Exciton and Charge Dynamics at Hybrid Organic-Inorganic Semiconductor Heterojunctions

by

Anurag Panda

A dissertation submitted in partial fulfillment
of the requirements for the degree of
Doctor of Philosophy
(Materials Science and Engineering)
in The University of Michigan
2018

Committee:

Professor Stephen R. Forrest, Chair
Assistant Professor Parag B. Deotare
Assistant Professor John T. Heron
Professor Jamie D. Phillips

apanda@umich.edu
ORCID iD: 0000-0001-7985-0013

To those who are knowledge-rich yet resource-poor

ACKNOWLEDGEMENTS

My foremost note of gratitude goes to the mentors who saw potential in me, took the time to patiently see me though my moments of naivete and stubbornness, and helped me discover new horizons of inquiry and ability. First and foremost, I am grateful to Prof. Stephen Forrest for continually challenging my thinking, focusing my undirected curiosity, and providing support when the project outcomes were not promising. In the past six years I have learned a tremendous amount about the culture of scientific research, how to see a vision through, and what it means to make lasting contributions to scientific progress while operating in "Pasteur's quadrant." I am also thankful to Prof. Alakananda Mukerji for blending art into my technical interests, Prof. Toby Cumberbatch for making me aware of the larger societal context in which technology exists, and David Berger for teaching me to work with my hands.

I am forever indebted to the citizens, whose taxes support the various scientific and educational institutions that made my education and research work possible. My particular thanks to Peter Cooper for endowing "education as free as air and water" in 1859. Without his visionary support I would not have been able to afford an undergraduate education the United States in 2007.

During the first three years of the PhD journey, Prof. Jeramy Zimmerman, Dr. Brian Lassiter, Dr. Michael Slootsky, Prof. Kyle Renshaw and Prof. Kyusang Lee provided initial training, clarified fundamental concepts, and filled me in on the generations-old equipment knowledge. Eva Ruff made all administrative processing smooth sailing, proofread this thesis, and offered much humor and support throughout. The Optoelectronic Components and Materials group members (also known as OCMers) and the

Lurie Nanofabrication Facility staff provided fun company and support during fabrication, measurement and brainstorming sessions. I am specially grateful to Xiao Liu, Dejiu Fan, Yue Qu and Kan Ding for support with the work presented in this thesis.

Outside the lab, the generosity I received from numerous people across Germany, Ghana, India, Burkina Faso and the U.S. during my travels kept me inspired and hopeful. In particular, my mind always wandered back to Ron Guttenberg's workshop in Glasgow, Montana, where in retirement he continues to repair discarded bicycles and gives them away to community members. Alexis Orkehov, Dr. Hassan Edress, Dr. Ravish Malhotra, Rohit Jain, Xiao Liu, Quinn Burlingame, Bikash Kanungo, and my brothers, Dr. Anshuman Panda and Arabind Panda, periodically helped me think through concerns beyond research. Kathryn Sutcliffe and I crossed paths midway though the journey and she has been a cheerful and encouraging companion since. The time we spent reflecting together how best to do good in our communities will always help keep me motivated and optimistic when confronted with failures.

Finally, I am eternally grateful to my parents, Anima Panda and Rabindra Nath Panda for gladly and repeatedly sacrificing their material and emotional well-being to provide me with world-class educational opportunities.

Anurag Panda

Ann Arbor, Michigan, U.S.A.

January 3rd, 2018

TABLE OF CONTENTS

LIST OF TABLES

Table

LIST OF FIGURES

Figure

LIST OF ABBREVIATIONS

Recurring Acronyms

CB	conduction band
CVD	chemical vapor deposition
DFT	density functional theory
DSSC	dye-sensitized solar cells
DOS	density of states
EL	electroluminescence
FRET	Förster resonance energy transfer
FWHM	full width at half maximum
HCTE	hybrid charge transfer exciton
$HCTE_F$	free HCTE
$HCTE_{QW}$	QW-confined HCTE
$HCTE_T$	trapped HCTE
HJ	heterojunction
HOMO	highest occupied molecular orbital
$J-V$	current density vs. voltage
LUMO	lowest unoccupied molecular orbital
MD	molecular dynamics
MBE	molecular beam epitaxy
OI	organic-inorganic
OI-HJ	organic-inorganic semiconductor HJ

OLED	organic light-emitting diode
OPV	organic photovoltaic
PL	photoluminescence
QW	quantum well
RT	room temperature = 294 K
SCL	space-charge-limited
SRH	Shockley-Read-Hall
TCL	trap-charge-limited
UHV	ultra-high vacuum
UPS	ultraviolet photoelectron spectroscopy
VTE	vacuum thermal evaporation
VB	valence band
WM	Wannier-Mott

Recurring Chemical Names

CBP	4,4'-bis(N-carbazolyl)-1,1'-biphenyl
DBP	tetraphenyldibenzoperiflanthene
ITO	indium tin oxide
P3HT	poly(3-hexylthiophene-2,5-diyl)
PEN	pentacene
PTCDA	3,4,9,10-perylene tetracarboxylic dianhydride

Recurring Fundamental Constants

N_A	Avogadro constant
k_B	Boltzmann constant
m_0	electron rest mass
q	elementary charge

h	Planck constant
$\hbar$	reduced Planck constant
c	speed of light
ϵ_0	vacuum permittivity

Recurring Parameters and Variables

ω	angular frequency
V_a	applied voltage
V_{bi}	built-in voltage
E_g	band gap or energy gap
E_B	binding energy
E_c	CB minimum energy
E_v	VB maximum energy
μ	charge carrier mobility
ΔE_{cL}	CB minimum and LUMO offset energy at the OI-HJ
ΔE_{vH}	VB maximum and HOMO offset energy at the OI-HJ
ΔE_{OI}	CB minimum and HOMO energy difference at the OI-HJ
ϵ_R	dielectric constant of a given material
$m_{e,R}$	effective mass of electron in a given material
$m_{h,R}$	effective mass of hole in a given material
m^*	reduced effective mass
EA	electron affinity (i.e. LUMO or E_c)
$E_{F,n}$	electron quasi-Fermi level
$E_{F,P}$	hole quasi-Fermi level
E_F	Fermi level
n_{HJ}	electron density in the inorganic semiconductor at the OI-HJ
P_{HJ}	hole density in the organic semiconductor at the OI-HJ

F	electric field
L_D	exciton diffusion length
EQE	external quantum efficiency
FF	fill factor
n_r	index of refraction
IP	ionization potential (i.e. HOMO energy or E_v)
V_{OC}	open-circuit voltage
ϵ	permittivity
PCE	power conversion efficiency
R_S	series resistance
J_{sc}	short-circuit current density
T	temperature
λ	wavelength

ABSTRACT

The advancements in our fundamental understanding of light-matter interaction in the past century are foundational to our technology-enabled modern lifestyle. While the physics and technology of inorganic semiconductors have been well-developed in the past 60 years, the development of organic semiconductors is in its nascent stages. Combination of the two material systems in organic-inorganic (OI) hybrid semiconductor systems have already found applications in next-generation solar cells, light-emitting diodes, and non-linear optical devices, yet the unique charge and exciton behavior at OI heterojunctions (HJs) remains largely unexplored. The stark differences in the optoelectronic properties of organic and inorganic semiconductors offer a rich and as of yet unexplored territory of charge and energy transfer processes in hybrid semiconductor systems. Expanding the physical understanding of these coupled material systems could potentially lead to major advances in semiconductor applications and science.

This thesis presents the first steps toward developing a comprehensive understanding of charge and exciton dynamics in coupled hybrid OI material systems. A theory of optical and electrical behavior of OI-HJ based diodes is outlined. The theory yields a quantitative model for current density versus voltage ($J-V$) characteristics of OI-HJ based diodes. The existence of a hybrid charge transfer exciton (HCTE) state, composed of a columbically-bound electron in the inorganic semiconductor and hole polaron in the organic semiconductor, is predicted at the hybrid heterointerface. The HCTE is found to be the the fundamental quasi-particle that governs the excited state properties of the diode. A first principles quantum mechanical model of the HCTE is developed to predict its optoelectronic properties. The external quantum efficiency, electrolumines-

cence, photoluminescence, and $J-V$ characteristics for multiple OI diode systems are presented along with model fits to the data. The fits yield insights into the dominant optoelectronic processes in OI material systems, including trap-mediated charge recombination and space-charge-limited current. The ability to systematically manipulate the optoelectronic properties of the HCTE by tuning the dimensionality of electron delocalization in the inorganic semiconductor is demonstrated. Potential novel applications and future directions for exploration that emerge for hybrid material systems as a result of the findings of this thesis are also discussed.

CHAPTER I

Introduction

This thesis is divided into five chapters. The first chapter discusses the motivation for studying semiconductor materials and specifically for undertaking a detailed study of the behavior of charges and excitons at organic-inorganic (OI) semiconductor heterojunctions (HJs). The fundamental physics concepts and materials growth techniques utilized for the results contained in this thesis are also introduced. The second chapter discusses the fundamental processes governing charges and excitons in OI-HJ based diodes and develops quantitative expressions for the device current density vs. voltage ($J-V$) characteristics. The third chapter develops a first principles theory for the hybrid charge transfer exciton (HCTE), along with simulations of the optoelectronic properties of the HCTE at engineered reduced dimensional OI-HJs. The fourth chapter presents experimental results for four different OI-HJ based diodes, along with their fit to the theory developed in parts two and three. The final chapter contains a summary of the results, along with suggested experiments to further refine our understanding of hybrid OI material systems and potential novel applications.

1.1 Motivation for researching semiconductor materials

The control and understanding of electric charge within matter and the interaction of matter with the electromagnetic spectrum are key advances that enabled the electronics revolution of the 20th century. Foundational to this revolution are semiconductor materials, which have charge transport properties in between insulators and conductors.

Their charge transport properties can be tuned by the application of an external voltage, doping, or formation of heterostructures with other semiconductors. Historically, inorganic materials such as Silicon, Germanium, and III-V compound materials (e.g. $In_{0.53}Ga_{0.47}As$, GaAs, InP and GaN) were employed as semiconductors because they can be highly purified (99.9999999%), controllably doped and precisely grown. These qualities have allowed the theory and technology of conventional inorganic semiconductors to mature over the last 80 years.

As a result, today billions of transistors operate in our computers and smartphones put unprecedented computational power at our fingertips, enabling seamless information access and increasing productivity. Optoelectronic devices are a subset of semiconductor devices used for electricity to light conversion or vice versa. These devices include lasers and photodetectors, which, coupled with optical fibers, have enabled instantaneous communication across the globe. Similarly, light-emitting diode (LED) and photovoltaic (PV) technology are poised to usher in a new generation of high-efficiency and environmentally benign lighting and power generation.

New developments in semiconductor technology promise higher energy efficiency, greater speed and lower cost for previously realized applications, and deployment in fields such as power electronics, medical imaging, mechanical and thermal energy harvesting and environmental monitoring and surveying. Additionally, the discovery of new phenomena in semiconductors promises completely new realizations of computing based on optical or quantum computing. As a result, recently, there is interest in a host of new semiconductor materials such as II-VI compound materials (e.g. ZnSe, CdTe, ZnO), two-dimensional materials (e.g. graphene, $MoSe_2$), complex and simple oxides (e.g. TiO_2, $YBa_2Cu_3O_{7-x}$), small molecules and polymers, biological molecules, colloidal quantum dots, and perovskites. Many of these can be deposited as thin films, processed at low temperatures, and have less stringent purity requirements for use in devices. As a result, these semiconductors have the potential to be less expensive than

their conventional inorganic counterparts and can be deployed into a variety of form factors. The work in this thesis focuses on inorganic III-V compound and simple oxide semiconductors, and organic small molecule semiconductors.

1.2 Comparison of organic and inorganic semiconductor properties

The disparate properties of organic and inorganic semiconductors are a result of their different internal bonding characteristics. Inorganics are generally grown as large crystals that are chemically bonded together either by covalent and ionic bonds. Organic molecules are deposited as thin films in a range of morphologies from crystalline to amorphous and are internally bonded with covalent bonds and held together as a film with van der Waals forces. As a result, their physical and optoelectronic properties are vastly different (summarized in Table 1.1). Most important for the purpose of this thesis are the optoelectronic properties. Inorganic semiconductors have a high charge mobility and dielectric constant, low oscillator strength, and their conductivity can be tuned several orders of magnitude by doping. Excitons in inorganics, known as Wannier-Mott (WM) excitons, have low binding energy with a large radius, while excitons in organics, known as Frenkel excitons, have high binding energy and a small radius. Organic semiconductors are the ideal platforms for some emerging optoelectronic applications because they can be fabricated on flexible substrates.

1.3 Motivation for researching organic-inorganic hybrid semiconductor material systems

Combining the desirable properties of organic and inorganic semiconductors in the same optoelectronic device often requires contacting them at OI-HJs. Many critical charge and energy transport phenomena in optoelectronic devices are determined by

Table 1.1: Comparison of the optoelectronic and physical properties of inorganic and organic semiconductors. Desirable and undesirable properties are highlighted in green and red, respectively. Exciton properties are highlighted in blue.

Property	**Inorganic**	**Organic**
Bond type	covalent/ionic	van der Waals
Charge transport	band transport	polaron hopping
Charge mobility ($cm^2/(Vs)$)	1000	10^{-3}
Dielectric constant	$5-15$	4
Refractive Index	$2-5$	$1-3$
Absorption (cm^{-1})	10^3-10^4	10^5-10^6
Oscillator strength	low	high
Exciton type	Wannier-Mott	Frenkel
Exciton binding energy (meV)	$5-10$	$200-1000$
Exciton radius (Å)	100	10
Hardness	hard	soft
Flexibility	brittle	flexible

the properties of HJs, such as energy level alignment between the two material systems and defect density at the HJ. Physics Nobel Prize winner Leo Esaki once said that while conventional semiconductors are "God-made crystals," heterostructures, with their unique properties not exhibited by natural materials, should be called "man-made crystals [1]." Contrasting Esaki's statement to a quote by another Physics Nobel prize winner, Wolfgang Pauli, makes the challenge in studying HJs clear: "God made the bulk; surfaces were invented by the devil [2]." Nevertheless, the study of heterogeneous semiconductor materials contacted at HJs are the subject of the 2000 Nobel Prize in physics and enabled specialized optoelectronic devices such as low-power solid state lasers and high-electron-mobility transistors. Heterojunctions between organic semiconductors are also critical for the operation of organic light-emitting diode (OLED) and organic photovoltaic (OPV) devices, where they are used for charge and exciton blocking, charge injection and exciton-to-charge conversion.

The use of both organic and inorganic semiconductors in the same device has already been widely demonstrated in optoelectronic devices. These devices explore both resonant and non-resonant energy and charge transfer between the two material systems.

For example, organic/metal oxide interfaces are used as charge generation layers in stacked OLEDs [3–5] and tandem OPVs [6]. Organic layers are used for surface passivation in conventional inorganic solar cells [7–9] and as charge transport layers in colloidal quantum dot solar cells [10], perovskite solar cells [11] and inorganic solar cells [12, 13]. Studies of exciton dissociation through charge transfer at the OI-HJ have been complicated by chemical reaction of organic molecules with unpassivated inorganic surfaces [14, 15] and exciton quenching by surface states. Nevertheless, charge separation at OI-HJs is widely utilized for operation of dye-sensitized solar cells (DSSCs) [16, 17].

In addition to the behavior of charges and excitons at OI-HJs, control of energy transfer between the bulk of the materials is of critical importance for optoelectronic applications. Efficient Förster resonance energy transfer (FRET) has been demonstrated from inorganic semiconductor to organic overlayers [18–20] and metal to organic overlayers [21, 22]. The FRET efficiency is systematically tunable by changing the barrier layer thickness between the two semiconductors [23–25]. Coupling the low exciton saturation density of inorganics with the high oscillator strength of organics using FRET has also resulted in the prediction and observation of non-linear optical phenomenon such as hybrid polaritons in optical cavities which have the potential to be used in low threshold lasers [26–29].

Beyond these already demonstrated device applications, type II OI-HJs can potentially support long lived HCTE states whose properties can be tuned by HJ engineering. Studies of OI-HJs between inorganic semiconductors such as CdS [30, 31], ZnO [32], ZnMgO [33], GaAs [34] and WS_2 [35] and organic semiconductors have already suggested existence of the bound state. This makes OI-HJs model systems for exploring the processes governing polaron-pair (i.e. charge transfer state) kinetics at organic semiconductor HJs, a process at the heart of OPV device operation [36, 37]. The HCTE also has the potential to be utilized in exciton based transistors, where the logic operations

are performed by controlling HCTE transport using either voltage or surface acoustic waves [38, 39]. This can result in increased energy efficiency since the HCTE can be converted directly into an optical signal for on-chip photonic interconnects, eliminating the resistive and relatively slower electrical interconnects. There is also interest in the use of hybrid interfaces for spintronic devices [40]. Finally, multilayer organic and inorganic thin film structures (i.e. OI superlattices) give an unprecedented ability to access new material properties and can have applications in quantum cascade lasers, terahertz sources, and thermoelectrics [41].

Although improvement in application of OI semiconductor systems in devices are demonstrated every year, there remains a tremendous gap in our understanding of how the properties of the two material systems and their HJs impact the behavior of charges, excitons and their interaction with electromagnetic radiation. No comprehensive study combining both theory and experiment has yet been presented that elucidates the role of the HCTE in determining the optical and electrical properties of OI-HJ diodes. Filling this gap in understanding through a systematic study has the potential to open up new physical understanding of OI material systems and enable their effective utilization in technological applications.

1.4 Overview of inorganic semiconductors

Currently, Si is the material of choice for the inorganic semiconductor industry. Although Si is relatively abundant and its properties sufficient for some integrated circuit and PV applications, its use in high frequency circuits and light-emitting applications is limited by its comparably low mobility and indirect band gap. III-V compound semiconductors were introduced to expand the range of functionality of semiconductor devices. Even though these materials are more expensive than Si, they are critical for commercially available high-frequency electronics, lasers, LEDs and photodetectors. Due to the performance requirements, industry goes to great lengths to ensure that the semicon-

ductors are formed into nearly perfect single crystals from highly pure source material.

1.4.1 Bonding in inorganic semiconductor crystals

Inorganic semiconductors consist of either covalently or ionically bonded nearly perfect single crystals [42]. During bonding, the core electrons of an atom are tightly confined to the nucleus and screen the same number of protons. The atom can then be thought of as a N^+ charge surrounded by a N^- electron cloud, known as the valence electrons. It is these valence electrons that interact to determine the type of bond the atoms will form, the crystal structure and the properties of the resulting solid. For example, in Si, an atom with four valence electrons, covalent bonds are formed by sharing one electron with each of the neighboring atoms, satisfying the octet rule. This is an example of covalent bonding because there is no charge transfer or Coulombic interaction within the atoms.

In ionic solids, the bond is formed through charge transfer between the atoms resulting in the formation of ions, which in turn are attracted by Coulomb forces and repulsed due to the Pauli exclusion principle. This type of bonding is found in atoms with different electronegativities, such as III-V and II-VI compound semiconductor materials that form partially covalent and partially ionic bonds. For example, in the GaAs crystal, electrons are transferred from As to Ga so that each of the atoms has four electrons, which results in ionic bonding between the As and Ga ions. The bonding results in the solid finding the minimum stable energy state and forming its equilibrium crystal structure. The bond formation for Si and GaAs is shown in Fig. 1.1.

1.4.2 Growth and processing techniques

Molecular beam epitaxy (MBE), metalorganic chemical vapor deposition (CVD) and radio frequency (RF) sputtering are the three growth techniques used in this thesis for depositing inorganic semiconductors. Molecular beam epitaxy has been the method of

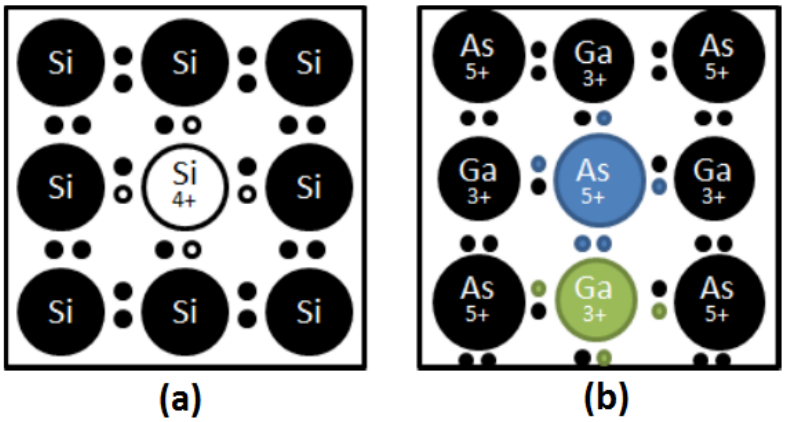

Figure 1.1: Bond formation in (a) Si and (b) GaAs crystals. The Si atoms forms purely covalent bonds by sharing one electron with each neighbor and retaining their four electrons. The Ga and As atoms form a mix of covalent and ionic bonds. The As transfers one of its five electrons to Ga, giving both four electrons. The resulting ions are attracted by Coulombic attraction and repulsed by the Pauli exclusion principle. Figure reproduced from Ref. [43].

choice, as it allows for epitaxial control over the device structure one monolayer at a time. Epitaxial growth is performed on a single crystal wafer grown by the Czochralski process. In this process, high purity material is melted in a crucible. Impurities are sometimes added to dope the melt. A seed crystal is then inserted into the melt and slowly pulled out from the melt while being rotated. Surface tension causes some of the molten semiconductor to adhere to the seed crystal as it is pulled from the melt. As this molten material solidifies, it extends the size of the seed crystal. Control of the temperature of the melt, the seed crystal rotation speed, draw rate, and cooling time governs the final boule diameter. The boule is then diced and polished to provide an atomically flat surface for device fabrication. The wafer is typically > 300 μm thick and serves as support for the < 10 μm thick device fabricated on top. For Si, polishing the wafer is the final growth step. The rest of the device processing is done by a combination of lithography, doping, oxidation, etching, and metallization. In the case of compound semiconductors, the device layers are further grown by MBE.

Epitaxial growth allows for fabrication of crystals composed of layers of different

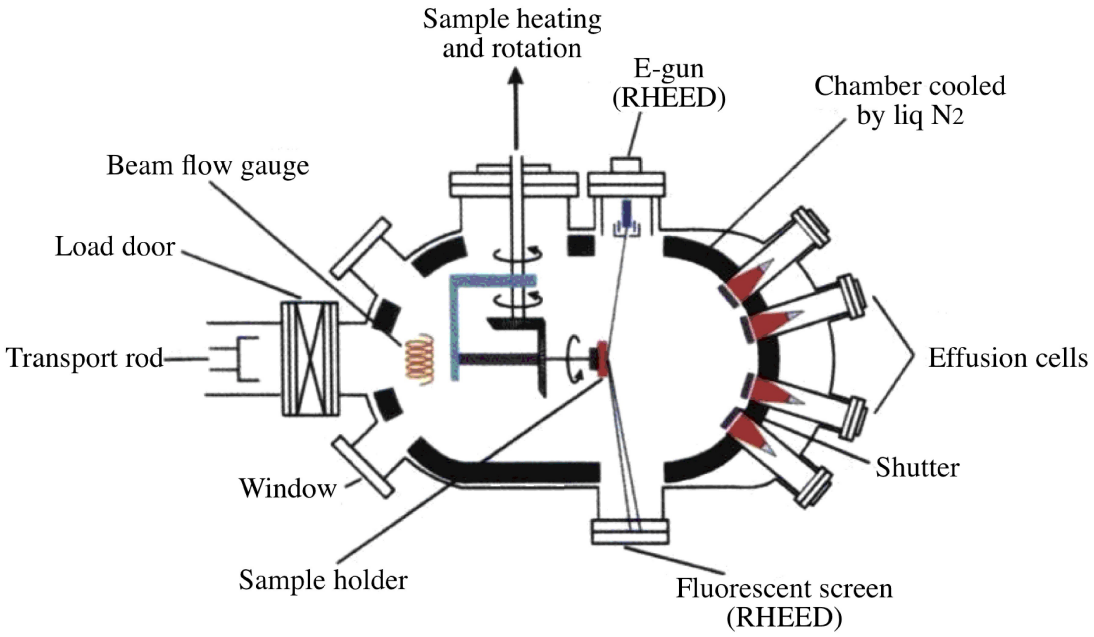

Figure 1.2: Layout of a solid-source MBE chamber used for epitaxial crystal growth for III-V and II-VI compound semiconductors on single crystal wafers. The wafer is grown by the Czochralski process. Materials are then introduced into the chamber by evaporating material in the effusion cells. Reflection high-energy electron diffraction (RHEED) is used to characterize the surface during growth. Figure adapted from Ref. [44].

semiconductor materials. A schematic of an MBE chamber is shown in Fig. 1.2. The MBE process is performed in a ultra-high vacuum (UHV) chamber (base pressure $< 10^{-9}$ Torr) with the chamber wall temperature kept at 77 K to avoid the incorporation of unwanted impurities in the crystal. The native oxide on the wafer surface is removed before loading into the chamber. After loading, the wafer is heated to $\sim 500^{\circ}$ C to degas and remove any residual oxide. Once a clean, oxide-free surface is recovered (confirmed using reflection high-energy electron diffraction (RHEED)), the substrate is heated to a temperature that allows the deposited materials to move around and find low energy equilibrium sites but not high enough to melt the substrate. Materials are then introduced into the chamber by evaporating material (solid-source MBE) or by flowing a gas such as phosphine (PH_3) through a heater at $\sim 1000^{\circ}$ C. As a result the hydrogen bonds break, freeing the phosphorous to deposit onto the substrate (gas-phase MBE). The composition and doping of the resulting monolayer is determined by the flux of each element onto the substrate, which is controlled by the source temperature or gas flow rate. For defect-free growth epitaxial layer thickness must be less than the critical thickness given as [45]:

$$t_c \approx \frac{a_o}{2|d|}, \tag{1.1}$$

where $d = \frac{a-a_o}{a_o}$, and a and a_o are the lattice constants of the substrate and epitaxial layer, respectively. When growing ternary or quaternary materials such as $In_xGa_{1-x}P$ and $In_xGa_{1-x}Al_{1-x-y}P$ the lattice constant and other crystal properties can be estimated by the compositional average of the binary compounds, also known as Vegard's law. The lattice constants for various compounds is given are Fig. 1.3. The extreme environmental control required for the MBE process makes it slow, low throughput, and prohibitively expensive for anything but the most specialized of devices. Further, this is a precision process that requires careful process control, calibration, and patience. Metalorganic CVD is a somewhat faster but comparable technique where the crystal can be grown over larger areas using precursor gases. The precursors react when in contact with

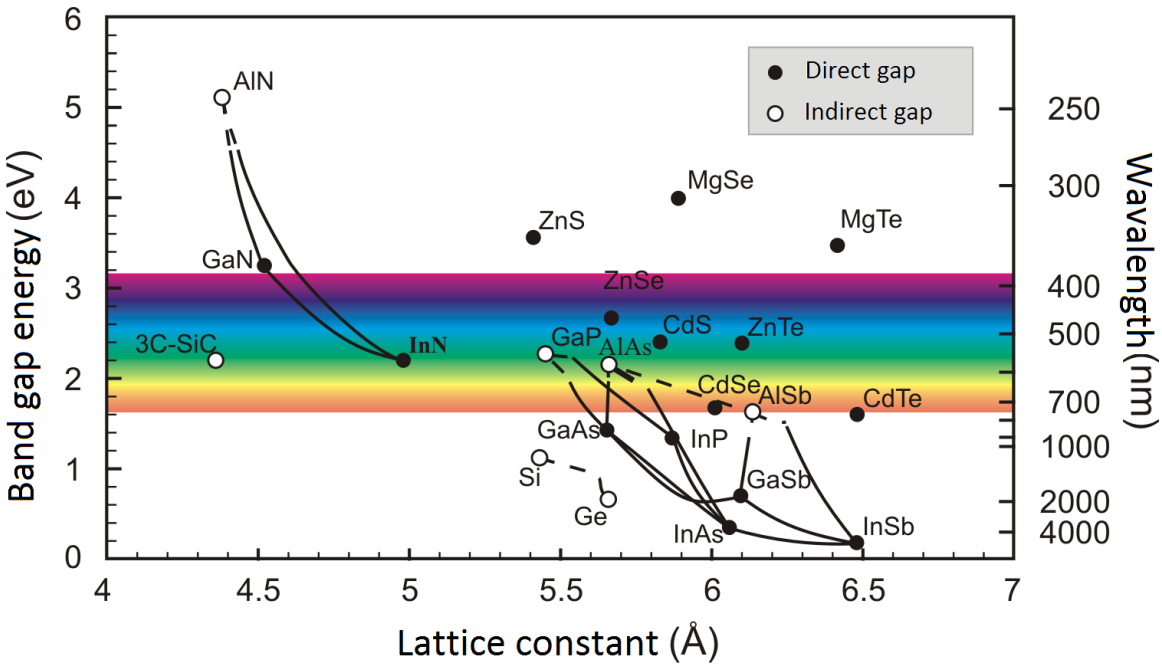

Figure 1.3: Band gap (E_g) and lattice constant (a_o) of crystalline inorganic semiconductors at RT. The right axis gives the wavelength corresponding to the E_g energy determined using the Plank relation. Semiconductors with E_g energy corresponding to the visible region of the electromagnetic spectrum are highlighted. The direct or indirect nature of the E_g is also indicated. Figure adapted from Refs. [46] and [47].

the hot substrate surface, depositing the heavy metal atom while the volatile organic component either remains attached for subsequent reaction or is pumped out.

For sputtering, a non-reactive gas such as Ar is ionized and bombarded onto a target to carry out physical deposition of materials from a target onto the substrate. Since the sputtered atoms undergo collision with the ionized gas on the way to the substrate, the atoms reach the substrate after going through a random walk, making conformal coverage of the substrate possible. A schematic of an RF magnetron sputtering chamber is shown in Fig. 1.4. Sputtering performance can be improved by adding a strong magnetic magnetic field that confines the ionized gas in the plasma close to the surface of the sputtered target that increases the ionized gas bombardment rate. An RF signal can be applied to the target to ensure there is no surface charge buildup, which is necessary for insulating materials. Reactive sputtering, done by adding reactive gas

such as O_2 or N_2 to the chamber, offers control over the stoichiometry of the sputtered film. However, this method offers limited control over the crystallinity of the deposited film, which is tunable with the substrate temperature and deposition rate.

Due to the strong chemical bonds that hold inorganic semiconductors together, it is possible to do extensive processing on them without risking damage to the bulk of the material, such as photolithography, high temperature annealing, and wet and reactive ion etching (RIE). For lithography a light sensitive chemical is spin coated onto the wafer and exposed through a mask with the desired pattern. The chemical in either the exposed or unexposed area can then be selectively removed using a developer, allowing for further processing of the exposed area. High temperature annealing is done to increase the quality of Ohmic contact to the semiconductor, which is generally deposited on the back side of the wafer. Etching is done to either expose buried layers, remove the native oxide, or to lift off a layer. For wet chemical etching, an acid such as buffered HF that can chemically react to dissolve away oxides is used. In RIE, the substrate is etched by ionized reactive gases in plasma which reacts with atoms on the surface of the substrate to form volatile species which are continuously evacuated from the chamber. As compared to wet etching that results in the undercut of patterned photoresist, plasma etching can be more anisotropic.

1.4.3 Electronic states of crystalline inorganic semiconductors

According to the theory of quantum mechanics, the state of a system is described by Ψ, its wave function. In the Born-Oppenheimer approximation, the nuclear coordinates are assumed to be static as compared to the electron coordinates, allowing for separation of the wave function of the two, $\Psi = \psi_n \psi_e$. In the static nuclear coordinate configuration, ψ_e can be determined by solving for the eigenstates of the time-independent Schrödinger equation:

$$\hat{H}\psi_e = \left(-\frac{\hbar^2}{2m_0}\nabla^2 + U(r)\right)\psi_e = E\psi_e, \tag{1.2}$$

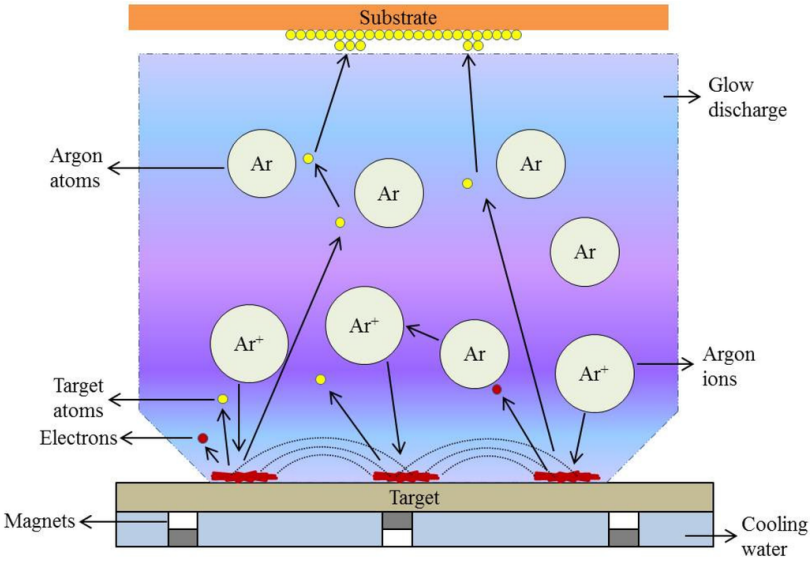

Figure 1.4: Layout of a radio frequency sputtering chamber. Ar gas is ionized and bombarded onto a target resulting in physical deposition of materials from the target onto the substrate. In magnetron sputtering, a magnetic field is applied to confine the ionized gas in a plasma close to the surface of the target increasing the ion bombardment rate. Figure reproduced from Ref. [48].

where $\hat{H}$, the Hamiltonian, is the operator corresponding to the total energy of the system, m_0 is the electron rest mass. The $\hbar = h/2\pi$ where $\hbar$ is the reduced Plank constant and h is the Plank constant. The first term is the kinetic energy of the electron and the second term, $U(r)$, is the potential energy experienced by the electron within the solid. In the simplest case, the potential energy results predominantly from nucleus-electron interactions. A crystal consists of periodically spaced nuclei which are partially screened by core electrons. The valence electrons are delocalized throughout the crystal and interact with the potential energy resulting from unscreened protons. This yields a periodic wave function of the electron and is summarized by the Bloch theorem:

$$\psi_k(r) = \psi_k(r+R) = e^{ik\cdot r}U(r), \tag{1.3}$$

where k is the wave vector of the electron in the first Brillouin zone in reciprocal space (k-space) and $U(r)$ is a periodic function with the same periodicity as the crystal. Since

Eq. 1.3 holds for any translation by the lattice periodicity, R, this indicates that an electron in this state is shared equally with all the lattice sites in the crystal. The delocalized nature of the electronic states is the reason for the high electronic coupling and charge mobility in crystalline semiconductors.

The result of the periodic potential on the optoelectronic properties of the crystal is seen by solving Eq. 1.2, which yields the energy-momentum ($E-k$) relationship of electrons in the crystal, also known as the dispersion relation. Various techniques are used for solving the equation, including the tight-binding method [49], $k \cdot p$ method [50] and density functional theory (DFT) [51]. While qualitative agreement can be obtained by simplifying approximations, calculations accounting for electron-electron interactions and spin-orbit coupling are necessary to quantitatively match experimental results.

As a result of the delocalization of the electrons through the crystal lattice, their discrete energy levels in an isolated atom become a range of energy levels, each corresponding to multiple wave vectors supported by the crystal. These energy levels are known as bands. An important result is the disallowed energy levels that form a gap, known as the band gap (E_g) of the crystal. Energies within the E_g not allowed for charge carriers. The E_g directly relates to the minimum photon energy the crystal can absorb, or the photon emission wavelength of the crystal by the Plank-Einstein relation:

$$E = h\nu = h\frac{c}{\lambda} = \hbar\omega, \tag{1.4}$$

where c is the speed of light, and ν, ω and λ are the frequency, angular frequency and wavelength of the photon, respectively. Further, $\nu = \omega/(2\pi)$. The energy levels below the gap are called the valence band (VB) energies and the levels above are called the conduction band (CB) energies. The CB minimum energy (E_c) and VB maximum energy (E_v) are primarily responsible for optoelectronic processes in the crystal since

any photoexcited, thermally excited or injected charge carriers thermalize into these two levels. In the CB, the current flow occurs by the movement of electrons while in the VB, the flow is conducted by the absence of electrons known as holes.

Near the CB minimum, the dispersion relation can be approximated by a parabolic function, $E = \frac{\hbar^2 k^2}{2m_{e,R}}$, where $m_{e,R} = \hbar^2 \frac{\delta k^2}{\delta^2 E}$ is the effective mass of the electron in the crystal, usually stated as a multiplier of m_0. With this approximation, the electron can be treated as a free carrier in the solid characterized by its effective mass, and the classical Newtonian equations can be used to describe the movement of the charge carrier. A similar treatment is applicable for the hole, whose $m_{h,R}$ is generally higher.

The calculated $E-k$ relationship for (a) Si and (b) GaAs for different momentum of electrons (wave vectors) supported by the crystal are shown in Fig. 1.5. The E_g of Si is 1.1 eV at room temperature = 294 K (RT) and the minimum of the CB is located offset from the Γ-point. As a result, it is known as an indirect gap material and is inefficient at photon emission by carrier recombination. For GaAs, the E_g is 1.4 eV at RT and is located right at the Γ-point, making it a direct gap material. If the crystal is not symmetric along different axes, $m_{e,R}$ is given as a tensor quantity. The E_g for multiple inorganic semiconductors along with their lattice constants and the nature of their gap are shown in Fig. 1.3. The interatomic spacing in a crystal decreases with decreasing temperature, resulting in a increase in the E_g. The temperature dependence of E_g is given by the Varshini coefficients of the semiconductor [52].

1.4.4 Carrier generation

Carrier occupation in a solid at a given temperature (T) is mathematically described by its Fermi level (E_F) and density of states (DOS). The E_F represents the equilibrium occupation level for the electrons and holes in the material and generally lies between the E_c and E_v, within the E_g. At 0 K the E_F is also known as the Fermi energy, and the system is in its lowest energy configuration. As a result all available electronic

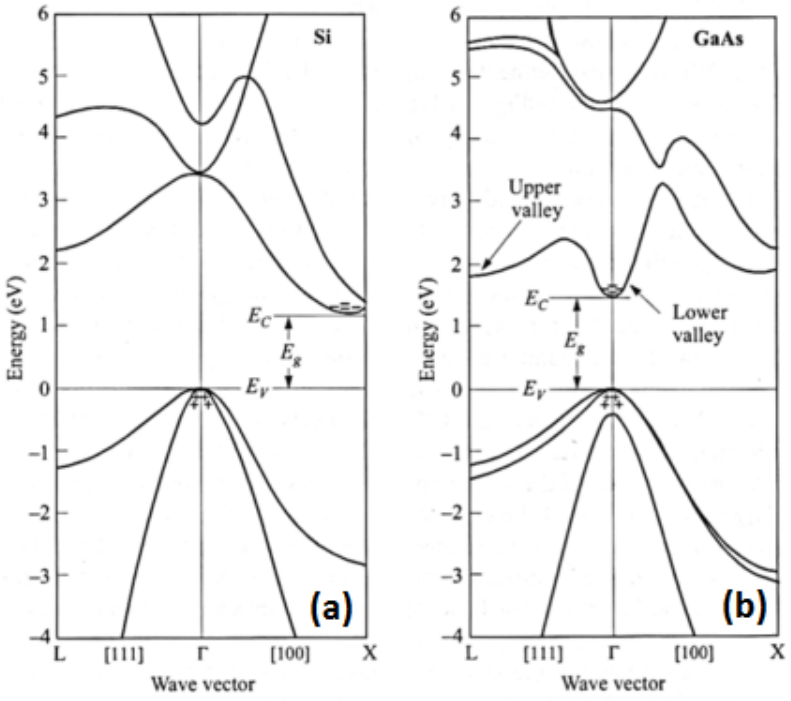

Figure 1.5: Energy-momentum ($E-k$) relationship of electrons in (a) Si and (b) GaAs at RT. Silicon is an indirect E_g material because the E_c and E_v do not occur at the same wave vector. GaAs is a direct E_g material since the E_c and E_v occur at the same k-vector, conserving momentum and allowing for efficient photon emission or absorption. Figure reproduced from Ref. [53].

states above the E_F are empty while the ones below are full. As the temperature rises, increasing the thermal energy available to the lattice, electrons are excited above the Fermi energy and holes are generated below only if there is an availability of states. As a result, the E_g changes with temperature. If states are available right at E_F, the material can conduct charges and behaves as a metal. If the E_F lies deep within the E_g and both the E_c or E_v are several k_BT away from E_F, the material behaves as an insulator due to a low density of excited charge carriers in either of the bands. The intermediate case results in semiconductors. Fermi-Dirac statistics used to describe carrier occupation probability as a function of energy, given as:

$$f(E) = \frac{1}{1 + exp\left(\frac{E-E_F}{k_BT}\right)} \approx exp\left[\frac{-(E-E_F)}{k_BT}\right], \tag{1.5}$$

where k_B is the Boltzmann constant. The approximation in Eq. 1.5 is the Boltzmann approximation and is valid when E is greater than a few k_BT above E_F. This is not the case at low temperatures or for degenerate (heavily doped) semiconductors. The carrier density per unit energy is given as $n(E) = D(E)f(E)$, where $D(E)$ is the DOS per unit energy. For example, for a 3D crystal, $D(E) = \sqrt{2}m_{e,R}^{3/2}\sqrt{E-E_c}/(\pi^2\hbar^3)$. The $D(E)$ changes based on the dimensionality of the system as shown in Fig. 1.6. Integrating over energies gives $n = N_c exp\,[-(E_c - E_F)/(k_BT)]$, where $N_c = (m_{e,R}k_BT)^{3/2}/(\sqrt{2\pi^3}\hbar^3)$ is the effective density of states at the CB.

For an intrinsic (undoped) semiconductor, the E_F is roughly in the middle of the gap (depending on the DOS, $m_{e,R}$ and $m_{h,R}$). The Fermi energy can be tuned by intentionally incorporating dopants into the crystal lattice during crystal growth or afterward by diffusion. For example, in Si, a Group IV element, Group V element P can be added to the crystal to increase the free electron concentration and move the Fermi level closer to the CB. The Group III element B can be added to create a hole and move the E_F close to the VB. This process is shown in Fig. 1.7. For effective doping, the localized energy

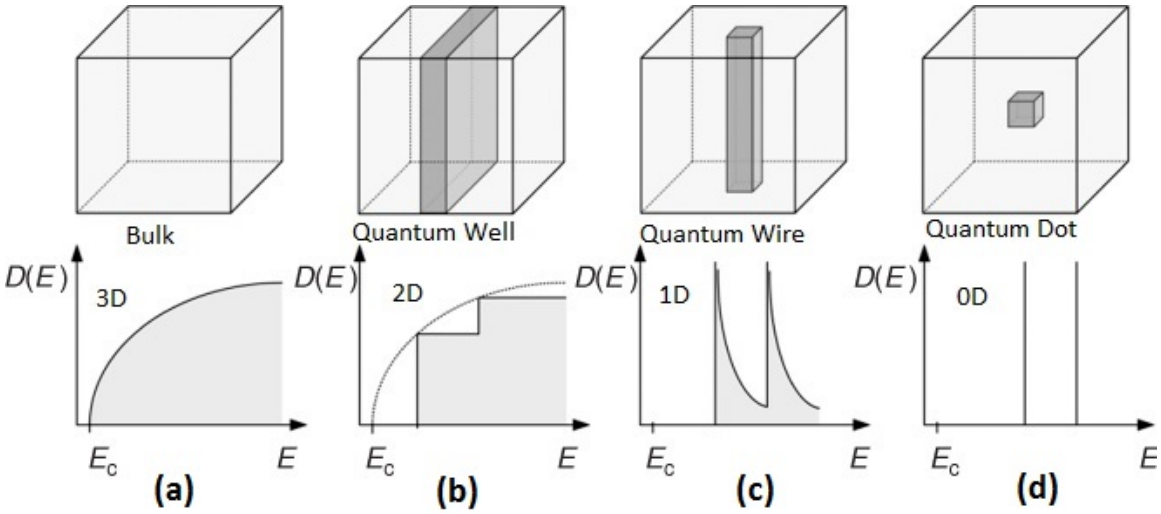

Figure 1.6: Dimensionality of a semiconductor and its corresponding DOS per unit energy ($D(E)$) for electrons above the E_c. A similar trend is applicable for holes below the E_v. Reduction in dimensionality results in a corresponding change in the the shape and reduction in the magnitude of the DOS. Figure adapted from Ref. [54].

levels of the dopants relative to E_c or E_v (ionization energy of the dopant, E_D) should be smaller than the k_BT so the charge carrier can be thermally excited and contribute to conduction. The E_F for a doped semiconductor depends on the temperature. When the thermal energy is comparable or higher than $E_g/2$, the E_F moves toward the middle of the E_g. When the lattice thermal energy is below E_D, this is known as the carrier freeze-out region, and the E_F moves to E_D below the respective band for the dopant.

1.4.5 Carrier transport and recombination

The static and dynamic behavior of charge carriers in semiconductors are described using three key sets of equations: the electrostatic equation, the transport equation, and the continuity equation. All the equations are written in 1D, which is sufficient for modeling most optoelectronic devices. However, they can be easily expanded into 3D as necessary. The Poisson equation describes the electrostatics by relating the charge

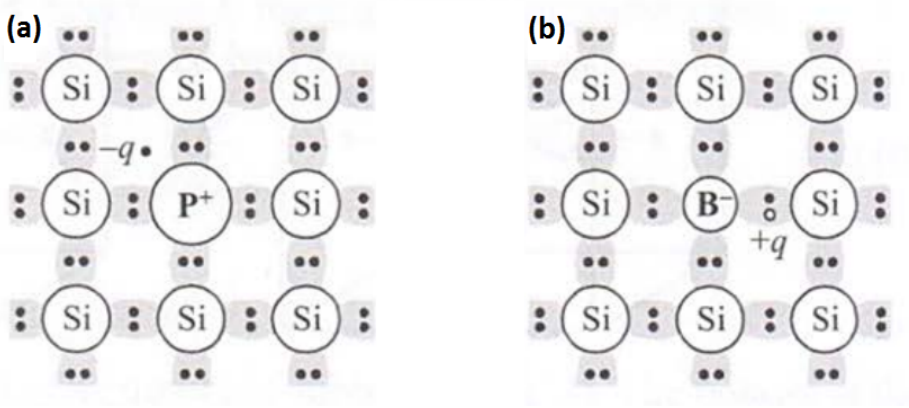

Figure 1.7: Doping of Si lattice by (a) incorporating Group V P generates a free electron and (b) incorporating Group III B generates a free hole. Figure reproduced from Ref. [45].

density to the electric field in the device:

$$\frac{d^2V}{dx^2} = -\frac{dF}{dx} = -\frac{\rho}{\epsilon}, \tag{1.6}$$

where V is the potential, F is the electric field, ρ is the charge density, $\epsilon = \epsilon_R \epsilon_0$ is the permittivity, ϵ_R is the dielectric constant of a given material or its relative permittivity and ϵ_0 is the vacuum permittivity.

For current conduction, drift and diffusion are the two key processes:

$$J = q\mu nF + qD\frac{dn}{dx} = q\mu\left(nF + \frac{k_B T}{q}\frac{dn}{dx}\right) = \mu q\frac{dE_F}{dx}, \tag{1.7}$$

where q is the elementary charge, μ is the charge carrier mobility and D is carrier diffusivity. In Eq. 1.7 the first term is the drift term and the second is the diffusion term. Near equilibrium, the second equality is written by using the Einstein relation ($D = \frac{k_B T}{q}\mu$). The third is written by using the Boltzmann approximation. The velocity of a charge carrier in the crystal due to the application of an external electric field is given by $v = \mu F$. The mobility is a function of $m_{e,R}$ or $m_{h,R}$, and the carrier lifetime, τ (i.e. $\mu = q\tau/m_{e,R}$). The lifetime of a carrier is determined by various scattering

processes such as phonon scattering, defect scattering, ionized impurity scattering, and recombination processes [45].

While the drift-diffusion equations are valid in regions where carriers do not recombine, the continuity equation deals with carrier recombination and generation. The continuity rate equation is a balance of current flow, generation (optical or electrical), and recombination:

$$\frac{dn}{dt} = G - R + \frac{1}{q}\frac{dJ}{dx}, \tag{1.8}$$

where G is the generation rate and R is the recombination rate. Under low excitation or injection the change is carrier density is well described by the first-order product of rate constants and carrier densities [55]. With these three sets of equations, an extensive set of semiconductor device phenomenon can be described.

1.5 Overview of organic semiconductors

Organic compounds primarily contain carbon atoms. The subset of these materials known as organic semiconductors have a highly conjugated π-electron system and are of interest for optoelectronic applications. Organic semiconductor compounds can broadly be separated into two categories: small molecules and polymers. The term small molecules is used for molecules with well defined molecular structure and weight, while polymers are chains consisting of varying lengths of monomers. Chemical structures of archetypical organic semiconductors polymer poly(3-hexylthiophene-2,5-diyl) (P3HT) and small molecule 3,4,9,10-perylene tetracarboxylic dianhydride (PTCDA) are shown in Fig. 1.8. As compared to inorganic semiconductors, organic semiconductors have advantages in applications that require flexible substrates such as medical applications, and large-area coverage such as PV [56, 57].

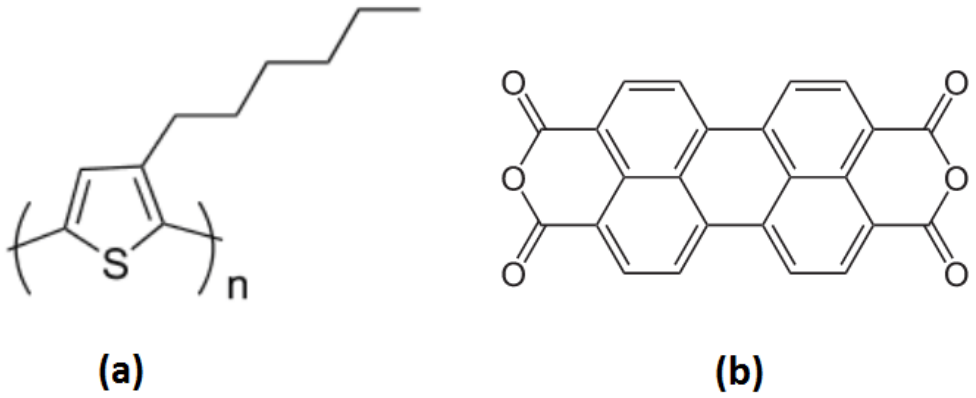

Figure 1.8: Archetypical organic semiconductor (a) polymer P3HT (b) small molecule PTCDA. Both the compounds have served as testbed for fundamental opto-electronic properties of organic semiconductors.

1.5.1 Bonding in organic semiconductor thin films

Isolated molecules or polymers are self-contained and chemically stable since their valence shells are filled. As a result, they do not interact strongly with neighboring molecules. Instead, the films are held together by van der Waals forces originating from dipolar interactions. The dipoles can arise from momentary fluctuations in the electron density of one molecule which induces a dipole of the opposite polarity in its neighboring molecule. The dipole-dipole interaction, known as the London dispersion force, falls off as r^{-6}, where r is the distance between the dipoles. This attractive force is countered by a repulsive force that arises from core repulsion, and is approximated with a r^{-12} dependence. The sum of the two forces results in the Lennard-Jones potential:

$$V_{LJ} = 4\alpha\left[\left(\frac{\sigma}{r}\right)^{12} - \left(\frac{\sigma}{r}\right)^{6}\right], \tag{1.9}$$

where α is the depth of the binding potential well and σ is the intermolecule distance at which the potential goes to zero. This weak intermolecular coupling and lack of electron sharing between molecules results in highly localized charges and excitons in organic semiconductor films. Within organic molecules, there are strong covalent bonds that

result in formation of molecular orbitals and give rise to its optoelectronic properties.

1.5.2 Purification and growth techniques

Chemical impurities can significantly degrade the electrical and optical properties of organics. Uncatalyzed reactants and solvents left from material synthesis, oxidized materials from unintentional oxygen exposure, and photoxidation are some of the sources of these impurities. Impurities act as both electrical and excitonic traps and reduce device performance. Material purification is thus a critical step when working with organic semiconductors.

Gradient sublimation, illustrated in Fig. 1.9, is the method widely used to purify small molecules. For polymers, high-performance liquid chromatography (HPLC) or the zone refining method is used. In gradient sublimation, a quartz cylindrical tube containing the material at one end is heated with a thermal gradient across its length as it is continuously evacuated to $\sim 10^{-6}$ Torr. As the temperature on the end with the material is slowly raised, the compound sublimes and diffuses to the lower temperature end. The temperature gradient is calibrated to ensure that the middle of the tube is slightly below the sublimation temperature of the material. Thus, sublimed high quality material condenses in the middle of the tube. Impurities with other condensation temperatures settle at other spots along the tube. Each cycle takes $1-3$ days and $1-3$ cycles are typically necessary to reach acceptable purity levels from the material obtained from the manufacturer.

One potential advantage of organic semiconductors is the promise of low temperature and low cost fabrication. There are a great variety of organic deposition and patterning methods in use, which range from solution processing to vacuum deposition. Generally, conjugated polymers are deposited by spin casting from dilute solution in solvent while small molecules are deposited by vacuum thermal evaporation (VTE). However, many other techniques [60] such as organic vapor phase deposition (OVPD)

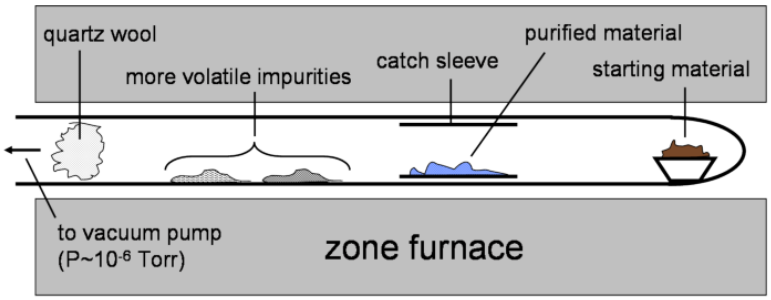

Figure 1.9: Schematic of a typical gradient sublimation setup. The material is loaded into one end of a quartz tube held at $\sim 10^{-6}$ Torr vacuum. The tube is then heated with a thermal gradient across it. The material and impurities sublime and settle in different sections of the tube. Figure adapted from Refs. [58] and [59].

[61] and inkjet printing [62] continue to be developed.

In this work, VTE is used for depositing organic thin films. Fig. 1.10 shows the schematic of a typical VTE chamber. For VTE, the chamber is kept at high vacuum ($< 10^{-7}$ Torr) and the material is resistively heated in a baffled boat made of Mo. As a result, ballistic vapor streams of the material are generated and deposited on the substrate. The deposition rate is exponentially dependent on source temperature and is typically within $1-5$ Å/s. The deposition rate is monitored using a quartz-crystal monitor whose resonance frequency changes based on the amount of material deposited on it. The substrate is also rotated to achieve film thickness uniformity. Patterning of films is done by shadow masking, where a patterned metal film is placed in contact with the substrate before deposition. Since most systems have more than one source, codeposition of two or more organics is also possible by careful control of temperature of the two sources monitored by independent quartz-crystal thickness monitors.

1.5.3 Electronic states in organic semiconductors

Carbon (atomic number 6) has a ground state of $1s^2 2s^2 2p^2$. There are four valence electrons in the outer shell that participate in bonding. The bonding scheme of interest for conjuguated molecules that show high electron conductivity is when they form three

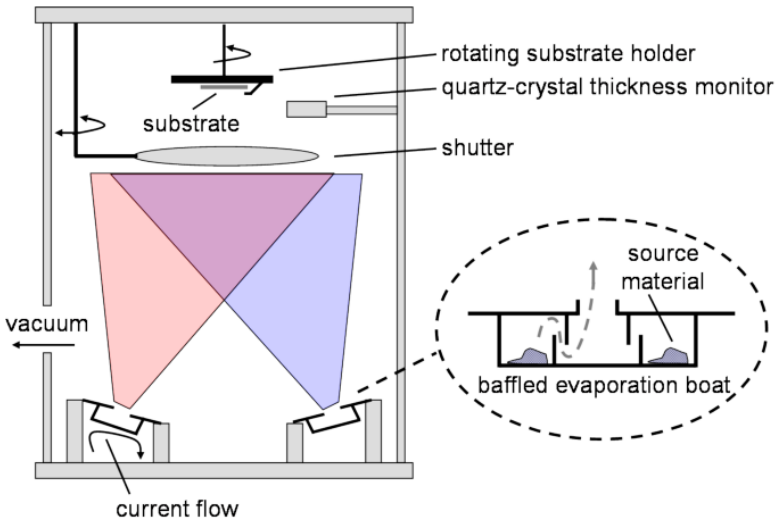

Figure 1.10: Schematic of a typical VTE chamber. A Mo baffle boat containing organic semiconductor small molecules is resistively heated to the sublimation point creating a vapor flux that deposits on a substrate facing down on top of the chamber. Codeposition of two or more organic molecules is also possible by careful control of the temperature of two sources monitored by two independent quartz-crystal thickness monitors. Figure reproduced from Ref. [59]

degenerate in-plane hybrid sp^2 orbitals, known as σ bonds. The fourth electron is the out-of-plane p-orbital (p_z) that interacts to form π bonds that create a delocalized "sea of electrons" above and below the plane of the molecule. The two bonding schemes are shown for ethylene (C_2H_4) in Fig. 1.11.

Similar to inorganic semiconductors, the electronic states of organic semiconductors are determined by solving the Schrödinger equation for the molecular orbital wave functions. Again the Born-Oppenheimer approximation is almost always made. Further, by ignoring spin-orbit coupling, separation of the spatial and spin component of the wave function is possible. Methods such as linear combination of atomic orbitals (LCAO) [64], Hartree-Fock [65] and DFT are used to solve for the properties of the molecule. In DFT, the n-body problem is recast as a solution to a one-body non-linear Schrödinger equation to the effective potential (Kohn-Sham potential), which is a function of the charge density and includes exchange-correlation [51]. A functional can then be used

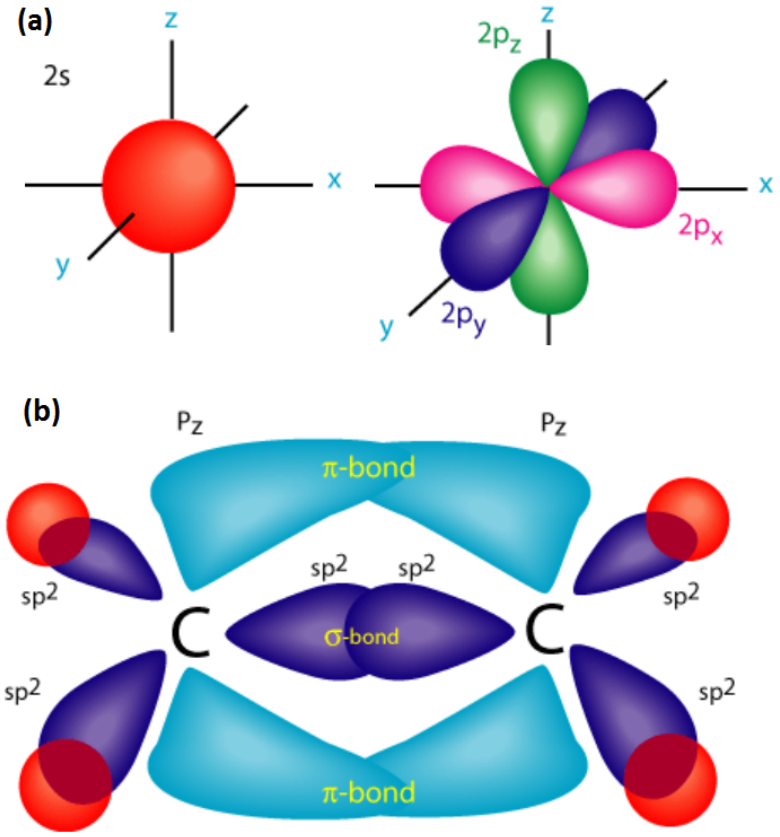

Figure 1.11: (a) The 2s and 2p valence orbitals of carbon that participate in bonding. (b) Bonding in ethylene (C_2H_4) showing the σ bonds formed by hybridized s, p_x and p_y orbitals (sp^2) and π bonds formed by out-of-plane p_z orbitals. Figure adapted from Ref. [63].

to relate the charge density to the ground state properties of the molecule. For DFT calculations done in this work, the basis set 3-21G with exchange-correlation energy functional B3LYP is used. This indicates that three primitive Gaussians are used to construct each core atomic orbital basis set and the valence orbitals are composed of two basis functions each, the first a linear combination of two primitive Gaussian functions, and the second a primitive Gaussian function. B3LYP stands for Becke, 3-parameter, Lee-Yang-Parr.

The number of molecular orbitals increases with the number of atoms and the filling of the molecular orbitals is governed by a combination of the Aufbau principle, Pauli exclusion principle and Hund's rule. The Aufbau principle states that electrons are filled from the lowest to the highest energy orbitals. The Pauli exclusion principle states that two fermions with the same spin cannot occupy the same orbitals. Hund's rule states that when electrons occupy the same energy level, one electron will enter each orbital with the same spin, followed by the doubling up of electrons with the opposite spin. The close proximity of interacting atomic levels causes the energy levels to split and create bonding (higher energy) and anti-bonding (lower energy) orbitals. For the bonding orbitals, the π bonds are typically higher energy than the σ bonds, while for the anti-bonding orbitals π^* is lower energy than the σ^*. As a result, the highest occupied molecular orbital (HOMO) and lowest unoccupied molecular orbital (LUMO) of organic semiconductors, which are analogous to the CB and VB in inorganic semiconductors, have π and π^* characteristics, respectively. Further, the spacing between the bonding and anti-bonding orbitals decreases as the conjugation length of the atoms increases. This is demonstrated by the energy gap of napathene (composed of 2 fused benzene rings) as compared to pentacene (composed of 5 fused benzene rings), which decreases from 5 eV to 2.2 eV [66], as shown in Fig. 1.12.

The HOMO or ionization potential (IP) of organic molecules is determined experimentally using either cyclic voltammetry or ultraviolet photoelectron spectroscopy

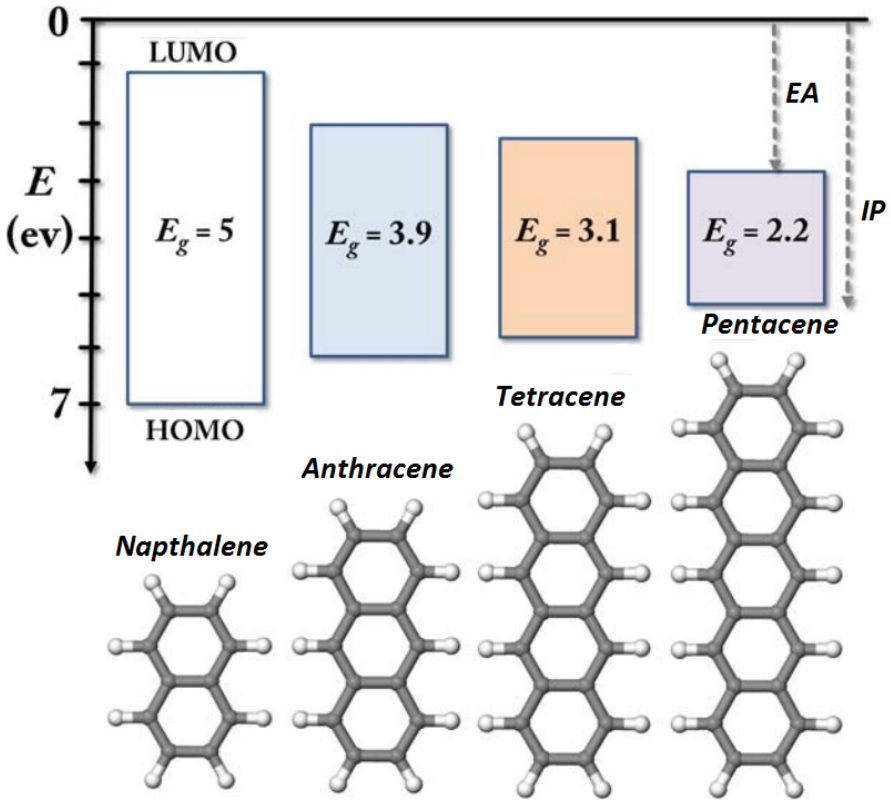

Figure 1.12: E_g, EA or LUMO and IP or HOMO of small molecule organic semiconductors as a function of their conjugation length. As the conjugation length increases the E_g decreases. Figure adapted from Ref. [67].

(UPS). The LUMO or electron affinity (EA) can also be determined using cyclic voltammetery or inverse photoemission spectroscopy (IPES). However, the measurement accuracy of EA ($\approx$ 0.5 eV) is worse as compared to the IP ($\approx$ 0.1 eV) due to the reorganization energy of the molecule upon addition of an electron. Instead, the optical energy gap (E_g) determined by absorption measurements can be added to the HOMO to calculate the approximate LUMO. These energy levels are referenced to the vacuum level of the material. The UPS measurement is done by illuminating the sample with He I emission from a gas-discharge lamp (21.22 eV) and collecting the emitted electrons using a hemispherical deflector that acts as a energy filter. The spectra as functions of energy are plotted with respect to the instrument Fermi level (determined using a calibration Au sample). The onset of emission then determines the HOMO and the secondary cutoff determines the vacuum level. The experimental setup for UPS measurement and a representative spectra are shown in Fig. 1.13.

1.5.4 Carrier generation and transport

The nearly free carrier transport via band description is rarely appropriate for organic semiconductor films. Instead in organic films, because the intramolecular electron-phonon coupling exceeds the intermolecular electronic coupling, the excited molecule quickly relaxes to the lowest available energy vibrational configuration and polarizes neighboring molecules. The combination of a charge carrier and the ensuing polarization of neighboring molecules is known as a polaron. While discrete electronic states are characteristic of isolated molecules, in a thin film the interaction between the random dipole fluctuations and the various molecular configurations widen the HOMO and LUMO energy distributions and give rise to broadened absorption spectra and transport levels.

The thermally generated charge carrier concentration in organics is low due to their large E_g. Impurities, chemical defects and atmospheric contamination lead to some

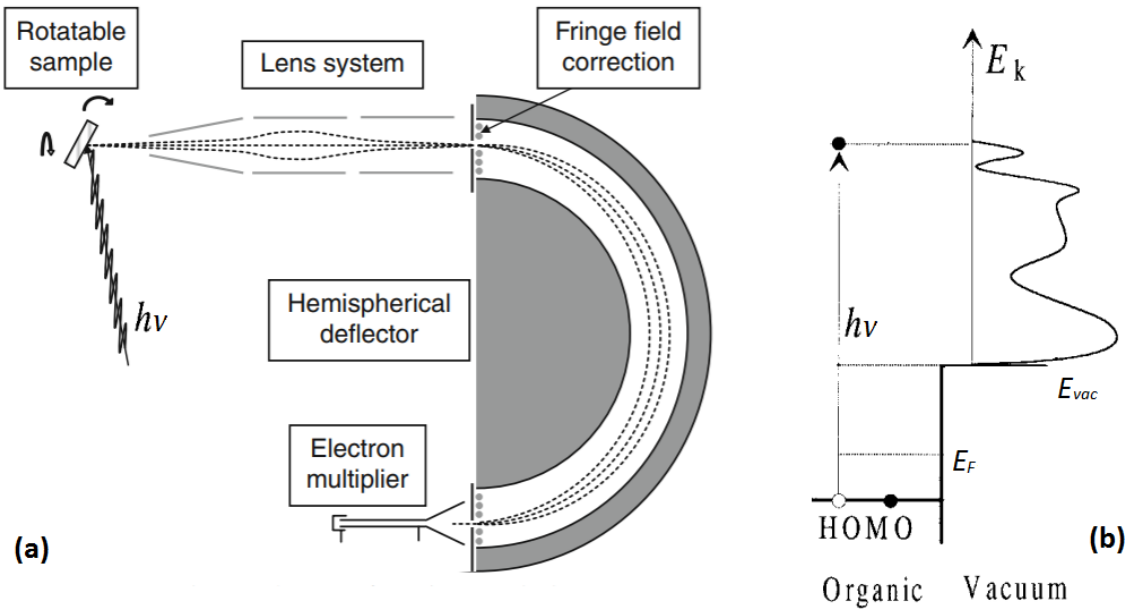

Figure 1.13: (a) UPS setup used to measure the IP of semiconductors. (b) Typical spectra obtained from UPS measurement (counts vs. electron kinetic energy (E_k)) which is referenced to the Fermi level of the instrument (E_F). The sample is illuminated with He-I emission from a gas-discharge lamp ($h\nu = 21.22$ eV). The kinetic energy of a collected electron is then $E_k - E_{vac}$, where E_{vac} is vacuum level energy of the film. Figure adapted from Refs. [46] and [68].

unintentional doping, however charge carriers are mostly introduced by the contact or though optical excitation. Electrical doping has been demonstrated, albeit with limited success [69, 70]. Doping is usually achieved by incorporating molecules with a lower LUMO or higher HOMO than those of the molecules in the film. This leads to the generation of charge carriers due to charge transfer between two adjacent molecules. Increasing carrier density using this method is limited due to the factor of 50 size difference between an organic molecule compared to an inorganic dopant atom. This restricts the range of doping achievable without perturbing the electronic states of the host molecules.

Carrier injection into an organic film is done by metal or metal-oxide contacts that range somewhere between Ohmic and Schottky-type depending on the alignment of the Fermi level with that of the organic. Ohmic contacts are characterized by an infinite reservoir of charge which is provided as needed by the bulk, while Schottky contacts are characterized by a depletion of charge near the contact, resulting in a barrier. In practice, no contact is truly Ohmic, since a potential barrier exists for injection into an organic layer. Although various thermionic emission models have been shown to be applicable for treating injection over a barrier, these should be applied with caution due to trap states at the interface that lower the barrier to injection.

Polarons travel through organic semiconductor film by a field-assisted stochastic hopping process. To describe molecule to molecule transfer, the Miller-Abraham transfer rate given as is used [71]:

$$k_{et} = \upsilon \, exp(-2\gamma R) \left\{ \begin{array}{ll} exp\left(-\frac{\Delta E}{k_B T}\right) & \text{, if } \Delta E > 0 \\ 1 & \text{, if } \Delta E < 0 \end{array} \right\}, \tag{1.10}$$

where υ is the attempt frequency, γ is the overlap factor, R is the separation between the molecules and ΔE is the difference in the polaron energies of the molecules.

The full drift-diffusion equation (Eq. 1.7) is used to describe bulk carrier transport

in organics. The μ in organic films has been shown to be a function of T, F, carrier density (n or p) and disorder which results in broadening of the Gaussian distribution of site densities characterized by the full width at half maximum (FWHM) of the DOS σ_D [72]. Various models have been proposed to relate these parameters including thermally activated mobility:

$$\mu(T) = \mu_\infty exp\left(\frac{-\Delta E_\mu}{k_B T}\right), \tag{1.11}$$

where μ_∞ is the infinite temperature mobility and E_μ is the activation energy. To describe the field dependence, an expression analogous to Poole-Frenkel emission known as the phenomenological Gill equation is used [73]:

$$\mu(F,T) = \mu_\infty exp\left[\frac{-(E_\mu - \beta\sqrt{E})}{k_B T_{eff}}\right], \tag{1.12}$$

where E_o is the zero-field activation energy, β is a empirical parameter related to the field-dependence and $\frac{1}{T_{eff}} = \frac{1}{T} - \frac{1}{T_0}$. T_0 is known as the Gill temperature. Combining the Gaussian disorder model and the correlated disorder model, one can write [74]:

$$\mu = \mu_\infty exp\left[-\left(\frac{3}{5k_B T}\sigma_D\right)^2\right] exp\left\{C_o\sqrt{\frac{qFR}{\sigma_D}}\left[\left(\frac{\sigma_D}{k_B T}\right)^{3/2} - \Gamma\right]\right\}, \tag{1.13}$$

where C_o is a empirical constant and Γ is related to the off-diagonal disorder. Although Eq. 1.11 and Eq. 1.12 are generally sufficient to describe the temperature and field dependence of the organic mobility, Eq. 1.13 derived through Monte-Carlo simulations and accounting for disorder and field-dependence is more generally applicable. If the disorder is significant enough, charge transport through the film cannot be defined by a single mobility, a regime also known as dispersive transport.

The space-charge-limited (SCL) carrier conduction regime is an important analytical result that is commonly observed when the injected charge density, dictated by the capacitance of the film exceeds the total free charge in the organic [75]. Since the

dielectric relaxation in the organic film occurs on a time scale longer than the transit time, there is space-charge buildup. In this regime the electrical field is the sole force driving current conduction. Therefore, Eq. 1.7 simplifies to $J \approx q\mu n_{sc} F$. Combining the drift term with Eq. 1.6, one obtains:

$$\frac{d}{dx}F^2 = \frac{2J}{\epsilon\mu}. \tag{1.14}$$

By assuming a low density of injected charge throughout the layer, one can obtain the electric field, the space-charge voltage and the carrier density through the film as [75]:

$$\begin{aligned} F(x) &= \sqrt{\frac{2Jx}{\epsilon\mu} + F_c^2}, \\ V(x) &= \frac{\epsilon\mu}{3J}\left[\left(\frac{2Jx}{\epsilon\mu} + F_c^2\right)^{3/2} - F_c^3\right] \text{ and} \\ P(x) &= \frac{J}{q\mu}\frac{1}{\sqrt{\frac{2Jx}{\epsilon\mu} + F_c^2}}. \end{aligned} \tag{1.15}$$

Here x is the distance within the film and F_c is the field at the injecting contact. Taking $F_c = 0$ yields the Mott-Gurney relation, $J_{SCL} = \epsilon\mu 9V^2/(8d^3)$. These equations are only valid when traps within the device are filled. When traps are present, one method of accounting for them is to assume an exponential distribution of electron trap states that extends into the E_g as:

$$H_t(E) = H_o exp\left[\frac{E - E_{LUMO}}{k_B T_t}\right], \tag{1.16}$$

where H_o is the trap density of states and T_t determines the trap depth into the LUMO. The corresponding trap-charge-limited (TCL) conduction $J-V$ expression is given as [76]:

$$J_{TCL} = q\mu N_c \left(\frac{\epsilon}{qH_t}\right)^l \left(\frac{l}{l+1}\right)^l \left(\frac{2l+1}{l+1}\right)^{l+1} \frac{V^{l+1}}{d^{2l+1}}, \tag{1.17}$$

where N_c is the density of transport states and $l = T_t/T$. The higher power law dependence in Eq. 1.17 is a result of trap filling, since μ effectively increases as traps get

occupied. A similar treatment is applicable for hole traps near the HOMO.

When both electrons and holes are present in the bulk, recombination and generation processes are again described using Eq. 1.8. The recombination rate of free electrons and holes is approximated by the Langevin rate:

$$R_L = \frac{q(\mu_N + \mu_P)}{\epsilon} np = \gamma_L np, \tag{1.18}$$

which is valid when the carrier mean free path is less than its Coulomb capture radius.

1.6 Optical excitations in organic and inorganic semiconductors

Photon absorption is a common method of generating excited states in semiconductors. The absorption and emission of photons result from transition of charge carriers between two electronic states close to the E_g. The effectiveness of these optical transitions is estimated using the Fermi Golden Rule, derived using time-dependent perturbation theory:

$$\Gamma_{f \leftarrow i} = \frac{2\pi}{\hbar} |\langle \Psi_f | H' | \Psi_i \rangle|^2 \rho_f, \tag{1.19}$$

where Ψ are the wave functions of the states involved in the transition, ρ_f is the density of the final states and H' is the perturbation that drives the transition. Derivation of Eq. 1.19 assumes a sharp transition into a continuum of available states. The optical perturbation from the magnetic vector potential of the photon, A, is written as $H'(r,t) = \frac{iq\hbar}{m_0 c} A \cdot \nabla$ [77]. When the λ of the electromagnetic radiation is much larger than the size of the charge carrier wave functions, to first order using the electric dipole approximation, $H' \approx -q\hat{r} \cdot F$, where $q\hat{r}$ is the dipole moment of the charge between the initial and final state.

1.6.1 Photon interaction with inorganic semiconductors

In inorganics, photon emission occurs by electronic transitions from the E_c to the E_v and photon absorption occurs by electronic transition from the continuum of states in the VB to the continuum of states in the CB. As a result, the absorption profile is generally parabolic, similar to the shape of the DOS shown in Fig. 1.6(a). The emission profile peaks slightly above the E_g and is broadened by band occupation statistics, given by the E_F of the crystal.

Applying the Fermi Golden Rule to band to band excitations, one can write the absorption coefficient for indirect gap and direct gap semiconductors [78]. For direct gap absorption,

$$\alpha(\hbar\omega) = n_r^{-1}\left(\frac{q^2 m_0^{1/2}}{4\pi\hbar^2\epsilon_0 c}\right)\left(\frac{2m^*}{m_0}\right)^{3/2}\left(\frac{2p_{CV}^2}{m_0}\right)\frac{(\hbar\omega - E_g)^{1/2}}{\hbar\omega}, \tag{1.20}$$

where n_r is the index of refraction of the crystal, $m^* = m_{e,R}m_{h,R}/(m_{e,R} + m_{h,R})$ is the reduced effective mass. The $f_{CV} = 2p_{CV}^2/(m_0)$, is the oscillator strength for the transition, and equals 20 eV for most semiconductors, where p_{CV} is the momentum matrix element. For indirect gap materials:

$$\alpha(\hbar\omega) = n_r^{-1}\left(\frac{q^2 m_0^{1/2}}{6\pi\hbar^2\epsilon_0 c}\right)\left(\frac{2m^*}{m_0}\right)^{5/2} f_{CV}^{'}\frac{\left(\hbar\omega - E_g\right)^{3/2}}{\hbar\omega}, \tag{1.21}$$

where $f_{CV}^{'}$ is the oscillator strength of the forbidden transition, usually much less than unity. Eq. 1.20 and Eq. 1.21 are valid at 0 K, where the CB is unoccupied while the VB is full. Photon emission probability by carrier relaxation from an excited states is treated similarly and is given as:

$$P_{em} = \frac{n_r q^2 E p_{CV}^2 (1 + u_E)}{3\pi\epsilon m_0^2\hbar^2 c^3}, \tag{1.22}$$

where $(1 + u_E)$ is related to photon occupation in the cavity and is equal to unity when photons escape after carrier recombination.

1.6.2 Photon interaction with organic semiconductors

Applying the Fermi Golden Rule to the molecular wave function assuming the Born-Oppenheimer approximation, one can write, $\Psi = \chi_v \psi_e \theta_s$, where the terms are the vibrational (nuclear), spatial (electronic) and spin wave functions. Since the perturbation from electromagnetic radiation does not act on the spin or nuclear components of the wave function, one can write:

$$\begin{aligned} \Gamma_{fi} &= \frac{2\pi}{\hbar} |\langle \chi_f \psi_f \theta_f | - q\hat{r} \cdot F | \chi_f \psi_f \theta_f \rangle|^2 \rho_f \\ &\propto F^2 \rho_f |\langle\ \chi_f | \chi_i \rangle|^2 |\langle \psi_f | \hat{r} | \psi_i \rangle|^2 |\langle \theta_f | \theta_i \rangle|^2. \end{aligned} \tag{1.23}$$

The probability of transition is directly proportional to the intensity of illumination ($\propto F^2$) and the density of the final states. Given that Eq. 1.23 is zero if any of the terms are zero, we can now determine various selection rules.

The $|\langle \psi_f | \hat{r} | \psi_i \rangle|^2$ term is the transition dipole moment, which gives the orbital selection rules. Transitions where this term is zero are called dipole-forbidden. The $|\langle\ \psi_f | \psi_i \rangle|^2$ term is called the Frank-Condon factor and indicates that the transition is more probable when the vibrational wave function overlap is large. The last term, $|\langle \theta_f | \theta_i \rangle|^2$, requires that the ground state and excited state have the same spin parity. This is discussed further in the next section.

To elucidate the role of the Frank-Condon factor in optical processes one must relax the Born-Oppenheimer approximation, whereby the nuclei are assumed to be static relative to the electrons. This approximation is not valid on long time scales after photon absorption or emission since the nuclei reorganizes. A qualitative understanding of the vibrational modes of an organic molecule can be gained from the anharmonic Morse potential for a diatomic molecule, given by:

$$E(q) = D_e[1 - exp(\alpha(q - q_o))]^2, \tag{1.24}$$

where D_e is the depth of the potential well relative to the dissociation energy, q is the internuclei distance, q_o is the equilibrium separation, and α is the stiffness of the bond. A plot of the anharmoic potential as a function of inter-nuclei distance is shown in Fig. 1.14. This potential is qualitatively similar to the Lennard-Jones potential, but differs in that when the separation becomes less than q_o, there is a repulsive Coulombic force and, when the separation becomes greater than q_o, there is a attractive bonding force. If the separation becomes large enough, the chemical bond is broken and the molecule dissociates. Inside the well, the available vibrational levels are quantized. Close to the dissociation energy, the states are continuous. The Schrödinger equation can be solved for the potential in Eq. 1.24 to yield the vibrational sublevels:

$$V_n = \left(n + \frac{1}{2}\right)\hbar\omega_o - \left(n - \frac{1}{2}\right)^2 \frac{(\hbar\omega_o)^2}{4D_e}, \tag{1.25}$$

where $\omega_o = \alpha\sqrt{2D_e/m_N}$, m_N is the mass of the nuclei and n is the energy level. Since there is a large difference between the first and second energy levels ($\approx$ 100 meV) as compared to $k_B T$ at RT, generally only the first level is occupied. Further, any additional energy in the system dissipates by releasing the excess energy as phonon or infrared photons on a ps time scale. As a result absorption and emission processes occur from the lowest quantized energy level, also known as Kasha's Rule.

Figure 1.15 shows the overlap between the vibrational wave functions of a ground and excited diatomic molecule. Upon excitation, the equilibrium nuclear coordinates of the molecule shift and the molecule rapidly thermalizes to its lowest vibration energy level. Since optical transitions occur on a faster time scale as compared to shifts in nuclear coordinates (Franck-Condon principle), this results in highest probability of excitation of the $0 \rightarrow 1$ transition and emission through the $1 \leftarrow 1$ transition. The redshift in emission as compared to absorption is known as the Stokes shift.

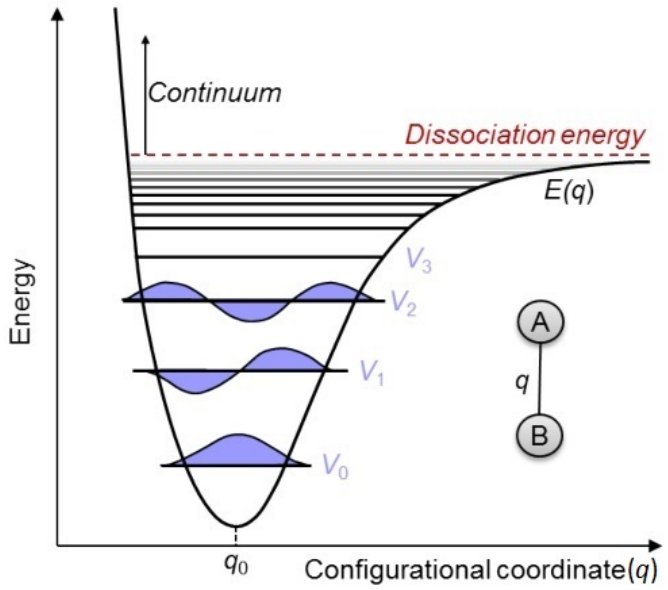

Figure 1.14: The anharmoic Morse potential ($E(q)$, see Eq. 1.24) of a diatomic (A—B) molecule as a function of interatomic distance, where q is the distance between them. When the atoms move closer together than q_o, the equilibrium interatomic distance, they are repelled by Coulombic force. When they move farther apart, they are either attracted back to q_o by the bonding force or the bond dissociates. Near q_o, the potential can be approximated as a harmonic oscillator resulting in equally spaced vibrational levels (V_n). Far from q_o, the spacing between vibrational levels becomes a continuum. Figure reproduced from Ref. [79].

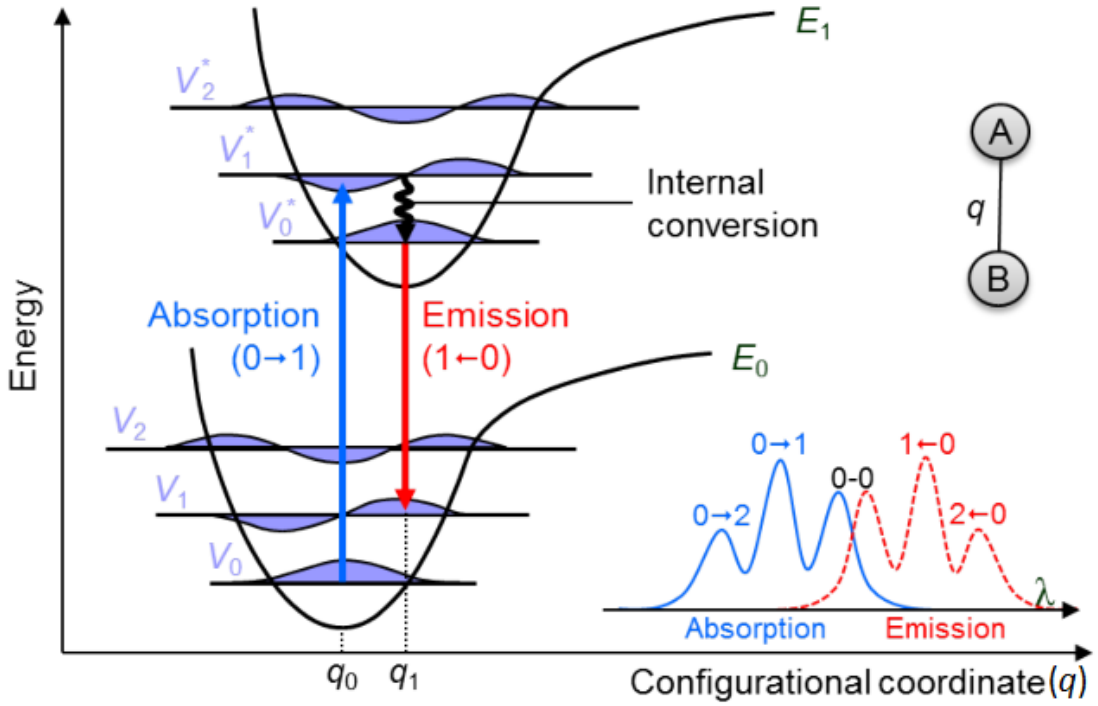

Figure 1.15: Vibrational energy levels of an excited (V_n^*) and ground state (V_n) diatomic (A—B) molecule as a function of interatomic distance (q). The emission and absorption spectra as a function of λ is shown as inset. The equilibrium coordinates shift ($q_0 \rightarrow q_1$) for the excited molecule and the molecule rapidly relaxes to its lowest vibration energy level. Optical transitions occur faster than shifts in nuclear coordinates (Franck-Condon principle). As a result, the strongest electronic state transition during photon absorption ($0 \rightarrow 1$) and emission ($1 \leftarrow 0$) occur from the lowest vibration energy levels to the energy level with the highest wave function overlap at the equilibrium coordinate of the final state. The resulting redshift in emission is known as the Stokes shift. Figure reproduced from Ref. [79].

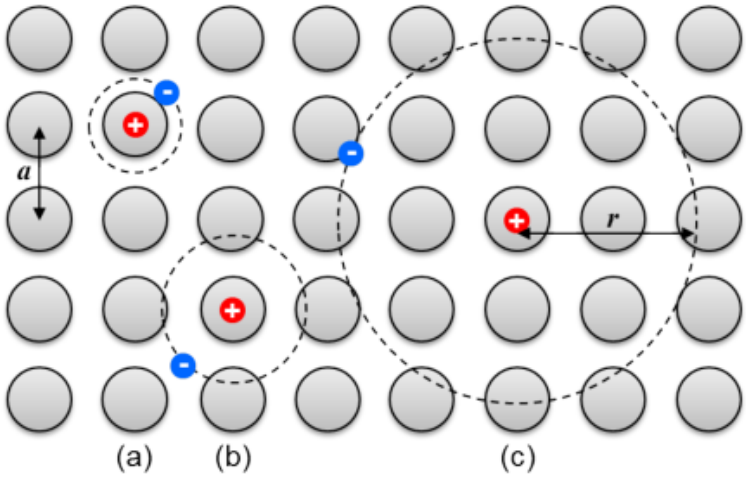

Figure 1.16: Schematic representation of the three types of excitons: (a) localized Frenkel exciton generally found in organic semiconductors, (b) charge-transfer exciton, and (c) WM exciton generally found in inorganic semiconductors. The intermolecular or interatomic distance is a and the exciton radius is r. Figure reproduced from Ref. [79].

1.6.3 Excitons

Excitons are quasi-particles that are Coulombically bound electron-hole pairs. Due to the limited intermolecular interaction in organic semiconductor films, the excitations are localized on a single molecule and are called Frenkel excitons. Frenkel excitons have a high binding energy (E_B) and small radius because of the low dielectric constant of the film, as discussed in §1.2. In contrast, inorganic semiconductor excitons have a large radius as compared to the lattice constant and are called WM excitons. Due to their low E_B, WM excitons are generally only seen at low temperatures. The E_B can be increased by quantum confinement in nanostructures such as quantum well (QW)s or quantum dots. A charge transfer exciton is an intermediate exciton type where the hole and electron reside on nearby molecules or lattice sites. Schematic representation of the three types of excitons is shown in Fig. 1.16.

One can consider an exciton as two paired fermions each with spin angular momentum $s = \frac{1}{2}$. One can define the spin wave function of a fermion as $\theta_s = |s, m_s\rangle$, where

$m_s = \pm\frac{1}{2}$ is the spin quantum number resulting from projection of the spin angular momentum along an arbitrary axis [64]. Then the two spin states can be denoted as 'up' ($|\uparrow\rangle$) and 'down' ($|\downarrow\rangle$). When considering two paired fermions, there are four combinations of the individual fermion spin states, $|\uparrow\uparrow\rangle, |\uparrow\downarrow\rangle, |\downarrow\uparrow\rangle$ and $|\downarrow\downarrow\rangle$. However, these are not the eigenstates of the total spin operator $s^2 = s_1^2 + s_2^2$, where s_1 and s_2 are the spin operators of the individual fermions. For the total spin operator the following are the eigenstates:

$$\begin{aligned} |0,0\rangle &= \frac{1}{\sqrt{2}}[|\uparrow\downarrow\rangle - |\downarrow\uparrow\rangle], \\ |1,+1\rangle &= |\uparrow\uparrow\rangle, \\ |1,0\rangle &= \frac{1}{\sqrt{2}}[|\uparrow\downarrow\rangle + |\downarrow\uparrow\rangle], \text{ and} \\ |1,-1\rangle &= |\downarrow\downarrow\rangle. \end{aligned} \tag{1.26}$$

In Eq. 1.26, the first equation is the antisymmetric singlet state and the last three are the symmetric triplet states. The total wave function of two paired fermions consist of the spatial (ψ_e) and the spin component (θ_s), which together must be antisymmetric upon fermion exchange by the Pauli exclusion principle. Since the ψ_e when two fermions occupy the same orbital is symmetric since it is unaffected by particle exchange, θ_s must be antisymmetric. Therefore, for closed shell molecules where the electrons occupying each orbital are paired, the ground state is a singlet. Since optical excitation conserves spin, in a closed shell molecule photon absorption yields singlet excitons. However, electrical injection yields singlet and triplet excitons in a 1 : 3 ratio. Further, triplet states in a closed shell molecule cannot radiatively decay to the ground state unless there is spin-orbit coupling to give the state singlet character or intersystem crossing (ISC) [65].

To evaluate the relative difference between the singlet and triplet energies, one can construct the spatial component of the two particle wave function, which is symmetric

for the singlet and antisymmetric for the triplet. The energies of the two states are then:

$$E_{singlet} = \frac{q^2}{8\pi\epsilon}\langle\psi_1(1)\psi_2(2)+\psi_1(2)\psi_2(1)\left|\frac{1}{r_{12}}\right|\psi_1(1)\psi_2(2)+\psi_1(2)\psi_2(1)\rangle \text{ and}$$
$$E_{triplet} = \frac{q^2}{8\pi\epsilon}\langle\psi_1(1)\psi_2(2)-\psi_1(2)\psi_2(1)\left|\frac{1}{r_{12}}\right|\psi_1(1)\psi_2(2)-\psi_1(2)\psi_2(1)\rangle. \tag{1.27}$$

Defining

$$J = \frac{q^2}{4\pi\epsilon}\langle\psi_1(1)\psi_2(2)\left|\frac{1}{r_{12}}\right|\psi_1(1)\psi_2(2)\rangle \text{ and}$$
$$K = \frac{q^2}{4\pi\epsilon}\langle\psi_1(1)\psi_2(2)\left|\frac{1}{r_{12}}\right|\psi_1(2)\psi_2(1)\rangle, \tag{1.28}$$

where J is the Coulomb energy and K is the exchange energy, one can rewrite Eq. 1.27 as $E_{singlet} = J + K$ and $E_{triplet} = J - K$. Therefore, the triplet state energy of an exciton is lower than the singlet state energy by twice the exchange energy. For open shell molecules where the electron in the HOMO is unpaired, the ground state is generally a triplet due to the lower energy of the state.

For inorganics the exchange energy is negligible due to the large radius of the exciton and high dielectric constant of the material. As a result, the singlet and triplet energy levels are within $k_B T$.

1.6.4 Energy transfer

Excitons are the primary medium of energy transport and excitation in organic semiconductors. Therefore, accurately modeling their absorption and transport through a thin film is a critical step in predicting device behavior. The absorption or exciton generation profile through a layered stack is a function of λ and is obtained through transfer matrix calculations [80, 81]. The optical constants necessary for the calculation are obtained by variable angle spectroscopic ellipsometry. Once the the exciton generation profile in an organic thin film is known, exciton transfer is modeled by the diffusion

equation:

$$\frac{dn(x)}{dt} = G(x) - \frac{n(x)}{\tau} + \frac{L_D^2}{\tau}\frac{d^2n(x)}{dx^2}. \tag{1.29}$$

Here $G(x)$ is the generation profile, the second term is the natural exciton decay and the third term is Fick's law of diffusion. The τ is the exciton lifetime and $L_D = \sqrt{D\tau}$ is the exciton diffusion length where D is the diffusivity. Solving this equation requires assumptions about exciton behavior at the boundary of the thin film and, generally, either a perfectly blocking (i.e. $\frac{dn}{dx} = 0$) or a perfectly quenching (i.e. $n(x) = 0$) boundary condition is assumed. Once the exciton profile after accounting for exciton diffusion is known, the exciton flux at d is $J_n = \frac{L_D^2}{\tau}\frac{dn}{dx}|_{x=d}$.

There are two primary mechanisms for molecule-to-molecule exciton transfer, FRET and Dexter electron transfer. Since Förster transfer is a dipole-dipole mediated transfer, it is only allowed for singlets. Dexter transfer, on the other hand, occurs by electron exchange and is allowed for both singlets and triplets. The FRET rate between a emitter and acceptor is given by [82, 83]:

$$k_F = \frac{9\kappa^2\eta_{PL}}{128\pi^5\tau r^6 n_r^4}\int \lambda^4 F_D(\lambda)\sigma_A(\lambda)d\lambda. \tag{1.30}$$

Here κ is the dipole orientation factor, $F_D(\lambda) = PL(\lambda)/\int PL(\lambda)d\lambda$ is the normalized fluorescence spectrum of the emitter and $\sigma_A(\lambda) = \alpha(\lambda)MW/(\rho N_A)$ is the absorption cross-section of the acceptor. Here α is the acceptor absorption coefficient, MW is its molecular weight, ρ is its density and N_A is the Avogadro constant. The $\kappa = 0.845\sqrt{2/3}$ for amorphous film with randomly oriented rigid dipoles [84]. The Förster radius R_o is defined as $(k_F\tau r^6)^{1/6}$. At R_o, 50% of the excitons transfer via FRET while the remaining 50% recombine. The Dexter transfer rate as a function of distance R is given as [85]:

$$k_D = \frac{2\pi}{\hbar}\frac{K}{R^2}\sigma_D exp\left(\frac{-2R}{\eta}\right), \tag{1.31}$$

where K is a normalizing constant, η is the effective orbital radius of the final and initial electronic states, and σ_D is the overlap integral of the normalized phosphorescence spectrum of the emitter and the absorption spectrum of the acceptor. Therefore, the Dexter transfer rate decreases exponentially as a function of distance.

1.6.5 Excited state decay pathways

Various radiative and non-radiative pathways are possible for excitons and charges in inorganic and organic semiconductors. In inorganics, radiative emission of carriers occurs by either band-to-band recombination or through formation of an exciton state. Non-radiative recombination occurs via either Auger or Shockley-Read-Hall (SRH) recombination. Auger recombination occurs when two carriers recombine and transfer their energy to a third carrier while SRH recombination occurs when two carriers recombine via localized states within the E_g.

In organic semiconductors, the majority of carriers or photons form excitons before recombination. The various available pathways are summarized in Jablonski diagrams. A generic Jablonski diagram is shown in Fig. 1.17. Photon absorption results in the generation of high energy singlet excitons that relax to the lowest vibrational energy. The singlet exciton can either fluoresce or recombine through non-radiative recombination pathways, or become a triplet state though intersystem crossing (ISC). The fluorescence PL efficiency is then defined as:

$$\eta_f = \frac{k_r}{k_r + k_{nr} + k_{ISC}} = k_r \tau, \tag{1.32}$$

where k_r, k_{nr}, and k_{ISC} are the rates of radiative, non-radiative, and ISC, and τ is the experimentally measured lifetime. The triplet state is generated though ISC, which undergo either phosphorescence or non-radiative recombination. Although this process is spin-forbidden, the efficiency can be significantly enhanced by introduction of a heavy

metal atom core that increases spin-orbit coupling and gives the triplets singlet character. It is this innovation that resulted in the development of the 100% internal quantum efficiency OLED and their subsequent commercialization [86]. If the non-radiative recombination rate is low enough and the singlet and triplet energies are within $2-3\ k_BT$ the triplet can undergo ISC to become a singlet, and subsequently fluoresce. This is observed by delayed fluorescence. Using Fermi Golden Rule and the dipole approximation, the rate of radiative recombination for a particle in a two level system with wave functions, ψ_1 and ψ_2 is:

$$k_r = \frac{\omega^3 n_r}{3\pi\epsilon_0\hbar c^3}\left(q\int \psi_2^*\mathbf{r}\psi_1 d^3r\right)^2 = \frac{q^2\omega^2 n_r f}{2\pi\epsilon_0 m_0 c^3}. \tag{1.33}$$

Here $\mathbf{r}$ is the position. The f is the oscillator strength of the transition, given as:

$$f = \frac{2m_0}{3\hbar^2}\hbar\omega\left(\int \psi_2^*\mathbf{r}\psi_1 d^3r\right)^2. \tag{1.34}$$

1.7 Device operation and characterization

The $J-V$ and external quantum efficiency (EQE) are two of the most fundamental measurements used to characterize OPV and OLED devices. $J-V$ measurements for OPVs are done both in the dark and under illumination, while for OLEDs the $J-V$ is measured while monitoring the device light output. The dark current is the electrical-only behavior, where carriers are injected into the device under forward bias, and subsequently recombine. Under reverse bias, carriers are extracted and there is limited current flow. High performance devices show a sharp exponential increase under forward bias and a low increase in leakage current under reverse bias. For measuring illuminated $J-V$ characteristics, charges are generated within the device through optical excitation. Under reverse bias the extraction of photogenerated carriers is assisted

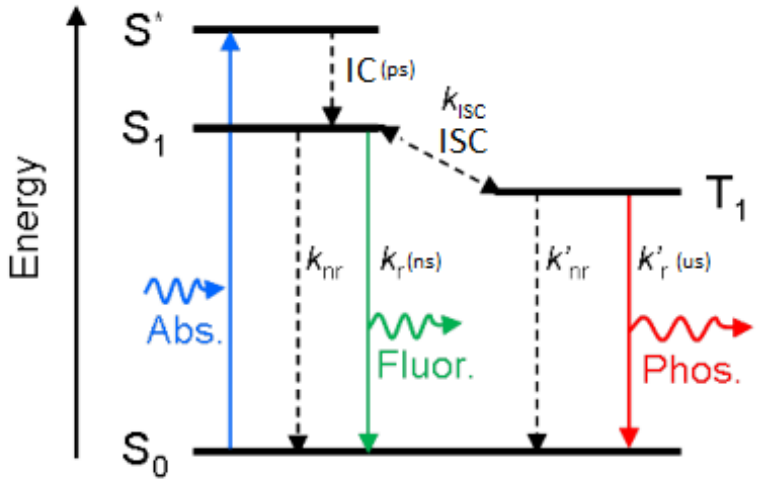

Figure 1.17: A representative Jablonski diagram of electronic states in an organic semiconductor molecule. Photon absorption on a fs time scale leads to exciton excitation from the singlet ground state (S_O) to the singlet excited state (S^*), which then relaxes to the lowest singlet vibrational manifold (S_1) on a ps time scale. The exciton can then recombine non-radiatively with rate k_{nr}, or radiatively with rate k_r by fluorescence on a ns time scale. The singlet exciton can also become a triplet though intersystem crossing (ISC), which can subsequently recombine non-radiatively with rate k'_{nr} or radiatively with rate k'_r, resulting in phosphorescence on a μs time scale. The triplet can also undergo ISC to become a singlet, however this process is highly inefficient in most molecules because the process is spin-forbidden and due to the uphill energy requirement. Figure adapted from Ref. [79].

by an additional applied field. Under high forward bias ($> 2V$), where OLEDs operate, SCL or TCL current is observed.

The power conversion efficiency of an OPV is given as $\eta_{PCE} = FF \cdot J_{sc} \cdot V_{oc}/P$, where P is the incident light power intensity, V_{oc} is the voltage at zero current (open-circuit voltage), J_{sc} is the current density at zero voltage (short-circuit current density) driven by the built-in voltage (V_{bi}), and FF is the fill factor. The FF quantifies the voltage dependence of the $J-V$ in the power quadrant that results in loss from the maximum possible power generation by the cell. A solar cell that can simultaneously operate at V_{OC} and J_{sc} has FF = 100%. The power efficiency for an OLED is often given as the luminous efficiency (lumens/Watt), $\eta_P = \int P(\lambda)L(\lambda)d\lambda/(V_a I)$, where $L(\lambda)$ is the photopic response of the eye, $P(\lambda)$ is the luminous power spectrum, and I is the drive current at an applied voltage (V_a). The measurement of luminous efficiency allows for measurement of the perceived brightness by the human eye.

The processes governing OPV EQE are shown in Fig. 1.18(a). The EQE of an OPV is defined as the number of electrons out per incident photon at a V_a and λ. The J_{sc} is also recovered by multiplying and integrating the EQE at $V_a = 0$ V and the lamp spectrum as a function of λ. Expanding the OPV EQE into its sub-processes, one can write, $\eta_{EQE}(\lambda) = \eta_A(\lambda) \cdot \eta_D(\lambda) \cdot \eta_{CT} \cdot \eta_{DS} \cdot \eta_{CC} = \eta_A(\lambda) \cdot \eta_{IQE}(\lambda)$. Here, η_A is the photon absorption efficiency and η_D is the exciton diffusion efficiency to the HJ, η_{CT} is the charge transfer state formation efficiency, η_{DS} is the charge transfer state dissociation efficiency, and η_{CC} is the charge collection efficiency. Further, η_{IQE} is the internal quantum efficiency (IQE). The η_A and η_D are discussed in §1.6.4. The mechanism for η_{CT} and η_{DS} remain under debate in the field, while η_{CC} is dependent on the charge mobility and conductivity in the bulk.

The processes governing OLED EQE are shown in Fig. 1.18(b). The EQE of an OLED is defined as the number of photons out per injected electron at a given J. Expanding the OLED EQE into its sub-processes, one can write, $\eta_{EQE}(J) = \eta_{CB}(J) \cdot \eta_R(J) \cdot \eta_{OUT}(J, \lambda) =$

$\eta_{IQE}(J) \cdot \eta_{OUT}(J, \lambda)$. Here, η_{CB} is the charge balance efficiency in the emission layer, η_R is the exciton radiative efficiency and η_{OUT} is the photon outcoupling efficiency. While most of these processes have been optimized in state-of-the-art OLEDs, increasing η_{OUT} remains a challenge. Further, at high current densities, various quenching mechanisms (e.g. exciton-polaron quenching) reduce η_R.

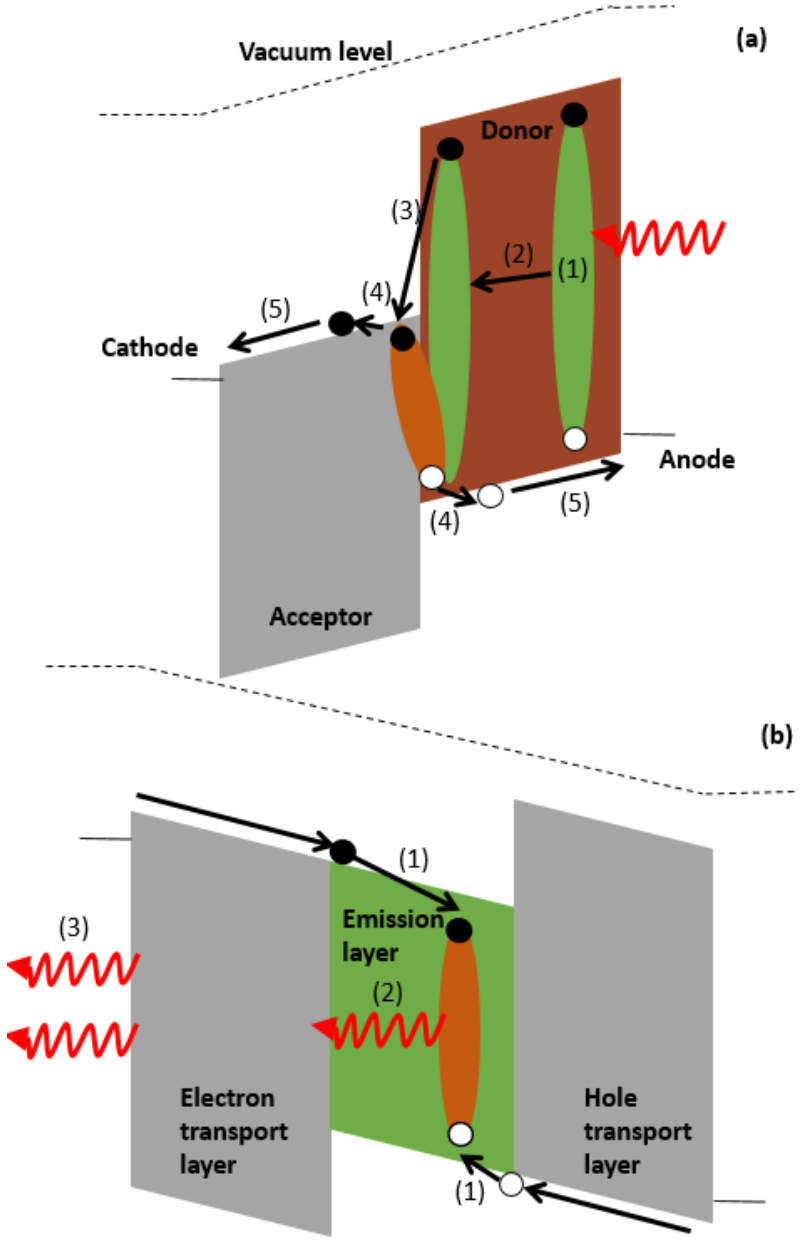

Figure 1.18: (a) The fundamental processes governing OPV efficiency: (1) exciton formation; (2) exciton diffusion; (3) charge transfer state formation; (4) charge transfer state dissociation; and (5) charge collection. (b) The fundamental processes governing OLED efficiency: (1) charge balance; (2) exciton radiative recombination; (3) and photon outcoupling.

Bibliography

[1] Z. I. Alferov, "The semiconductor revolution in the 20th century," *Russ. Chem. Rev.* **82**, 587 (2013).

[2] K. Wandelt, *Surface and interface science, volumes 1 and 2: volume 1 - concepts and methods; volume 2 - properties of elemental surfaces* (Wiley, Weinheim, Germany, 2012), 1010 pp.

[3] T. Tsutsui and M. Terai, "Electric field-assisted bipolar charge spouting in organic thin-film diodes," *Appl. Phys. Lett.* **84**, 440 (2004).

[4] M. Kroger, S. Hamwi, J. Meyer, T. Dobbertin, et al., "Temperature-independent field-induced charge separation at doped organic/organic interfaces: experimental modeling of electrical properties," *Phys. Rev. B* **75**, 235321 (2007).

[5] J. Meyer, M. Kroger, S. Hamwi, F. Gnam, et al., "Charge generation layers comprising transition metal-oxide/organic interfaces: electronic structure and charge generation mechanism," *Appl. Phys. Lett.* **96**, 193302 (2010).

[6] X. Che, X. Xiao, J. D. Zimmerman, D. Fan, and S. R. Forrest, "High-efficiency, vacuum-deposited, small-molecule organic tandem and triple-junction photovoltaic cells," *Adv. Energy Mater.* **4**, 1400568 (2014).

[7] D. R. T. Zahn, G. N. Gavrila, and G. Salvan, "Electronic and vibrational spectroscopies applied to organic/inorganic interfaces," *Chem. Rev.* **107**, 1161 (2007).

[8] S. Avasthi, Y. Qi, G. K. Vertelov, J. Schwartz, A. Kahn, and J. C. Sturm, "Silicon surface passivation by an organic overlayer of 9,10-phenanthrenequinone," *Appl. Phys. Lett.* **96**, 222109 (2010).

[9] N. Li, K. Lee, C. K. Renshaw, X. Xiao, and S. R. Forrest, "Improved power conversion efficiency of InP solar cells using organic window layers," *Appl. Phys. Lett.* **98**, 053504 (2011).

[10] E. H. Sargent, "Colloidal quantum dot solar cells," *Nat. Photonics* **6**, 133 (2012).

[11] O. Malinkiewicz, A. Yella, Y. H. Lee, G. M. Espallargas, et al., "Perovskite solar cells employing organic charge-transport layers," *Nat. Photonics* **8**, 128 (2014).

[12] S. Avasthi, S. Lee, Y.-L. Loo, and J. C. Sturm, "Role of majority and minority carrier barriers silicon/organic hybrid heterojunction solar cells," *Adv. Mater.* **23**, 5762 (2011).

[13] Q. Liu, I. Khatri, R. Ishikawa, A. Fujimori, et al., "Improved photovoltaic performance of crystalline-Si/organic Schottky junction solar cells using ferroelectric polymers," *Appl. Phys. Lett.* **103**, 163503 (2013).

[14] G. Hughes, J. Roche, D. Carty, T. Cafolla, and K. E. Smith, "Core level photoemission and scanning tunneling microscopy study of the interaction of pentacene with the Si(100) surface," *J. Vac. Sci. Technol. B* **20**, 1620 (2002).

[15] G. Salvan and D. R. T. Zahn, "Evidence for strong interaction of PTCDA molecules with defects on sulphur-passivated GaAs(100)," *EPL* **67**, 827 (2004).

[16] A. Hagfeldt, G. Boschloo, L. Sun, L. Kloo, and H. Pettersson, "Dye-sensitized solar cells," *Chem. Rev.* **110**, 6595 (2010).

[17] N. Vlachopoulos, P. Liska, J. Augustynski, and M. Graetzel, "Very efficient visible light energy harvesting and conversion by spectral sensitization of high surface area polycrystalline titanium dioxide films," *J. Am. Chem. Soc.* **110**, 1216 (1988).

[18] G. Itskos, G. Heliotis, P. G. Lagoudakis, J. Lupton, et al., "Efficient dipole-dipole coupling of mott-wannier and frenkel excitons in (ga,in)n quantum well/polyfluorene semiconductor heterostructures," *Phys. Rev. B* **76**, 035344 (2007).

[19] J. J. Rindermann, G. Pozina, B. Monemar, L. Hultman, H. Amano, and P. G. Lagoudakis, "Dependence of resonance energy transfer on exciton dimensionality," *Phys. Rev. Lett.* **107**, 236805 (2011).

[20] Q. Zhang, T. Atay, J. R. Tischler, M. S. Bradley, V. Bulovic, and A. V. Nurmikko, "Highly efficient resonant coupling of optical excitations in hybrid organic/inorganic semiconductor nanostructures," *Nat. Nanotechnol.* **2**, 555 (2007).

[21] R. R. Chance, A. Prock, and R. Silbey, "Molecular fluorescence and energy transfer near interfaces," *Adv. Chem. Phys.* **37**, 1 (1978).

[22] W. Gebauer, A. Langner, M. Schneider, M. Sokolowski, and E. Umbach, "Luminescence quenching of ordered pi-conjugated molecules near a metal surface: quaterthiophene and PTCDA on ag(111)," *Phys. Rev. B* **69**, 155431 (2004).

[23] G. Heliotis, G. Itskos, R. Murray, M. D. Dawson, I. M. Watson, and D. D. C. Bradley, "Hybrid inorganic/organic semiconductor heterostructures with efficient non-radiative energy transfer," *Adv. Mater.* **18**, 334 (2006).

[24] S. Blumstengel, S. Sadofev, and F. Henneberger, "Electronic coupling of optical excitations in organic/inorganic semiconductor hybrid structures," *New J. Phys.* **10**, 065010 (2008).

[25] K. A. S. Araujo, M. de Pauli, S. O. Ferreira, A. Malachias, and L. A. Cury, "Interface engineering to probe exciton energy transfer mechanism in conjugated polymer bilayers," *Org. Electron.* **15**, 3501 (2014).

[26] R. Holmes, S. Kena-Cohen, V. Menon, and S. Forrest, "Strong coupling and hybridization of Frenkel and Wannier-Mott excitons in an organic-inorganic optical microcavity," *Phys. Rev. B* **74**, 235211 (2006).

[27] V. M. Agranovich, Y. N. Gartstein, and M. Litinskaya, "Hybrid resonant organic-inorganic nanostructures for optoelectronic applications," *Chem. Rev.* **111**, 5179 (2011).

[28] M. Slootsky, X. Liu, V. M. Menon, and S. R. Forrest, "Room temperature Frenkel-Wannier-Mott hybridization of degenerate excitons in a strongly coupled microcavity," *Phys. Rev. Lett.* **112**, 076401 (2014).

[29] D. Coles, D. G. Lidzey, G. G. Paschos, J. L. Bricks, et al., "Hybrid organic-inorganic polariton laser," *Sci. Rep.* **7**, 1 (2017).

[30] N. Bansal, L. X. Reynolds, A. MacLachlan, T. Lutz, et al., "Influence of crystallinity and energetics on charge separation in polymer-inorganic nanocomposite films for solar cells," *Sci. Rep.* **3**, 1531 (2013).

[31] U. B. Cappel, S. A. Dowland, L. X. Reynolds, S. Dimitrov, and S. A. Haque, "Charge generation dynamics in CdS:P3HT blends for hybrid solar cells," *J. Phys. Chem. Lett.* **4**, 4253 (2013).

[32] Y. Vaynzof, A. A. Bakulin, S. Gelinas, and R. H. Friend, "Direct observation of photoinduced bound charge-pair states at an organic-inorganic semiconductor interface," *Phys. Rev. Lett.* **108**, 246605 (2012).

[33] M. Eyer, S. Sadofev, J. Puls, and S. Blumstengel, "Charge transfer excitons at ZnMgO/P3HT heterojunctions: relation to photovoltaic performance," *Appl. Phys. Lett.* **107**, 221602 (2015).

[34] H. Lim, H. Kwon, S. K. Kim, and J. W. Kim, "Delayed triplet-state formation through hybrid charge transfer exciton at copper phthalocyanine/GaAs heterojunction," *J. Phys. Chem. Lett.* **8**, 4763 (2017).

[35] X. Liu, J. Gu, K. Ding, D. Fan, et al., "Photoresponse of an organic semiconductor/two-dimensional transition metal dichalcogenide heterojunction," *Nano Lett.* **17**, 3176 (2017).

[36] K. Vandewal, S. Albrecht, E. T. Hoke, K. R. Graham, et al., "Efficient charge generation by relaxed charge-transfer states at organic interfaces," *Nat. Mater.* **13**, 63 (2014).

[37] X. Liu, K. Ding, A. Panda, and S. R. Forrest, "Charge transfer states in dilute donor-acceptor blend organic heterojunctions," *ACS Nano* **10**, 7619 (2016).

[38] A. A. High, E. E. Novitskaya, L. V. Butov, M. Hanson, and A. C. Gossard, "Control of exciton fluxes in an excitonic integrated circuit," *Science* **321**, 229 (2008).

[39] A. Violante, K. Cohen, S. Lazic, R. Hey, R. Rapaport, and P. V. Santos, "Dynamics of indirect exciton transport by moving acoustic fields," *New J. Phys.* **16**, 033035 (2014).

[40] K. V. Raman, "Interface-assisted molecular spintronics," *Appl. Phys. Rev* **1**, 031101 (2014).

[41] C. Wan, Y. Kodama, M. Kondo, R. Sasai, et al., "Dielectric mismatch mediates carrier mobility in organic-intercalated layered TiS2," *Nano Lett.* **15**, 6302 (2015).

[42] L. Pauling, *The nature of the chemical bond and the structure of molecules and crystals: an introduction to modern structural chemistry* (Cornell University Press, Ithaca, USA, 1960), 664 pp.

[43] C. K. Renshaw, "Hybrid organic/inorganic optoelectronics," PhD thesis (The University of Michigan, Ann Arbor, USA, 2014), 248 pp.

[44] A. Barron, *Chemistry of electronic materials* (Connexions, Rice University, 2013), 359 pp.

[45] J. Singh, *Electronic and optoelectronic properties of semiconductor structures*, 1st ed. (Cambridge University Press, Cambridge; New York, 2007), 560 pp.

[46] H. Ibach and H. Luth, *Solid-state physics: an introduction to principles of materials science*, 4th ed. (Springer, Berlin, Germany, 2009), 536 pp.

[47] S. Montanari, "Fabrication and characterization of planar gunn diodes for monolithic microwave integrated circuits," PhD thesis (RWTH Aachen, Aachen, Germany, 2005), 150 pp.

[48] D. K. Maurya, A. Sardarinejad, and K. Alameh, "Recent developments in R.F. magnetron sputtered thin films for pH sensing applications-an overview," *Coatings* **4**, 756 (2014).

[49] N. W. Ashcroft and N. D. Mermin, *Solid state physics*, 1st ed. (Holt, Rinehart and Winston, New York, USA, 1976).

[50] C. Kittel, *Quantum theory of solids*, 2nd ed. (Wiley, New York, USA, 1987), 528 pp.

[51] D. Sholl and J. A. Steckel, *Density functional theory: a practical introduction*, 1st ed. (Wiley-Interscience, Hoboken, USA, 2009), 252 pp.

[52] B. V. V. Zeghbroeck, *Principles of semiconductor devices and heterojunctions*, 1st ed. (Prentice Hall, Upper Saddle River, USA, 2010), 450 pp.

[53] M. L. Cohen and J. R. Chelikowsky, *Electronic structure and optical properties of semiconductors*, Vol. 75, Springer Series in Solid-State Sciences (Springer-Verlag, Berlin, Germany, 1989), 264 pp.

[54] E. U. Rafailov, ed., *The physics and engineering of compact quantum dot-based lasers for biophotonics* (Wiley, Weinheim, Germany, 2014), 264 pp.

[55] S. M. Sze and K. K. Ng, *Physics of semiconductor devices*, 3rd ed. (Wiley-Interscience, Hoboken, USA, 2006), 832 pp.

[56] S. R. Forrest, "The path to ubiquitous and low-cost organic electronic appliances on plastic," *Nature* **428**, 911 (2004).

[57] J. A. Rogers, T. Someya, and Y. Huang, "Materials and mechanics for stretchable electronics," *Science* **327**, 1603 (2010).

[58] S. R. Forrest, "Ultrathin organic films grown by organic molecular beam deposition and related techniques," *Chem. Rev.* **97**, 1793 (1997).

[59] N. C. Giebink, "Properties of excited states in organic light emitting diodes and lasers," PhD thesis (Princeton University, New Jersey, USA, 2009), 251 pp.

[60] M. M. Ling and Z. Bao, "Thin film deposition, patterning, and printing in organic thin film transistors," *Chem. Mater.* **16**, 4824 (2004).

[61] P. E. Burrows, S. R. Forrest, L. S. Sapochak, J. Schwartz, et al., "Organic vapor phase deposition: a new method for the growth of organic thin films with large optical non-linearities," *Journal of Crystal Growth* **156**, 91 (1995).

[62] T. R. Hebner, C. C. Wu, D. Marcy, M. H. Lu, and J. C. Sturm, "Ink-jet printing of doped polymers for organic light emitting devices," *Appl. Phys. Lett.* **72**, 519 (1998).

[63] P. Atkins, L. Jones, and L. Laverman, *Chemical principles*, 6th ed. (W. H. Freeman, New York, USA, 2012), 1024 pp.

[64] J. P. Lowe and K. Peterson, *Quantum chemistry*, 3rd ed. (Academic Press, Burlington, MA, 2005), 728 pp.

[65] P. W. Atkins and R. S. Friedman, *Molecular quantum mechanics*, 5th ed. (Oxford University Press, Oxford, UK, 2010), 592 pp.

[66] M. Pope and C. E. Swenberg, *Electronic processes in organic crystals and polymers*, 2nd ed. (Oxford University Press, New York, 1999), 1328 pp.

[67] R. R. Lunt, "The growth, characterization, and application of highly ordered small molecule semiconducting thin films," PhD thesis (Princeton University, New Jersey, USA, 2010), 239 pp.

[68] H. Ishii and K. Seki, "Energy level alignment at organic/metal interfaces studied by UV photoemission: breakdown of traditional assumption of a common vacuum level at the interface," *IEEE Trans. Electron Devices* **44**, 1295 (1997).

[69] B. Lussem, M. Riede, and K. Leo, "Doping of organic semiconductors," *Phys. Stat. Sol. (a)* **210**, 9 (2013).

[70] I. E. Jacobs and A. J. Moule, "Controlling molecular doping in organic semiconductors," *Adv. Mater.* **29**, 1703063 (2017).

[71] A. Miller and E. Abrahams, "Impurity conduction at low concentrations," *Phys. Rev.* **120**, 745 (1960).

[72] V. Coropceanu, J. Cornil, D. A. da Silva Filho, Y. Olivier, R. Silbey, and J.-L. Bredas, "Charge transport in organic semiconductors," *Chem. Rev.* **107**, 926 (2007).

[73] W. D. Gill, "Drift mobilities in amorphous charge-transfer complexes of trinitrofluorenone and poly-n-vinylcarbazole," *J. Appl. Phys.* **43**, 5033 (1972).

[74] D. Hertel and H. Bassler, "Photoconduction in amorphous organic solids," *ChemPhysChem* **9**, 666 (2008).

[75] A. Rose, "Space-charge-limited currents in solids," *Phys. Rev.* **97**, 1538 (1955).

[76] P. Mark and W. Helfrich, "Space-charge-limited currents in organic crystals," *J. Appl. Phys.* **33**, 205 (1962).

[77] R. H. Bube, *Electronic properties of crystalline solids: an introduction to fundamentals* (Academic Press, New York, USA, 1974), 552 pp.

[78] P. Bhattacharya, *Semiconductor optoelectronic devices*, 2nd ed. (Prentice Hall, Upper Saddle River, USA, 1997), 613 pp.

[79] M. Slootsky, "Manipulating light in organic thin-film devices," PhD thesis (The University of Michigan, Ann Arbor, USA, 2014), 198 pp.

[80] L. A. A. Pettersson, L. S. Roman, and O. Inganas, "Modeling photocurrent action spectra of photovoltaic devices based on organic thin films," *J. Appl. Phys.* **86**, 487 (1999).

[81] P. Peumans, A. Yakimov, and S. R. Forrest, "Small molecular weight organic thin-film photodetectors and solar cells," *J. Appl. Phys.* **93**, 3693 (2003).

[82] T. Forster, "10th Spiers memorial lecture. transfer mechanisms of electronic excitation," *Discuss. Faraday Soc.* **27**, 7 (1959).

[83] S. E. Braslavsky, E. Fron, H. B. Rodriguez, E. S. Roman, et al., "Pitfalls and limitations in the practical use of forster's theory of resonance energy transfer," *Photochem. Photobiol. Sci.* **7**, 1444 (2008).

[84] S. M. Menke and R. J. Holmes, "Exciton diffusion in organic photovoltaic cells," *Energy Environ. Sci.* **7**, 499 (2014).

[85] D. L. Dexter, "A theory of sensitized luminescence in solids," *J. Chem. Phys.* **21**, 836 (1953).

[86] M. A. Baldo, D. F. O'Brien, Y. You, A. Shoustikov, et al., "Highly efficient phosphorescent emission from organic electroluminescent devices," *Nature* **395**, 151 (1998).

CHAPTER II

Theoretical description of current-voltage characteristics of organic-inorganic heterojunction based diodes

The classical description of charge diffusion and recombination in inorganic semiconductor based $p-n$ junction diodes resulted in the Shockley equation [1] that — with many subsequent extensions and modifications — has served as the foundation of semiconductor device physics. Recently, Giebink *et al.* [2] extended this analysis to include organic semiconductors. The work of Renshaw *et al.* that extended it further to include hybrid OI semiconductors [3] is presented in this chapter. As discussed in §1.2 the different bonding energies in organic and inorganic semiconductors leads to vastly different optoelectronic properties in the two material systems. As a result, the optoelectronic processes in hybrid OI semiconductor based diodes require a significantly different physical description. This chapter will detail an analysis that describes the dynamics of charges and excited states in diodes consisting of OI-HJs. The analysis leads to a rigorous description of the $J-V$ characteristics of the hybrid structure, both in the dark and under illumination.

This chapter is organized as follows: first, the physical processes that govern optoelectronic behavior in type II OI-HJs are summarized along with the resulting rate equations. Second, the $J-V$ expression for quasi-equilibrium operation are derived for both ideal and non-ideal OI-HJs. Third, the calculation of $J-V$ for non-equilibrium op-

eration are discussed along with non-idealities originating in the bulk. Fourth, the $J-V$ expression for other possible hybrid diode architectures is discussed. Finally, a comparison of the diode equations for inorganic, organic, and OI semiconductor material systems is presented.

2.1 Optoelectronic processes at type II OI-HJs

The model is developed for an $n-P$ anisotype type II staggered OI-HJ diode, where n refers to electrons as the majority carrier type in the inorganic and P refers to hole polarons as the majority carrier type in the organic. Figure 2.1 shows the energy level diagram of an archetypical type II $n-P$ OI-HJ diode at equilibrium ($V_a = 0$). The behavior of the diode is expected to be dominated by recombination at the HJ at low current (corresponding to reverse bias or at small forward voltage) and the carrier transport properties of the semiconductor bulk at high current (SCL or TCL current). To begin with, we assume, defect states at the OI-HJ are inactive, there is no loss due to trapped charges within the bulk, and there is no injection of charge carriers above the HJ barriers. Indeed, it has been shown that, in some cases, the presence of the organic layer can passivate the inorganic surface [4–6]. Nevertheless, as we find in the experimental work outlined in Chapter IV, interface states play a dominant role in determining the photoresponse of the OI-HJ.

The model is based on the injection and generation of charges in the inorganic, and the injection of charges and generation of Frenkel excitons in the organic layer. The Frenkel excitons or charges can then migrate to the interface where though an HCTE, a state analogous to a polaron-pair state, they can either rapidly dissociates into free charge or recombine. The photocarrier generation in the diode occurs via one of three mechanisms: (i) direct band-to-band absorption of a photon in the inorganic that results in direct generation of free carriers; (ii) photon absorption in the organic leading to exciton generation, which subsequently diffuses to the junction; and (iii)

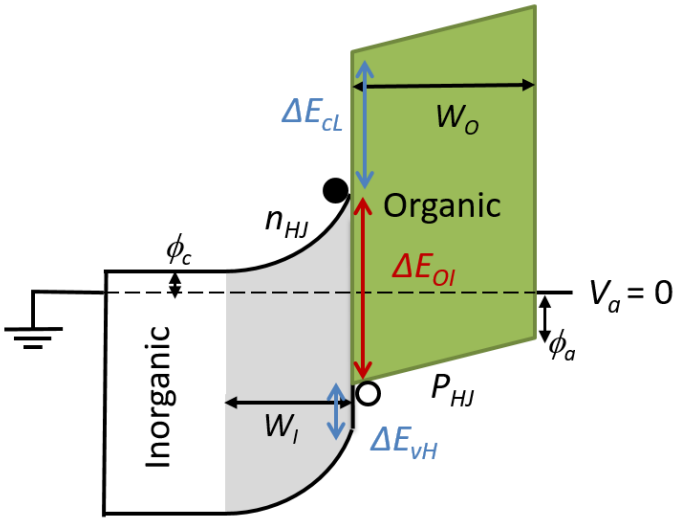

Figure 2.1: Equilibrium energy level diagram for a hybrid $n-P$ OI-HJ based diode. The depletion region formed in the inorganic is indicated in gray and has a width of W_I. The organic layer thickness is W_O and is fully depleted due to its low intrinsic carrier density. As a result, it is assumed to have a uniform field across. The cathode and anode form a carrier injection barrier of ϕ_c and ϕ_a with the organic and inorganic layer, respectively. Electron and hole density at the OI-HJ are n_{HJ} and P_{HJ}, respectively. The interface energy gap, determined by the difference in the E_c and HOMO is ΔE_{OI}. The difference in the E_c minimum energy and the organic LUMO is ΔE_{cL} and the E_v and the organic HOMO is ΔE_{vH}. Figure adapted from Ref. [3].

direct absorption by the HCTE state at the OI-HJ. In the first case, the majority carrier is extracted through the cathode while the minority carrier diffuses to the OI-HJ. The minority carrier can then either traverse over the OI-HJ through the organic layer to be collected by the anode or recombine through the HCTE state at the heterointerface. If the minority carrier diffusion length in the inorganic is higher than the layer thickness, the collection efficiency is only limited by interface bimolecular recombination. In the second case, once the exciton diffuses to the OI-HJ the electron transfers to the inorganic through either a resonant or non-resonant process and forms the HCTE, depending on the relative magnitudes of the organic and inorganic energy gaps and their offsets (i.e. type I, II, or III). The HCTE then dissociates and the hole and electron are collected at the electrodes, returning the organic back to its ground state. If there is a high density of interface traps, the HCTE and/or its excitonic precursor can also rapidly recombine. This process is schematically shown in Fig. 2.2. Since the third case usually has a low absorption cross section and, hence, is unlikely to play a significant role in the OI-HJ optoelectronic properties, we do not consider it in the subsequent discussion. In the dark, forward biasing the diode results in electron and hole injection from the cathode and anode respectively, that undergo bimolecular recombination at the OI-HJ.

The HCTE then is a *generally* unstable precursor to bimolecular recombination of carriers to the ground state or, alternatively, to exciton dissociation by generating free electrons at the OI-HJ in the inorganic and free hole polarons in the organic layers, respectively. Its properties are fundamental to determining the optoelectronic properties of OI-HJ diodes. In cases where the E_g of the inorganic is lower than the exciton energy in the organic, the exciton can potentially Förster transfer to the inorganic [8, 9], thereby circumventing the formation of the HCTE. Hence, both the relative magnitudes of the organic and inorganic energy gaps, the magnitude of the OI-HJ energy offset, and the presence of interface traps determine the excited state dynamics.

Figure 2.3 summarizes the processes that occur in a OI-HJ diode, along with the

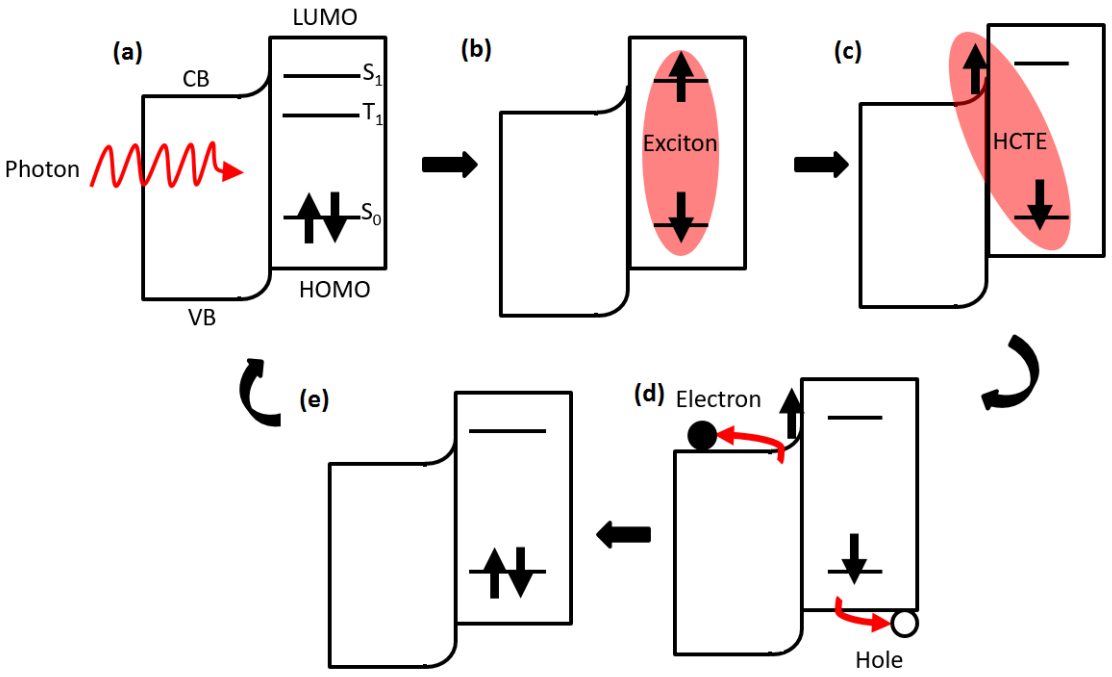

Figure 2.2: The process of charge generation via the generation of excitons in the organic semiconductor of an OI-HJ diode: (a) photon absorption in the organic; (b) exciton formation; (c) hybrid charge transfer exciton formation at the OI-HJ following exciton diffusion; (d) charge generation and extraction; and (e) return of the organic to the ground state (S_0). Here, S_1 is the first singlet excited state of the organic. This process can also occur via the T_1 exciton state if the S_1 exciton state intersystem crosses. Figure adapted from Ref. [7].

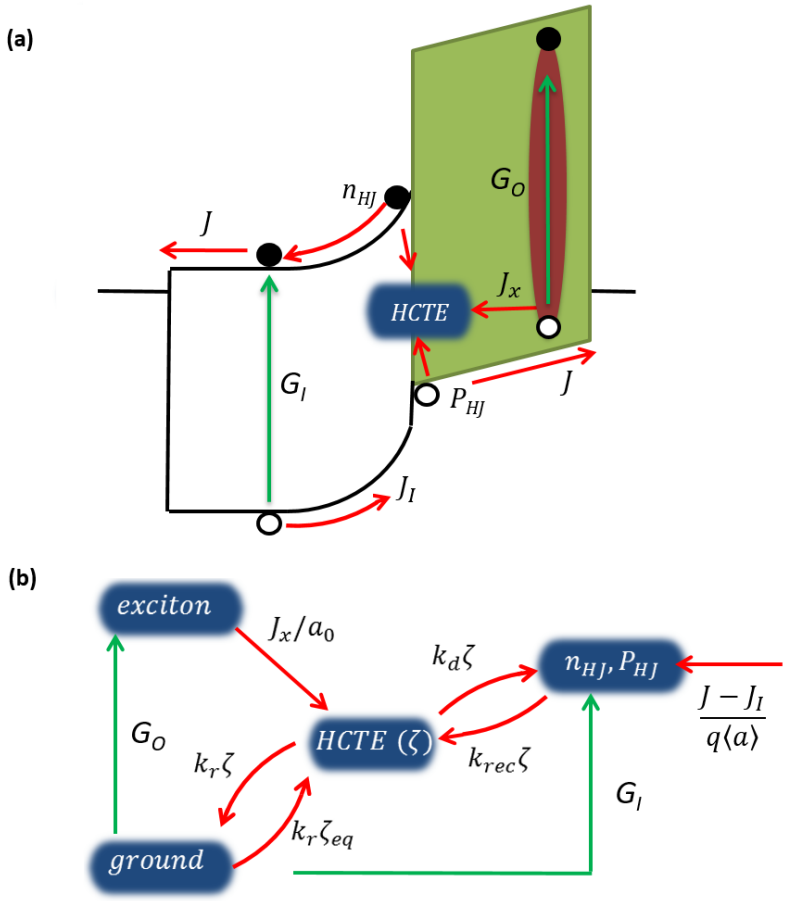

Figure 2.3: (a) Photon absorption in the inorganic semiconductor (G_I) leads to direct free carrier generation while photon absorption in the organic semiconductor (G_O) leads to exciton generation. To generate free carriers, the exciton must subsequently travel to the OI-HJ to dissociate through the HCTE. Photogenerated or injected free electrons in the inorganic layer (n_{HJ}) or free holes in the organic layer (P_{HJ}) can recombine at the OI-HJ through the HCTE. (b) State diagram summarizing the processes that occur at the OI-HJ in a region of width $\langle a \rangle$. Excitons from the organic layer dissociate at a rate $J_x/\langle a \rangle$ to form HCTEs (ζ). The HCTEs recombine and dissociate at rates k_r and k_d, respectively. Carriers near the interface can also recombine at rate k_{rec} to form the HCTE. The P_{HJ} is also populated at a rate $J_I/(q\langle a \rangle)$, where J_I is the current density due to the minority carriers that are photogenerated in the inorganic and are extracted through the organic layer. Figure adapted from Ref. [3].

dynamics at a characteristic "interfacial active width" of $\langle a \rangle$, which corresponds to the characteristic HCTE diameter. We can also define $A_{OB} = \frac{4}{3}\pi\left(\frac{\langle a \rangle}{2}\right)^3$ as the characteristic volume occupied by the state. The electron density in the inorganic and hole density in the organic at the HJ, n_{HJ} and P_{HJ}, respectively, are captured at a rate $k_{rec} n_{HJ} P_{HJ}$ to form HCTEs with density ζ. The corresponding rate equations for ζ, n_{HJ} and P_{HJ} as a function of time, t, are given by:

$$\begin{aligned} \frac{d\zeta}{dt} &= -k_r(\zeta - \zeta_{eq}) - k_d\zeta + k_{rec} n_{HJ} P_{HJ} + \frac{J_x}{\langle a \rangle} \\ \frac{dn_{HJ}}{dt} &= -k_{rec} n_{HJ} p_{HJ} + k_d\zeta + \frac{J_e}{q\langle a \rangle} \\ \frac{dP_{HJ}}{dt} &= -k_{rec} n_{HJ} p_{HJ} + k_d\zeta + \frac{J_h - J_I}{q\langle a \rangle} \end{aligned} \tag{2.1}$$

where k_r and k_d are the rates at which the HCTE recombines to the ground state and into free carriers, respectively. The equilibrium density of HCTEs, ζ_{eq}, is given by $\zeta_{eq} = k_{rec} n_{HJ,eq} P_{HJ,eq} / k_{d,eq}$. Equilibrium corresponds to $V_a = 0$ in the absence of illumination. Since there is no photogeneration or injection of electrons in the organic layer, the current is carried by holes, J_h. Further, the minority carrier current in the inorganic, J_I, is extracted through the organic. By recognizing current continuity throughout the device, we can write $J_e + J_I = J_h \equiv J$. The equations for n_{HJ} and P_{HJ} in Eq. 2.1 thus become symmetric. In steady-state the rate equations can be solved by setting them equal to zero to eliminate ζ. Hence the current is given by:

$$J = q\langle a \rangle k_{rec}(1 - \eta_d)\left(n_{HJ} P_{HJ} - \frac{k_d}{k_{d,eq}} n_{HJ,eq} P_{HJ,eq}\right) - J_{ph}. \tag{2.2}$$

Here $J_{ph} = qJ_x\eta_d - J_I$ is the total photocurrent, which is the sum of the current generated by organic exciton dissociation and the and direct current generated in the inorganic and the HCTE dissociation efficiency is $\eta_d = k_d/(k_d + k_r)$.

2.2 $J-V$ expressions under quasi-equilibrium condition

If J is sufficiently small so that the electron and hole quasi-Fermi levels ($E_{F,n}$ and $E_{F,P}$) are constant throughout the respective layers, the interface carrier density are given by the Boltzmann approximation as:

$$\begin{aligned} n_{HJ} &= N_c exp\left(-\frac{\phi_I}{k_B T}\right) exp\left(\frac{qV_I}{k_B T}\right) = n_c exp\left(\frac{qV_I}{k_B T}\right) \\ P_{HJ} &= N_{HOMO} exp\left(-\frac{\phi_O}{k_B T}\right) exp\left(\frac{qV_O}{k_B T}\right) = P_c exp\left(\frac{qV_O}{k_B T}\right). \end{aligned} \tag{2.3}$$

Here, N_{HOMO} and N_c are the effective DOS of the HOMO of the organic and of the CB of the inorganic, and ϕ_O and ϕ_I are the injection barriers into the organic (from the anode) and inorganic (from the cathode) as shown in Fig. 2.1. The V_I and V_O are the voltage drops across the organic and inorganic layer, respectively. In case of a thick inorganic layer, due to the high carrier density, the depletion width does not extend into the contact. Then, $\phi_I = E_c - E_{F,n}$ in the undepleted equilibrium region. In this case, n_c, the electron density at equilibrium is determined by the ionized dopant density (N_D). In the organic layer, P_c is the hole density in the organic at the anode contact. Due to the low intrinsic carrier density and its thin film nature, the entire film is fully depleted of mobile polarons. Hence the field across the layer is assumed to be uniform and is given by $F_O = V_O/W_O$, where W_O is the organic layer thickness. Plugging Eq. 2.3 into Eq. 2.2 we obtain:

$$J = q\langle a\rangle k_{rec} N_{HOMO} N_c (1-\eta_d) exp\left(-\frac{\Delta E_{OI}}{k_B T}\right)\left(exp\left(\frac{qV_a}{k_B T}\right) - \frac{k_d}{k_{d,eq}}\right) - J_{ph}. \tag{2.4}$$

Here, the CB minimum and HOMO energy difference at the OI-HJ is $\Delta E_{OI} = V_{bi} + \phi_O + \phi_I$. The V_{bi} is determined by the difference in the inorganic Fermi level and the anode work (modified by any energy level shifts due to interface dipoles). The V_a is related to the voltage dropped across each layer and the built-in voltage by $V_a = V_O + V_I + V_{bi}$.

Next, the case of high density of interface trapped charge is considered. In organic

semiconductors the traps originate from morphological defects, impurities and variations in molecular conformations and configurations. In inorganic semiconductors the traps result from impurities, atomic vacancies, and crystal dislocations. The trap density of states in thin films with disorder-induced transport level broadening that lack a sharp band edge is often accurately described using [10, 11]:

$$P_{HJ,t} = H_O exp\left(\frac{E_{HOMO} - E_{F,P}}{k_B T_{t,O}}\right) = H_O\left(\frac{P}{N_{HOMO}}\right)^{1/l_o}, \tag{2.5}$$

where H_O is the trap density, $T_{t,O}$ is the characteristic trap temperature and $l_o = T_{t,o}/T$ determines the depth of the trap distribution. In addition, as discussed in §1.5.4, in organic films the conduction level density of states is often treated as a Gaussian distribution that is approximated by an exponential near the energies of the frontier orbital. For generality, we use a similar trap profile with parameters $H_I, T_{t,I}$ and l_I, near the inorganic E_c. This has been shown to be suitable for disordered inorganics [12, 13]; however, crystalline inorganics are typically characterized by discrete trap levels, where, $n_{HJ,t} = H_I exp(-\frac{E_c - E_{F,n} - E_t}{k_B T})$, and E_t is the trap energy.

We assume that interface recombination is dominated by the recombination of free carriers with trapped charge. We can then write the $J-V$ expression as two processes in parallel, where the first one is the free electron to trapped hole polaron ($n_{HJ} \rightarrow \mathrm{P}_{HJ,t}$) recombination and the second one is the trapped electron to free hole ($n_{HJ,t} \rightarrow \mathrm{P}_{HJ}$) recombination. In making this assumption, we neglect the contribution of free electron to free hole ($n_{HJ} \rightarrow \mathrm{P}_{HJ}$) recombination and trapped electron to trapped hole polaron ($n_{HJ,t} \rightarrow \mathrm{P}_{HJ,t}$) recombination, both of which are expected to be negligible. We can then write:

$$\begin{aligned} J = q\langle a\rangle(1-\eta_d)\Bigg[& k_{rec,n} N_c H_O \left(-\frac{\alpha_O}{k_B T}\right)\left(exp\left(\frac{qV_a}{n_O k_B T}\right) - \frac{k_d}{k_{d,eq}}\right) \\ & + k_{rec,p} N_{HOMO} H_I exp\left(-\frac{\alpha_I}{k_B T}\right)\left(exp\left(\frac{qV_a}{n_I k_B T}\right) - \frac{k_d}{k_{d,eq}}\right)\Bigg] - J_{ph}, \end{aligned} \tag{2.6}$$

where $k_{rec,n}$ and $k_{rec,p}$ are the recombination rates for free electrons with trapped holes

and free holes with trapped electrons. Further, α_O and α_I are the saturation current activation energies, and n_O and n_I are the idealities, defined as:

$$\begin{aligned}
\alpha_O &= \frac{\Delta E_{OI}}{n_o} + \frac{l_O - 1}{l_O}(\delta_O \phi_I - \delta_I \phi_O), \\
\alpha_I &= \frac{\Delta E_{OI}}{n_I} + \frac{l_I - 1}{l_I}(\delta_I \phi_O - \delta_O \phi_I), \\
n_O &= \frac{l_O}{\delta_I(l_O - 1) + 1} \text{ and} \\
n_I &= \frac{l_I}{\delta_O(l_I - 1) + 1}.
\end{aligned} \tag{2.7}$$

Here $\delta_O = V_O/(V_a - V_{bi})$ and $\delta_I = V_I/(V_a - V_{bi})$ are the fractions of the V_a dropped across the organic and inorganic layers, respectively. In the case of discrete trap states present at the inorganic surface, $\alpha_I = -E_t$.

At low currents, the δ_O and δ_I are analytically solvable for both the case of a thin and thick inorganic layer. When the organic and inorganic layers are thin and moderately doped (as is generally the case for organics [14]), they become fully depleted once in contact. For example, for $n = 10^{15}$ cm^{-3}, $V = 0.5$ V and $\epsilon_I = 35$ the depletion width is $W = \sqrt{2\epsilon_I V_{bi}/(qn)} > 1\mu$m. As a result the field across each layer is assumed to be uniform. Using continuity of the electric displacement at the OI-HJ (i.e. $\epsilon_I F_I = \epsilon_O F_O$, see Eq. 1.6), we write, $\delta_I = 1/(1 + \frac{\epsilon_I W_O}{\epsilon_O W_I})$. This assumption is valid at low carrier densities when there is limited charge accumulation at the OI-HJ. Here, F_I and F_O are the field in the organic and inorganic layers, respectively, and W_I is the thickness of the inorganic layer.

When the inorganic layer is thick, it is only partially depleted. When the inorganic side of the junction is not fully depleted, the δ_O and δ_I are a function of V_a. To estimate the voltage dependence, the depletion width approximation is used to determine the resulting field at the inorganic side of the OI-HJ using:

$$Q_I = \pm\sqrt{2k_B T q \epsilon_I}\sqrt{n_c\left[exp\left(-\frac{qV_I}{k_B T}\right) - \frac{qV_I}{k_B T} - 1\right]}. \tag{2.8}$$

The exponential dominates under forward bias while the $qV_I/(k_BT)$ dominates under reverse bias. Then the field at the organic side of the OI-HJ is determined using the continuity of the electric displacement, and the resulting voltage across the organic is calculated by using the uniform field approximation outlined above. This calculation is iteratively repeated at every voltage step to calculate δ_O and δ_I as a function of V_a.

Combining the prefactor in Eq. 2.6 in a single term, we can write the familiar ideal diode equation, analogous to those derived by Shockley [1] and Giebink *et al.* [2]:

$$\begin{aligned} J = J_{SO,T}\left[exp\left(\frac{qV_a}{n_O k_B T}\right)-1\right] \\ +J_{SI,T}\left[exp\left(\frac{qV_a}{n_I k_B T}\right)-1\right]-J_{ph}, \end{aligned} \tag{2.9}$$

here $J_{SO,T}$ and $J_{SI,T}$ are the saturation currents as defined in comparison Eq. 2.6.

In the limit that the HCTE E_B is $< k_BT$, the bound state readily dissociates and the HCTE is effectively coupled to the bath of free carriers (i.e. $k_d = k_{rec}/A_{OB} >> k_r$). Then $\eta_d \rightarrow 1$ and the prefactor $k_{rec}(1-\eta_d)$ in Eq. 2.6 reduces to $A_{OB}k_r$. Alternatively, the exciton precursor may both efficiently couple to the HCTE but also undergo extremely rapid quenching by surface states at the inorganic interface (i.e. $k_d << k_{rec}/A_{OB} = k_r$). In this case, $\eta_d \rightarrow 0$, and the prefactor $k_{rec}(1-\eta_d)$ reduces to k_{rec}.

2.3 *J – V* expressions under non-equilibrium conditions and non-idealities in the bulk

At high current, there is a departure from equilibrium and the behavior of $J-V$ in OI-HJ diodes becomes limited by the transport properties of the organic bulk. As a result, $E_{F,n}$ and $E_{F,P}$ are no longer flat across the layer. Further, charge carriers accumulated at the heterointerface screen the field. As a result, the δ_O and δ_I become a non-analytical function of V_a. To obtain the δ_O and δ_I, the coupled drift-diffusion (Eq. 1.7) and Poisson equation (Eq. 1.6) need to be solved in each of the layers with

the appropriate boundary conditions. The boundary conditions are derived from the current and electric displacement continuity across the OI-HJ, and the contact barriers.

Under these conditions Equation 2.3 can be modified as:

$$P_{HJ} = P_c exp\left(\frac{qV_O - \Delta E_{F,P}}{k_B T}\right), \tag{2.10}$$

and the change in quasi-Fermi level across a layer given as:

$$\Delta E_{F,P} = \frac{1}{\mu_O} \int_0^{W_O} \frac{1}{P(x)} dx. \tag{2.11}$$

Since the carrier mobility in inorganic semiconductors is significantly higher than that of organic semiconductors, and the change in quasi-Fermi level is inversely proportional to the mobility, the change in $\Delta E_{F,n}$ is assumed to be negligible. The current in the non-equilibrium case is obtained with the transformation $V_a \rightarrow V_a - \Delta E_{F,P}$ in Eq. 2.9. At sufficiently high driving voltage, the current is limited by the series resistance (R_S) of the contacts and the active layers which are accounted for with the transformation $V_a \rightarrow V_a - R_s J$ in Eq. 2.9.

An analytical solution for $\Delta E_{F,P}$ can be derived when transport in the organic is SCL. The hole density on the organic side of the HJ can be written as a combination of the equilibrium and non-equilibrium solutions ($P_{HJ} = P^O_{HJ} + P^{SC}_{HJ}$). The P^O_{HJ} is given in Eq. 2.3 and P^{SC}_{HJ} is given in Eq. 1.15. The P_c in Eq. 2.10 when $J \neq 0$ is now $P_c^{'} = P_c + J/(q\mu_O F_c)$. Thus:

$$\Delta E_{F,P} = qV_O^0 + qV_O^{SC} - k_B T ln\left[\frac{P^{SC}_{HJ}}{P_c^{'}} + \frac{P_c}{P_c^{'}} exp\left(\frac{qV_o}{k_B T}\right)\right]. \tag{2.12}$$

In addition to the processes outlined for photocurrent in the OI-HJ diode in §2.1, the exciton can also dissociate in the organic bulk. This is known as photoconductivity [15] and results in a linear slope in photocurrent as a function of voltage. This process is generally highly inefficient due to the high E_B of excitons in organics. Recently

however, efficient exciton dissociation has been reported in thin (< 10 nm) organic films, likely due to the high V_{bi}. The exciton diffusion length is also thermally activated [16] resulting in a temperature activation of J_x. Finally, when the exciton dissociates through the HCTE state, there is additional kinetic energy available for the process due to the electron moving from the organic LUMO to the inorganic E_c. This can potentially result in a different rate for exciton dissociation though the HCTE state as compared to the free carrier recombination though the state. This process of "hot exciton dissociation" remains under debate for excitonic hetereojunctions [17, 18]. Recently however, a consensus has started to emerge that since vibronic relaxation occurs on a ps time scale as compared to free carrier generation, which occurs on a sub-ns time scale, hot exciton dissociation is unlikely, at least at excitonic junctions.

The framework for understanding the charge generation and recombination dynamics in OI-HJ devices presented here can easily be extended to include additional processes in the bulk such as the field and carrier density dependence of carrier mobility in the organic and SRH generation and recombination statistics in the depletion region of the inorganic. The quantitative treatment for some of these processes is discussed in §1.5.4 and §2.4.

2.4 *J – V* expressions for other OI-HJ architectures

The model discussed thus far was developed to describe an $n-P$ junction dominated by interfacial recombination. It is straightforward to modify the model to describe the $J-V$ of other hybrid device architectures. Figure 2.4(a) shows the case of a type II $n-P$ junction with a small VB maximum and HOMO offset energy at the OI-HJ (ΔE_{vH}) such that current is dominated by injection over the barrier under forward bias. Carrier hopping in the organic suggests that the injection rate for a single carrier can be described as $k_{hop} = \upsilon exp(-\Delta E_{vH}/k_B T)$, where υ is the hopping attempt frequency. The forward bias current is then given by $J = q a_O P_{HJ} k_{hop}$, where a_O is the radius of each

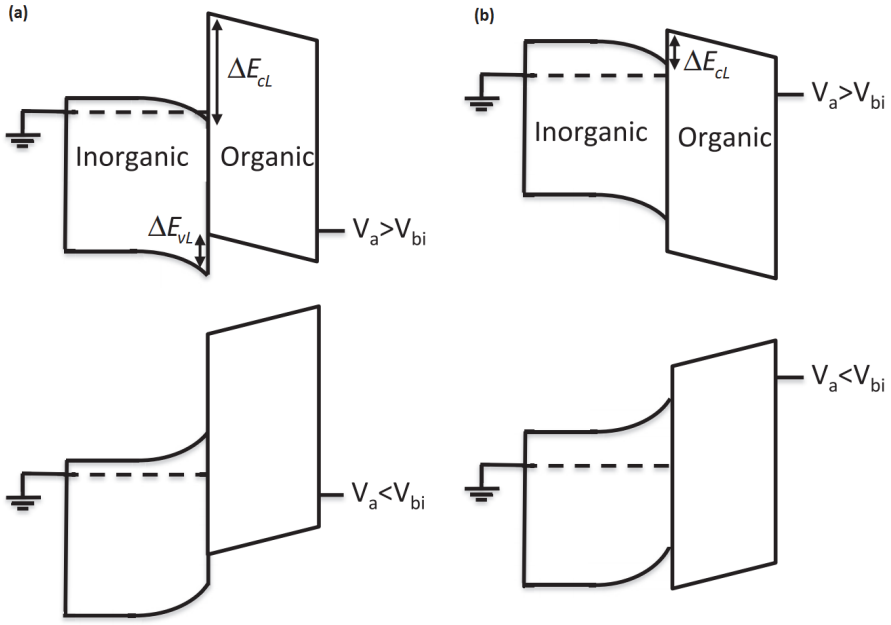

Figure 2.4: Alternative current conduction pathways for (a) type II $n-P$ and (b) type I $n-N$ OI-HJ diodes under forward ($V_a > V_{bi}$) and reverse bias ($V_a < V_{bi}$) bias. In the $n-P$ case, upon forward bias, holes are injected as minority carriers into the inorganic VB from the organic HOMO over ΔE_{vH}. The minority carriers recombine with free electrons in the inorganic bulk. Upon reverse bias, the current is dominated by SRH generation in the depletion region or minority carrier diffusion in the inorganic. In the $n-N$ case the forward bias current is limited by thermionic emission over the ΔE_{cL} into the organic HOMO. The reverse bias current is limited by space-charge in the organic layer. Figure adapted from Ref. [3].

polaron. Under reverse bias, the current is limited by SRH generation in the depletion region, or by minority carrier diffusion from the inorganic bulk. The $J-V$ relationship for the device is thus given as:

$$J = \upsilon q a_O P_c exp\left(\frac{qV_a - \Delta E_{vH}}{n_{therm} k_B T}\right) - \frac{q n_i W_D}{\tau_g} - q\sqrt{\frac{D_I}{\tau_I}}\frac{n_i^2}{N_D}. \tag{2.13}$$

Here, we have used Equation 2.3 for P_{HJ}. The intrinsic carrier density in the inorganic $n_i = \sqrt{N_c N_v} exp(-E_g/2k_B T)$, τ_g is the SRH generation rate, $W_D = \sqrt{(2\epsilon_I \epsilon_0 V_I / qN_D)}$ is the depletion width, D_I is the minority carrier diffusion length, τ_I is the minority carrier lifetime, N_D is the ionized dopant density in the inorganic, and n_{therm} is the ideality factor.

Figure 2.4 (b) shows a type I $n-N$ junction where current is limited by thermionic emission over CB minimum and LUMO offset energy at the OI-HJ (ΔE_{cL}) into the organic under forward bias. The reverse bias current is limited by transport through the organic film. The resulting current is given by:

$$J = A^* T^2 exp\left(\frac{-\Delta E_{cL}}{k_B T}\right) exp\left(\frac{qV_a}{n_{therm} k_B T}\right) - f(V_O), \tag{2.14}$$

where A^* is the effective Richardson constant. Here $f(V_O)$ is the current limiting mechanism in the organic layer. At low voltages, it's ohmic conduction and, at high voltages, it is SCL (Eq. 1.15) or TCL current (Eq. 1.17). Under forward bias, both devices behave as diodes (exhibiting exponential $J-V$), but the reverse (or leakage) characteristics deviate from a traditional Shockley diode behavior.

2.5 Universal ideal diode behavior

Equation 2.4 resembles the ideal diode equation for excitonic HJs and also inorganic $p-n$ junction diodes — the essential form remains the same regardless of whether the

diode is governed by drift and diffusion processes, by SRH generation and recombination statistics [19, 20]. Across all these systems, the universal form of the equation is given by:

$$J = J_s\left[exp\left(\frac{qV}{nk_BT}\right) - \chi(V)\right] - J_{ph}. \tag{2.15}$$

Here J_s is the saturation current density, n is the ideality factor, $\chi(V)$ is the bias dependent reverse-bias factor (note $\chi(0) \rightarrow 1$) and J_{ph}, the photocurrent, have different functional forms in the various material systems due to the different processes that govern current in these materials. Table 2.1 lists the definitions of these parameters for the different material systems when the current is controlled by only one of the two contacting materials. The universal form of the diode equation originates from the commonality of the fundamental physics governing carrier dynamics in these material systems. Since Boltzmann statistics govern the free carrier distribution, this results in an exponential increase in carrier density and current response to an applied field. The increase in carrier density is balanced by varied carrier generation and recombination processes in the case of the three junctions. Indeed, the primary distinguishing feature across these junctions is the specific physics at play in the generation and recombination processes.

Table 2.1: Comparison of the diode equations for various material systems. They all have the general form $J = J_s\left[exp\left(\frac{qV}{nk_BT}\right) - \chi(V)\right] - J_{ph}$, where J_s is the saturation current density, n is the ideality factor, $\chi(V)$ is the bias dependent reverse-bias factor and J_{ph} is the photocurrent. In writing the parameters, the current is assumed to be controlled by only one of the two contacting materials.

Equation	$\boldsymbol{J_s}$	$\boldsymbol{J_{ph}}$	$\boldsymbol{\chi}$	$\boldsymbol{n}$
Inorganic (diffusion)	$q\left[\frac{D_p n_i^2}{L_p N_D} + \frac{D_n n_i^2}{L_n N_A}\right]$	J_I	1	1
Inorganic (generation, recombination)	$\frac{qn_i}{\tau_g}\left(\frac{k_BT}{q}\frac{2\epsilon}{qWN_D}\right)\frac{D_n n_i^2}{L_n N_A}$	J_I	$\frac{W}{\left(\frac{k_BT}{q}\frac{2\epsilon}{qWN_D}\right)}$	2
Organic	$qa_O k_{rec} N_{HOMO} N_{LUMO}$ $(1-\eta_{PPd})exp\left(-\frac{\Delta E_{HL}}{k_BT}\right)$	$\eta_{PPd} J_x$	$\frac{k_{PPd}}{k_{PPd,eq}}$	$n_A = \frac{l_A}{\delta_D(l_A-1)+1}$
Hybrid	$q\langle a\rangle k_{rec} N_{HOMO} N_C$ $(1-\eta_{PPd})exp\left(-\frac{\Delta E_{OI}}{k_BT}\right)$	$\eta_d J_o + J_I$	$\frac{k_d}{k_{d,eq}}$	$n_O = \frac{l_O}{\delta_I(l_O-1)+1}$

Bibliography

[1] W. Shockley, "The theory of p-n junctions in semiconductors and p-n junction transistors," *Bell Syst. Tech. J.* **28**, 435 (1949).

[2] N. C. Giebink, G. P. Wiederrecht, M. R. Wasielewski, and S. R. Forrest, "Ideal diode equation for organic heterojunctions. I. Derivation and application," *Phys. Rev. B* **82**, 155305 (2010).

[3] C. K. Renshaw and S. R. Forrest, "Excited state and charge dynamics of hybrid organic/inorganic heterojunctions. I. Theory," *Phys. Rev. B* **90**, 045302 (2014).

[4] N. Li, K. Lee, C. K. Renshaw, X. Xiao, and S. R. Forrest, "Improved power conversion efficiency of InP solar cells using organic window layers," *Appl. Phys. Lett.* **98**, 053504 (2011).

[5] S. R. Forrest, M. L. Kaplan, and P. H. Schmidt, "Semiconductor analysis using organic-on-inorganic contact barriers. II. Application to InP-based compound semiconductors," *J. Appl. Phys.* **60**, 2406 (1986).

[6] S. R. Forrest, M. L. Kaplan, P. H. Schmidt, and J. V. Gates, "Evaluation of III-V semiconductor wafers using nondestructive organic-on-inorganic contact barriers," *J. Appl. Phys.* **57**, 2892 (1985).

[7] A. Panda, C. K. Renshaw, A. Oskooi, K. Lee, and S. R. Forrest, "Excited state and charge dynamics of hybrid organic/inorganic heterojunctions. II. Experiment," *Phys. Rev. B* **90**, 045303 (2014).

[8] V. M. Agranovich, D. M. Basko, G. C. L. Rocca, and F. Bassani, "Excitons and optical nonlinearities in hybrid organic inorganic nanostructures," *J. Phys.: Condens. Matter* **10**, 9369 (1998).

[9] S. Blumstengel, S. Sadofev, and F. Henneberger, "Electronic coupling of optical excitations in organic/inorganic semiconductor hybrid structures," *New J. Phys.* **10**, 065010 (2008).

[10] H. Bassler, "Charge transport in disordered organic photoconductors a Monte Carlo simulation study," *Phys. Stat. Sol. (b)* **175**, 15 (1993).

[11] P. Mark and W. Helfrich, "Space-charge-limited currents in organic crystals," *J. Appl. Phys.* **33**, 205 (1962).

[12] J. van de Lagemaat and A. J. Frank, "Effect of the surface-state distribution on electron transport in dye-sensitized TiO2 solar cells: nonlinear electron-transport kinetics," *J. Phys. Chem. B* **104**, 4292 (2000).

[13] S. Hirae, M. Hirose, and Y. Osaka, "Energy distribution of trapping states in polycrystalline silicon," *Journal of Applied Physics* **51**, 1043 (1980).

[14] B. Lussem, M. Riede, and K. Leo, "Doping of organic semiconductors," *Phys. Stat. Sol. (a)* **210**, 9 (2013).

[15] C. K. Renshaw, J. D. Zimmerman, B. E. Lassiter, and S. R. Forrest, "Photoconductivity in donor-acceptor heterojunction organic photovoltaics," *Phys. Rev. B* **86**, 085324 (2012).

[16] O. V. Mikhnenko, F. Cordella, A. B. Sieval, J. C. Hummelen, P. W. M. Blom, and M. A. Loi, "Temperature dependence of exciton diffusion in conjugated polymers," *J. Phys. Chem. B* **112**, 11601 (2008).

[17] T. M. Clarke and J. R. Durrant, "Charge photogeneration in organic solar cells," *Chem. Rev.* **110**, 6736 (2010).

[18] G. Grancini, M. Maiuri, D. Fazzi, A. Petrozza, et al., "Hot exciton dissociation in polymer solar cells," *Nat. Mater.* **12**, 29 (2012).

[19] W. Shockley and W. T. Read, "Statistics of the recombinations of holes and electrons," *Phys. Rev.* **87**, 835 (1952).

[20] C.-T. Sah, R. Noyce, and W. Shockley, "Carrier generation and recombination in p-n junctions and p-n junction characteristics," *Proc. IRE* **45**, 1228 (1957).

CHAPTER III

Theoretical description of hybrid charge transfer exciton

Analogous to the polaron-pair at excitonic HJs, the HCTE is a Coulombically bound charge-pair at OI-HJs. However, unlike the case of polaron-pairs where both charge species are localized, in the HCTE the charge in the inorganic is delocalized over many lattice sites, unless confined, while the polaron in the organic is localized on a particular molecule. As the discussion in Chapter II indicates, the HCTE is the quasi-particle that mediates exciton to charge conversion and charge recombination at the OI-HJ. Its formation, recombination, and dissociation rates play a crucial role in governing the behavior of OI-HJ diodes which are determined by the fundamental optoelectronic properties of the state. In this chapter we discuss both a semi-classical but analytical description of the state and a fully quantum mechanical simulation. The models are then used to predict the optoelectronic properties of interest for the experimental work presented in this thesis. Models for HCTE kinetics are also discussed. The chapter is organized as follows: first, an analytical expression for the HCTE binding energy is discussed based on the Bohr model. Second, a first principles quantum mechanical simulation is presented. Third, simulation results of HCTE properties as a function of the inorganic semiconductor dimensionality are presented. Fourth, the effect of the transition dipole moment orientation on HCTE emission is discussed. Finally, models for HCTE formation, dissociation and recombination are discussed.

3.1 Bohr model of the HCTE

The HCTE can be thought of as a hybrid between a Frenkel and WM exciton, as shown in Fig. 3.1. However, due to the high dielectric constant and delocalized nature of the carriers in the inorganic, the HCTE E_B, is expected to be much smaller than k_BT at RT, making the state unstable or at best metastable (i.e. characterized by a ps lifetime at RT). The HCTE is visualized in Fig. 3.1 as a localized polaron (hole) ($\approx$ 1 nm) on the organic side and an electron delocalized ($\approx$ 6 nm) on the inorganic side over many lattice sites. Once formed, the HCTE can either dissociate by thermal excitation or field at the OI-HJ (F_{OI-HJ}), or relax by recombining radiatively or non-radiatively. The dynamical properties of the HCTE are also strongly dependent on whether the transfer is between energetically resonant or non-resonant states at the two sides of the interface [1]. To estimate the E_B and $\langle a \rangle$ of the HCTE, it is helpful to look at a semi-classical picture of the state.

To estimate the E_B, we begin by defining $\langle \epsilon_R \rangle = (r_I\epsilon_I + r_O\epsilon_O)/(\epsilon_I + \epsilon_O)$, the effective dielectric constant, where r_I and r_O is the extent of the HCTE into the inorganic and organic layers, respectively. We estimate r following Onsager theory as $r = q^2/(4\pi\epsilon k_BT)$ [3]. We use the Bohr model [4] to estimate, $\langle a \rangle$, the diameter of the HCTE:

$$\langle a \rangle = a_I + a_O = \frac{4\pi\langle \epsilon_r \rangle \epsilon_0 \hbar^2}{m^* q^2} \tag{3.1}$$

where $m^* = (1/m_{e,I} + 1/m_{h,O})^{-1}$. Note that m^* generally reduces to $m_{e,I}$ since it is much lower as compared to $m_{h,O}$. The binding energy is then:

$$E_b = \frac{q^2}{4\pi\langle a \rangle \langle \epsilon_r \rangle}. \tag{3.2}$$

Figure 3.2 shows the HCTE E_B and $\langle a \rangle$ as a function of the $\langle \epsilon_R \rangle$ for $m^* = 1m_0$, $0.2m_0$ and $0.05m_0$. We find that in most cases the HCTE is expected to be unstable (i.e.

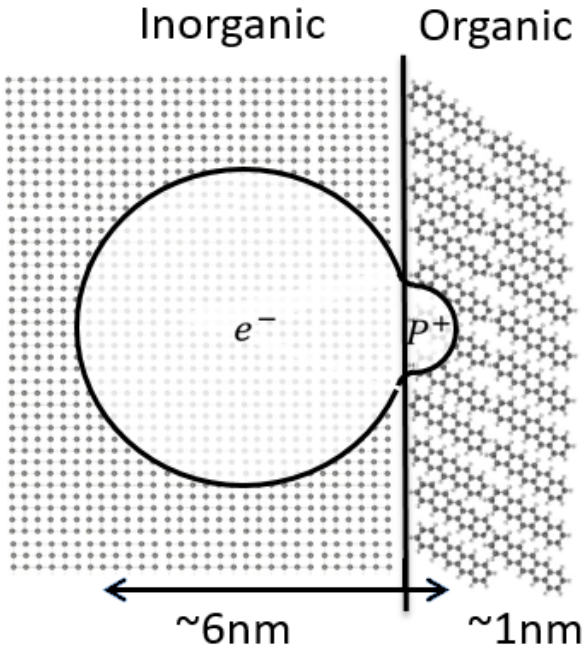

Figure 3.1: Conceptual illustration of the HCTE state. The electron in the inorganic is delocalized over a large number of lattice sites due to its relatively large dielectric constant, analogous to a WM state. This electron is Coloumbically bound to a positive polaron (hole) in the organic that is localized on one or two molecules at the interface, analogous to a Frenkel state. The arrows at the bottom note typical extent of these states into the respective materials. Figure adapted from Ref. [2].

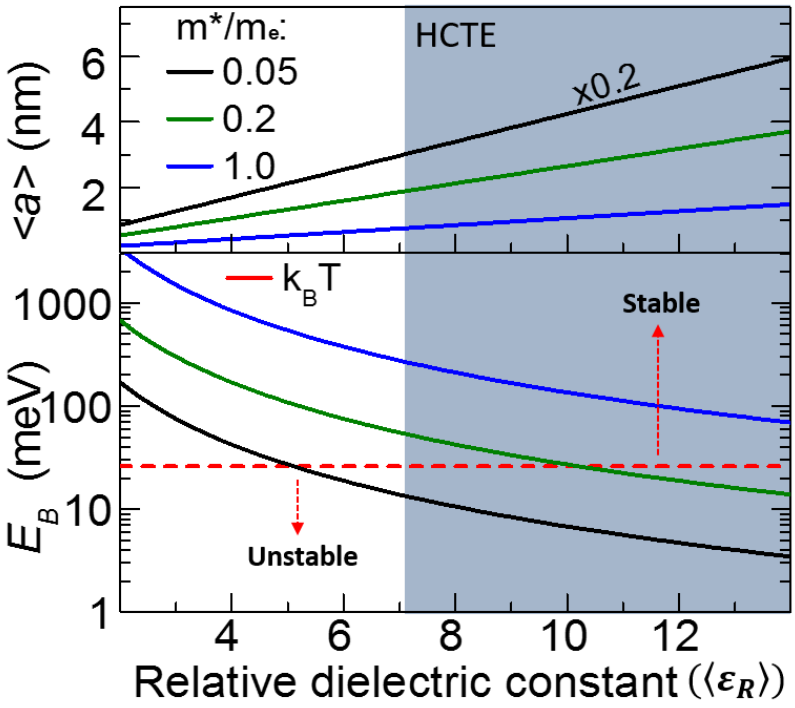

Figure 3.2: E_B and characteristic diameter, $\langle a \rangle$, of the HCTE as a function of the relative dielectric constant, $\langle \epsilon_R \rangle$ and m^*. The $\langle \epsilon_R \rangle$ and m^* are approximated well by the parameters of the inorganic, ϵ_I and $m_{e,I}$. The dashed line indicates the thermal energy at RT that demarks the regions of HCTE stability ($E_B > k_B T$) and instability ($E_B < k_B T$). The shaded region indicates the region with dielectric constants for most OI systems. Figure adapted from Ref. [2].

$E_B < k_B T$), unless the $\langle \epsilon \rangle$ is low or the m^* is high, and the $\langle a \rangle$ is $\approx 5-20$ nm. This model assumes that the electronic states are extended and that a localized electron is formed by a wavepacket whose motion can be characterized by the effective mass. The direct extension of the concept of m_0 to organic semiconductors is not rigorous; however, it has been estimated to be much higher than the $m_{e,I}$ [5, 6]. Therefore, this semi-classical approach is not expected to be accurate for large effective masses and highly localized charges and a rigorous calculation of E_B and $\langle a \rangle$ requires a fully quantum mechanical approach.

3.2 Quantum mechanical model of the HCTE

As discussed in §3.1, the delocalization of the electron in the HCTE is estimated to be about 6 nm. As a result, a fully quantum mechanical time-dependent DFT calculation of the state needs to include over 24,000 atoms, which is computationally prohibitive. We simplify the problem by developing a quantum mechanical description of the HCTE that consists of solving a one-body time-independent Schrödinger equation for the electron bound to a fixed hole (i.e. $m_{h,O} \rightarrow \infty$) across the OI-HJ. This assumption is justified by the comparatively lower dielectric constant, and larger effective mass of the hole, in the organic. This method yields the approximate electron and hole wave functions but results in the loss of their relative phase information, making the subsequent calculation of oscillator strength (f) and radiative lifetime (τ_r) only qualitatively valuable. Accurate calculations of the radiative lifetime require time-dependent DFT calculations.

The workflow for the simulation is summarized in Fig. 3.3. We combine molecular dynamics (MD) simulations of the organic on the inorganic surface, DFT calculations of the organic molecular orbitals, and solution to the Schrödinger equation to describe charges bound at the OI-HJ [7, 8]. The MD simulations are done using Materials Studio® and yield the average distance of the organic when deposited on the inorganic surface. The organic molecule is assumed to lay flat for subsequent calculations since this gives

the largest oscillator strength of the HCTE and thus accounts for most of the emission. In an amorphous film, multiple orientations of the molecule are expected, which would further reduce the estimated binding energy and oscillator strength of the state. The spatial charge distribution of the cationic organic molecule (hole) is found with DFT calculations using Gaussian 09®. The functional and basis set used for DFT calculations contained in this thesis are discussed in §1.5.3. The time-independent Schrödinger equation is solved using COMSOL Multiphysics® using the Hamiltonian:

$$\hat{H} = \frac{\hbar^2}{2m^*(z)}\nabla^2 - \sum_{i=1}^{n} \frac{\alpha(z)q^2/n}{4\pi\epsilon_R(z)\epsilon_0|\mathbf{r_e} - \mathbf{r_i}|} - \frac{\beta(z)q^2}{16\pi\epsilon_R(z)\epsilon_0 z} + \Delta E_{cL}, \tag{3.3}$$

where z is the direction perpendicular to the interface and $\mathbf{r_e}$ is the position of the electron. Here we have replaced the hole distribution on the HOMO of the organic with a summation over n discrete, fractional point charges at positions $\mathbf{r_i}$. The screening factor for the hole is $\alpha(z) = 2\epsilon_I/(\epsilon_O + \epsilon_O)$ in the inorganic and $\alpha(z) = 1$ in the organic, and $\beta(z)$ is the image charge factor with $\beta(z) = \pm(\epsilon_I - \epsilon_O)/(\epsilon_I + \epsilon_O)$ where the plus sign is for the organic, and the minus is for the inorganic. The first term in Eq. 3.3 is the kinetic energy of the electron, the second is the Coulomb energy due to the hole screened by the polarization of the organic, and the third term is the image potential energy from the induced charge at the interface.

3.3 HCTE in reduced dimensional systems

The quantum mechanical description of the HCTE can be used to accurately predict the properties of the state in any OI semiconductor material system, given that the energy level offsets at the OI-HJ, the dielectric constants, and the charge carrier effective masses in the respective materials are known. In Fig. 3.4, we show the three states observed in the experimental work contained in this thesis: the free HCTE ($HCTE_F$), the QW-confined HCTE ($HCTE_{QW}$) and the trapped HCTE ($HCTE_T$). In the three states

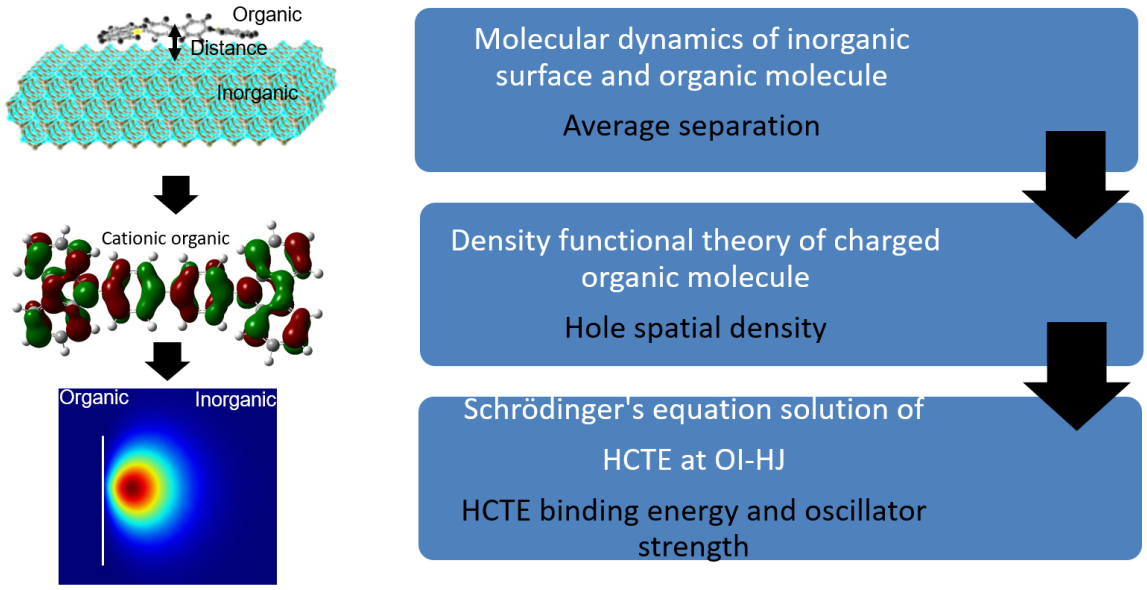

Figure 3.3: Steps for calculating HCTE properties from first principles. First, MD simulations of the organic molecule on the inorganic surface are done to determine the average separation between them. Second, DFT calculation of the organic with an electron removed from its HOMO (cationic molecule) is done to determine the spatial charge distribution of the polaron (hole). Finally, the time-independent Schrödinger equation is solved in the OI systems using the Hamiltonian in Eq. 3.3 to determine the E_B and electron charge distribution. The electron and hole charge distributions are then used to compute the oscillator strength and to estimate the radiative lifetime of the HCTE.

the available dimensions for electron delocalization is reduced from 3D to 2D to 0D (Fig. 1.6). To simulate the properties of the $HCTE_{QW}$, a thin ($\sim 2-5$ nm) inorganic layer with a lower band gap is inserted at the heterointerface and the resulting image charges in the various layers are taken into account. For the $HCTE_T$, an additional Coulomb potential, $V_{trap} = -Sq^2/(4\pi\epsilon_I\epsilon_0|\mathbf{r_e}-\mathbf{r_{trap}}|)$ is added to Eq. 3.3 which represents the location of the trapped electron. Here, r_{trap} is the position of the trap and S is the screening factor that determines its depth and the spatial extent of electron delocalization in the trap. The resulting range of properties of the three states are listed in Table 3.1. Generally, the E_B and the radiative lifetime of the state increases with increasing electron confinement. The E_B is given with respect to the quantized free electron energy level in the confined system. In the $HCTE_{QW}$ case it is EE_1, the first quantized electron level in the QW, and in the $HCTE_T$ case it is $E_{F,n}$ which determines the occupied energy levels of the traps.

In the 2D case, the maximum improvement in binding energy is given as [9]:

$$E_B^{QW} = 4\left(\frac{\epsilon_W}{\epsilon_B}\right)E_B^{Free} \tag{3.4}$$

where E_B^{Free} is the binding energy of exciton in the bulk, and ϵ_W and ϵ_B are the dielectric constants of the QW and the barrier layer. In the 0D case, the binding energy is given using Eq. 3.1, where the $\langle a \rangle$ is now simply the size of electron delocalization. While an infinitely high binding energy is theoretically possible due to the inverse relationship between $\langle a \rangle$ and E_B, in practice the maximum limit specified by Eq. 3.4 is rarely exceeded due to an inability to keep the electron wave function confined to a small radius.

3.4 Emission pattern of the HCTE

As shown in Fig. 3.4, the HCTE electron probability density is oriented parallel to the interface, resulting in a preferential orientation of the transition dipole moment of

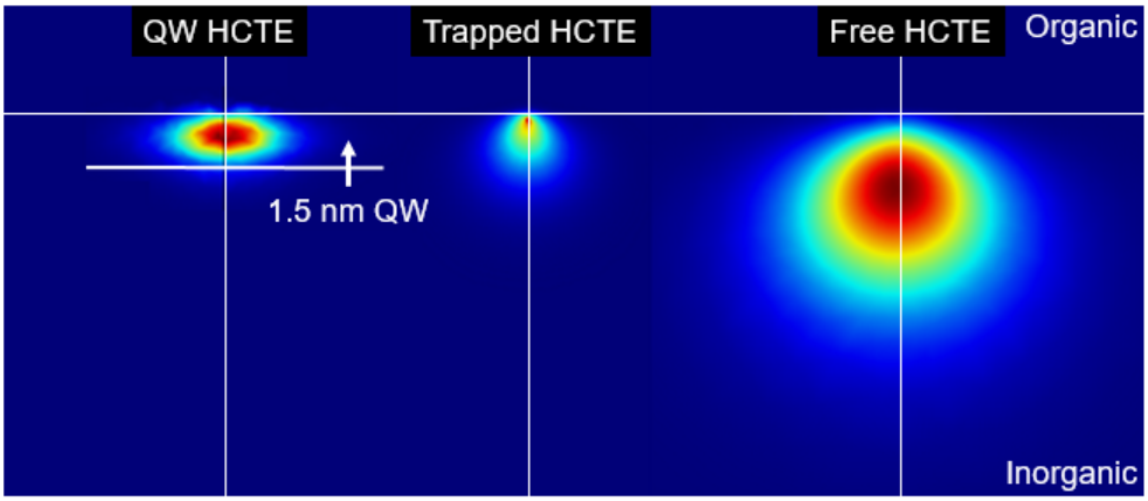

Figure 3.4: Spatial probability density of the electron for the lowest eigenvalue solution of the HCTE predicted in 3D (free), 2D (QW) and 0D (trapped) electron systems. Experimental data supporting the existence of these states is contained in Chapter IV. The optoelectronic properties of these states are summarized in Table 3.1.

Table 3.1: Predicted E_B and radiative lifetime (τ_r) of the HCTE states where the electron is delocalized in 3D (free), 2D (QW) and 0D (trapped). The representative electron wave function delocalization for the states are shown in Fig. 3.4. Reducing the dimensionality of the electron in the inorganic semiconductor results in increase in the binding energy and radiative lifetime of the state. The variables for predicted emission peaks are defined in Fig. 4.10 and Fig. 4.17.

HCTE type	**Predicted emission energy**	**Binding energy (meV)**	**Radiative lifetime (s)**
Free HCTE (3D)	$\Delta E_{OI} - E_B$	10-2	$\approx 10^{-3}$
QW HCTE (2D)	$\Delta E_{OI} - E_B + \Delta E_C + EE_1$	200-50	$\approx 10^{-6}$
Trapped HCTE (0D)	$\Delta E_{OI} - E_B - E_{F,n}$	450-50	$\approx 10^{-9}$

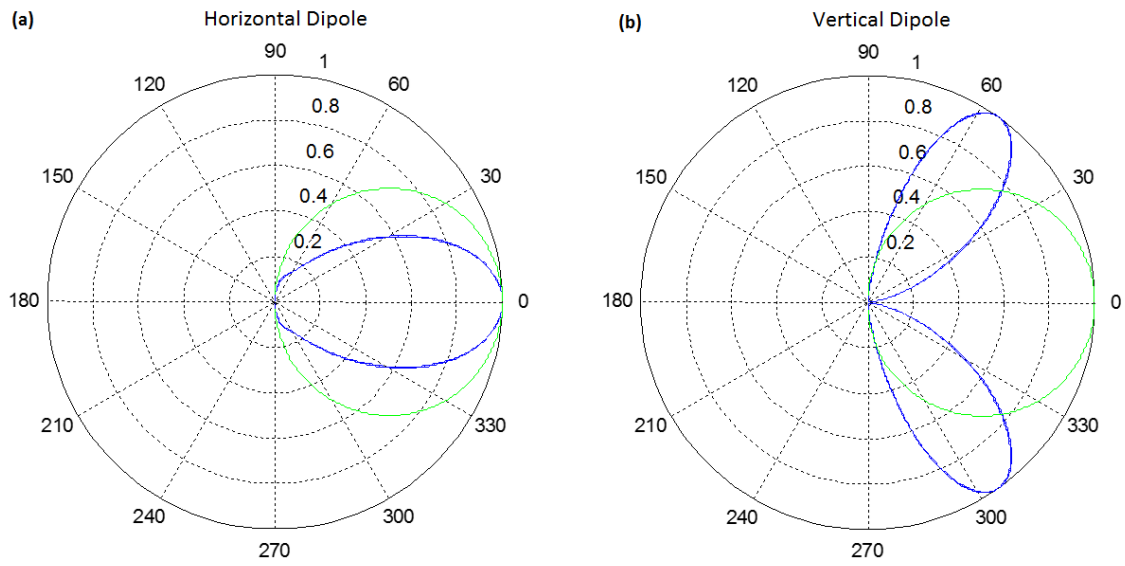

Figure 3.5: Predicted HCTE emission pattern for a HCTE with a (a) vertically and (b) horizontally oriented transition dipole moment when the emission is observed from the organic side of the sample. Maximum emission power for an HCTE with a vertically oriented transition dipole moment is at $\sim 55°$ from the normal and at the normal for a state with a horizontal transition dipole moment. An HCTE with a vertical transition dipole moment has an outcoupling efficiency of 2%, while the horizontal one has a 12% outcoupling efficiency. The simulation results are courtesy of Yue Qu, and follows the procedure is outlined in Ref. [10].

the state. The horizontal orientation factor is then defined as $\theta_{hor} = \frac{f_x+f_y}{f_x+f_y+f_z}$. Vertical orientation factor $\theta_{ver} = \frac{f_z}{f_x+f_y+f_z}$, f is the oscillator strength of the state in a given direction, as defined in Eq. 1.34. Assuming planar OI-HJs, the free HCTE is estimated to have $\theta_{ver} = 0.4$ and $\theta_{hor} = 0.5$. For the QW HCTE the estimated $\theta_{ver} = 0.45$ and $\theta_{hor} = 0.55$. For a trapped HCTE, the estimated $\theta_{ver} = 0.33$ and $\theta_{hor} = 0.66$.

We also estimate the outcoupling efficiency (η_{OUT}) and emission angle for the HCTE at the OI-HJ in the sample sapphire/inorganic (1 μm)/organic (5 nm), where the emission is observed from the organic side of the sample. For a state with a vertical transition dipole moment, $\eta_{OUT} = 2\%$, while for the horizontal case, $\eta_{OUT} = 12\%$. The low outcoupling efficiency is a result of the high n_r of the inorganic, and can be enhanced further by roughening the smooth interfaces. The angular dependence of the emission power

from the two transition dipole moments are shown in Fig. 3.5. The average emission angle or outcoupling efficiency is given by weighing the values for each orientation by the θ_{ver} and θ_{hor} of the state.

3.5 Rate of formation, recombination and dissociation of the HCTE

The rates of HCTE recombination, formation, and dissociation and their dependence on temperature and field are of critical importance for device operation, as discussed in §2.1, and for ensuring optical signatures of the HCTE are observed. The rate of HCTE formation (k_{rec}) when limited by low mobility charge carriers in the organic is estimated using Langevin recombination given in Eq. 1.18. This process is thermally activated due to the temperature dependence of charge carrier mobility in the organic. When limited by high mobility electrons, the rate is given as $k_{rec} = \nu_{th}\sigma$ where the thermal velocity $\nu_{th} = \sqrt{3k_BT/m_{eI}}$ and σ is the trap capture cross-section.

The HCTE formation rate (via electron transfer) from the organic exciton precursor is described using Marcus theory [11]:

$$k_{et} = k_{et,0} exp\left(\frac{-(\chi_{org} - \Delta E_{cL})^2}{4\chi_{org}k_BT}\right). \tag{3.5}$$

Here $k_{et,0}$ is the transfer rate at infinite temperature and zero field and χ_{org} is the molecular reorganization energy. For $E_{cL} < \sigma$, the rate of electron transfer decreases with decreasing E_{cL}. This process is usually efficient and occurs on a ns time scale. For $E_{cL} > \sigma$, the rate decreases with increasing E_{cL}. This regime is known as the inverted regime and is rarely observed for the exciton dissociation process. Equation 3.5 can also be useful for describing the HCTE recombination rate (k_r), which generally occurs in the inverted regime. Further modifications to Marcus theory have been developed to account for enhancement in the recombination rate through non-adiabatic, phonon-mediated processes [12]. If the HCTE relaxation to the ground state occurs via a radiative process,

the rate can be estimated using Eq. 1.33. In this case, $\omega = \Delta E_{OI}/\hbar$, ψ_1 is the electron wave function of the HCTE obtained from solving the Schrödinger equation in step three of the procedure outlined in Fig. 3.3, and ψ_2 is the hole wave function in a cationic organic molecule obtained from DFT in step two. We use the CBP cationic wave function since the optical transition occurs faster than molecular relaxation (the Franck-Condon principle, see Fig. 1.15).

Using the Onsager-Braun (OB) model, the dissociation of the HCTE is written as [3, 13]:

$$k_d^{OB} = A_{OB} exp\left(\frac{qE_B}{k_B T}\right) \frac{J_1[2\sqrt{(-2b)}]}{\sqrt{(-2b)}}. \tag{3.6}$$

Here, $b = q^3 F_{OI-HJ}/8\pi\epsilon k_B^2 T^2$, J_1 is the first-order Bessel function, A_{OB} is the HCTE volume as defined in §2.1 with the radius defined in Eq. 3.1. This model is valid for low mobility semiconductors where the mean free path of the charge carrier is less than the capture radius. In the case of a mobile carrier, the field dependence is larger and k_d is given by a expression similar to the Poole-Frenkel emission:

$$k_d^{FP} = k_{d,0} exp\left(\frac{-qE_B}{k_B T}\right) exp(\beta F^{1/2}), \tag{3.7}$$

where $k_{d,0}$ is the dissociation rate at infinite temperature and zero field and $\beta = (q^3/\pi\epsilon)^{1/2}/k_B T$.

Bibliography

[1] V. M. Agranovich, Y. N. Gartstein, and M. Litinskaya, "Hybrid resonant organic-inorganic nanostructures for optoelectronic applications," *Chem. Rev.* **111**, 5179 (2011).

[2] C. K. Renshaw and S. R. Forrest, "Excited state and charge dynamics of hybrid organic/inorganic heterojunctions. I. Theory," *Phys. Rev. B* **90**, 045302 (2014).

[3] L. Onsager, "Deviations from Ohm's law in weak electrolytes," *J. Chem. Phys.* **2**, 599 (1934).

[4] N. W. Ashcroft and N. D. Mermin, *Solid state physics*, 1st ed. (Holt, Rinehart and Winston, New York, USA, 1976).

[5] F. F. So and S. R. Forrest, "Evidence for exciton confinement in crystalline organic multiple quantum wells," *Phys. Rev. Lett.* **66**, 2649 (1991).

[6] R. J. Fleming, "Upper limit of electron effective mass in organic semiconductors," *J. Chem. Phys.* **56**, 4911 (1972).

[7] X.-Y. Zhu, Q. Yang, and M. Muntwiler, "Charge-transfer excitons at organic semiconductor surfaces and interfaces," *Acc. Chem. Res.* **42**, 1779 (2009).

[8] Q. Yang, M. Muntwiler, and X.-Y. Zhu, "Charge transfer excitons and image potential states on organic semiconductor surfaces," *Phys. Rev. B* **80**, 115214 (2009).

[9] H. Takagi, H. Kunugita, and K. Ema, "Influence of the image charge effect on excitonic energy structure in organic-inorganic multiple quantum well crystals," *Phys. Rev. B* **87**, 125421 (2013).

[10] K. Celebi, T. D. Heidel, and M. A. Baldo, "Simplified calculation of dipole energy transport in a multilayer stack using dyadic greens functions," *Opt. Express* **15**, 1762 (2007).

[11] R. A. Marcus and N. Sutin, "Electron transfers in chemistry and biology," *Biochim. Biophys. Act. - Reviews on Bioenergetics* **811**, 265 (1985).

[12] G. L. Closs, L. T. Calcaterra, N. J. Green, K. W. Penfield, and J. R. Miller, "Distance, stereoelectronic effects, and the Marcus inverted region in intramolecular electron transfer in organic radical anions," *J. Phys. Chem.* **90**, 3673 (1986).

[13] C. L. Braun, "Electric field assisted dissociation of charge transfer states as a mechanism of photocarrier production," *J. Chem. Phys.* **80**, 4157 (1984).

CHAPTER IV

Experimental investigation of organic-inorganic heterojunction based diodes

In this chapter we apply the $J-V$ theory outlined in Chapter II and the understanding of the HCTE state developed in Chapter III to analyze the electro-optical characteristics of four archetype OI-HJ based diode systems. The first system is based on the TiO_2/tetraphenyldibenzoperiflanthene (DBP) junction, which is chosen because of the widespread use of TiO_2 as an acceptor in DSSCs. The second system is based on an InP/pentacene (PEN) junction, which is chosen because InP can be epitaxially grown, allowing for systematic control of the HCTE by HJ engineering. The characteristics of these two systems are analyzed together to highlight the difference in behavior for OI-HJs with wide and moderate bad gap inorganic semiconductors. The third is based on a ZnO/4,4'-bis(N-carbazolyl)-1,1'-biphenyl (CBP) junction chosen for the relatively low dielectric constant of ZnO, allowing for optical observation of the HCTE at higher than cryogenic temperatures. The fourth is based on a GaN/(In)GaN/DBP or CBP junction, where the nitride semiconductor material system is chosen for both its relatively low dielectric constant and because it can be grown epitaxially, allowing for both observation of the HCTE at RT and manipulaation its optoelectronic properties by systematically tuning the OI-HJ.

Each subsection is organized as follows: first, an introduction to the material system is provided along with review of past work. Second, modifications to the theory from the previous chapter are applied to the specific semiconductor system studied. Third,

the experimental details and results are provided. Finally, the results are discussed in the context of the theory to glean broader implications for the physics of HCTE OI-HJs.

4.1 TiO_2/DBP and InP/PEN OI-HJs

The wide band gap TiO_2/DBP acceptor junction employs TiO_2 that has found widespread use in OI DSSCs [1, 2] and has been recently explored in metal oxide/polymer HJ solar cells [3, 4]. Furthermore, Frenkel/WM exciton hybridization has been found in the closely related metal oxide semiconductor/organic system consisting of ZnO and 1,4,5,8-naphthalenetetracarboxylic dianhydride (NTCDA) in strongly coupled optical cavities [5]. The second system studied here is the moderate band gap InP/PEN junction. Among other applications, InP has been shown to form rectifying OI-HJs [6, 7] that result in an improved photovoltaic power conversion efficiency compared to cells lacking an organic window layer [8].

We quantitatively analyze both the EQE and $J-V$ characteristics of archetype OI-HJs as functions of T, which provide insight into the nature of the HCTE and the role of surface states in determining the diode properties. The analysis provides convincing evidence for the existence of an HCTE in both the TiO_2 and InP-based systems. We find that the HCTE at the InP/PEN junction is strongly affected by traps at high temperatures. At low temperatures, the trap effects are "frozen out," resulting in a significant reduction in exciton quenching at the OI-HJ. In contrast, traps play a reduced role at the TiO_2/DBP junction. Fits to the $J-V$ characteristics under both illumination and in the dark show the relative importance of charge injection over the OI-HJ barrier vs. interface recombination in the two systems. Since the excited state and charge recombination kinetics are significantly different for the wide and moderate band gap semiconductor systems, whenever necessary, separate sub-sections treat these two cases for clarity. Further, by comparing the EQE and $J-V$ data from these two cases, we test the validity and generality of the theory presented in Chapter II.

4.1.1 Theory

A rigorous treatment of exciton and charge dynamics at the OI-HJ requires simultaneous solution to the coupled drift-diffusion and Poisson equations for both the inorganic and organic layers, as discussed in §2.3. To simplify this analysis, we begin by recognizing the large asymmetry in the charge mobility of the inorganic semiconductor as compared to that of the organic semiconductor, such that we can assume that the $E_{F,n}$ is flat throughout the inorganic layer. Further, we assume the $E_{F,P}$ in the organic at high current densities is determined by the SCL current regime (see Eq. 2.12).

Wide band gap semiconductor junction

To express the dependence of current density on V_a for the wide band gap diode, we assume an exponential density of trap states in both the organic and inorganic semiconductors, drift-limited transport through the organic at high current. For the HCTE we assume a small E_B and effective coupling to the ground state. This is reasonable because of the high dielectric constant of TiO_2 and the high density of defects at the surface. Furthermore, by assuming the current is determined by free carrier recombination with trapped carriers, we can write (see Eq. 2.6):

$$\begin{aligned} J = q\langle a\rangle\Bigg[& k_{rec,n}N_c H_o exp\left(-\frac{\alpha_O}{k_B T}\right)\left(exp\left(\frac{qV_a - \Delta E_{F,P}}{n_O k_b T}\right) - 1\right) \\ & + k_{rec,p}N_{HOMO}H_I exp\left(-\frac{\alpha_I}{k_b T}\right)\left(exp\left(\frac{qV_a - \Delta E_{F,P}}{n_I k_b T}\right) - 1\right)\Bigg] - qJ_X + J_I. \end{aligned} \tag{4.1}$$

Given the large band gap energy of TiO_2 (3.3 eV) [1], we can illuminate the TiO_2/DBP diode at energies where only the DBP absorbs (3.3 −1.8 eV), thereby generating excitons only in the organic. Under these conditions $J_I = 0$. The ideality factors (n_O and n_I) and energies (α_O and α_O) are defined in Eq. 2.7. Along with $\Delta E_{F,P}$, these variables are functions of δ_O and δ_I. The uniform field approximation is used to determine δ_O and δ_I.

For simplicity, Eq. 4.1 is then rewritten as:

$$\begin{aligned} J = J_{s1} exp\left(-\frac{\alpha_O}{k_B T}\right)\left(exp\left(\frac{qV_a - \Delta E_{F,P}}{n_O k_b T}\right) - 1\right) \\ + J_{s2} exp\left(-\frac{\alpha_I}{k_b T}\right)\left(exp\left(\frac{qV_a - \Delta E_{F,P}}{n_I k_b T}\right) - 1\right) - qJ_X. \end{aligned} \tag{4.2}$$

Here, J_{s1} and J_{s2} are functions of k_{rec}, which can be temperature and light intensity dependent.

Moderate band gap semiconductor junction

The $J-V$ characteristics for the moderate band gap inorganic semiconductor diode are obtained by assuming a discrete trap state (at energy E_t from the E_c) at the inorganic surface. Due to the smaller energy level offsets at the OI-HJ expected in cases where the organic and inorganic energy gaps are comparable, thermionic emission over the interface barrier can also be significant. Assuming the current is determined by both trapped electron to free hole recombination and thermionic emission over the OI-HJ barrier (see Eq. 2.13), we can write:

$$\begin{aligned} J = q\langle a\rangle k_{rec,p} N_{HOMO} H_I exp\left(-\frac{E_t}{k_B T}\right)\left(exp\left(\frac{qV_a - \Delta E_{F,P}}{n_I k_B T}\right) - 1\right) \\ + \upsilon q a_O P_c exp\left(-\frac{\Delta E_V}{k_B T}\right) exp\left(\frac{qV_a}{n_{therm} k_B T}\right) - qJ_X + J_I. \end{aligned} \tag{4.3}$$

Here, n_{therm} is the ideality factor for thermionic emission that depends on the existence of interface traps and n_I is the ideality for interface recombination with trap states in the inorganic. In writing the first exponential of Eq. 4.3, we have ignored carrier recombination in the bulk of the InP. This is reasonable for photogenerated and injected carriers when thermionic emission is absent (i.e. reverse bias and low forward bias) since InP has a minority carrier diffusion length (typically > 5 μm [9]) greater than the thickness used in the device (1 μm). Further, we have assumed that when thermionic emission over the barrier is present, diffusion current dominates over drift at small

forward bias. The $\Delta E_{F,P}$ are a function of δ_O and δ_I, which, in turn, are functions of the applied voltage because the InP layer is not fully depleted. At equilibrium, δ_O and δ_I can be determined as outlined in §2.2.

Simplifying Eq. 4.3, we thus obtain:

$$\begin{aligned} J = J_{s1} exp\left(-\frac{E_t}{k_B T}\right)\left(exp\left(\frac{qV_a - \Delta E_{F,P}}{n_I k_B T}\right) - 1\right) \\ + J_{s2} exp\left(-\frac{\Delta E_V}{k_B T}\right) exp\left(\frac{qV_a - R_s J}{n_{therm} k_B T}\right) - qJ_X + J_I. \end{aligned} \tag{4.4}$$

Here, we have included R_S to account for contact resistance limited current at high currents.

4.1.2 Experimental methods

The thin film TiO_2/DBP devices are grown on solvent-cleaned, 150 nm thick film of indium tin oxide (ITO) patterned into 1 mm wide stripes on a glass substrate (Luminescence Technology Corp.). For cleaning the substrate is sequentially sonicated in detergent, deionized water, acetone and isopropanol [10]. The device structure is ITO (150 nm)/TiO_2 (60 nm)/DBP (30 nm)/MoO_3 (15 nm)/Al (100 nm) as shown in the inset of Fig. 4.1. We include the MoO_3 as a hole transport layer that also protects the DBP from damage during metal deposition, and is further capped with an Al cathode to form an Ohmic contact with the organic semiconductor [11].

The TiO_2 film is grown by sputtering from a Ti target at 6 sccm of O_2 flow while maintaining the chamber pressure at 5.5 mTorr. This O_2 flow rate is at the threshold of complete target oxidization determined by the increase in sputtering voltage at a DC power of 300 W [13, 14]. The substrate is heated to 300° C during deposition at a rate of 0.33 Å/s to promote the formation of a dense and conductive TiO_2 film. The resulting film is determined to be nearly stoichiometric by X-ray photoelectron spectroscopy (XPS). Next, we sequentially deposit DBP (Luminescence Technology Corp.), MoO_3 (Alfa Aesar)

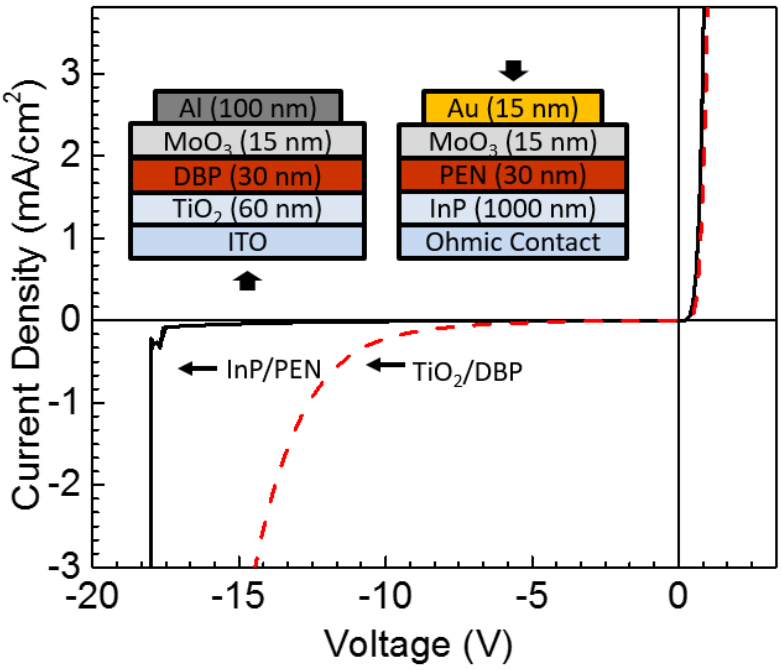

Figure 4.1: $J-V$ characteristics showing the breakdown of a TiO_2/DBP diode (dashed line) and an InP/PEN diode (solid line) at -14 V and -18 V, respectively. The device structures are shown in the inset, where the arrows indicate illumination direction. Figure reproduced from Ref. [12].

and Al by VTE at 1 Å/s in a chamber with a base pressure of 1x10^{-7} Torr. Prior to growth, all organics were purified once by vacuum thermal-gradient sublimation (see Fig. 1.9). The Al cathode is deposited perpendicular to the ITO stripes through a shadow mask with 1 mm wide openings to define a 1 mm^2 device area.

Fabrication of the InP/PEN device starts with the growth of a 1000 nm thick, nominally undoped (1x10^{16} cm^{-3}) InP layer by MBE on a S-doped (1x10^{18} cm^{-3}) (100) InP wafer (WaferTech LLC). The device structure is InP/PEN (30 nm)/MoO_3 (10 nm)/Au (15 nm), as shown in the inset of Fig. 4.1. Post-growth, the wafer is transferred to an e-beam chamber with base pressure of 1x10^{-8} Torr, where an Ohmic contact (Pd (5 nm)/Ge (50 nm)/Au (65 nm)/Ti (20 nm)/Au (50 nm)) [15] is deposited on the non-epitaxial growth side, followed by annealing in air at 180° C for 25 min. Prior to organic deposition the wafer is cleaved into (1.5 cm)^2 substrates and the native oxide is removed by brief immersion in buffered HF, followed by immediate transfer of the substrate into a glovebox filled with ultrahigh purity ($<$ 1 ppm O_2) N_2. There, the substrate is attached to a Au-coated Si wafer using In to allow access to the cathode. Next, PEN (Sigma Aldrich) and MoO_3 are deposited by VTE at $1-2$ Å/s chamber with a base pressure of 1x10^{-6} Torr. The circular device area of 1 mm radius is defined by a Au cathode deposited through a shadow mask by e-beam evaporation. A significant variation in the $J-V$ and EQE characteristics of devices on a single substrate were observed, possibly due to irregular PEN surface morphology resulting from local crystallization commonly observed for this material [16]. For measurements, therefore, we select the devices with the most revealing EQE characteristics vs. T.

For temperature dependent measurements, the devices are loaded into an open-cycle liquid N_2 cryostat. The $J-V$ characteristics are obtained in the dark and under illumination using a semiconductor parameter analyzer. The light intensity is calibrated using a National Renewable Energy Laboratory-traceable Si reference cell. The EQE measurements are obtained with a monochromated (spectral resolution of $\approx$ 10 nm)

halogen lamp chopped at 200 Hz and a lock-in amplifier. A National Institutes of Standards and Technologies traceable Si photodetector is used to calibrate the beam intensity at each wavelength. During measurement, the cryostat is maintained at $< 1x10^{-3}$ Torr to prevent degradation by exposure to oxygen or moisture.

The samples are cooled to 134 K and allowed to equilibrate for an hour. The measurements are then taken at 20 K steps using a thermally controlled stage heater at 20 min intervals to allow for thermal stabilization. To minimize trapping-induced hysteresis in the $J-V$ characteristics apparent at low temperatures, the devices are first maintained at 0 V for 5 s before voltage sweeps in both forward and reverse directions. The $J-V$ characteristics under illumination are taken under a power of 100 mW/cm^2 (1 Sun) for the TiO_2-based sample, and 25 mW/cm^2 for the InP-based sample. The TiO_2 sample is illuminated at $\lambda = 633$ nm via emission from a He-Ne laser, while the InP sample is illuminated by a AM 1.5G solar simulator. The power for the AM 1.5 G solar simulator is determined using a National Renewable Energy Laboratory calibrated reference cell. Fits to the data are done using MATLAB® using a non-linear least-squares, trust-region algorithm.

UPS measurements are done in an ultrahigh vacuum chamber base pressure $< 1x10^{-9}$ Torr using He-I emission (see §1.5.3). The substrates are prepared similarly to those used for device fabrication, and transferred into the system through a N_2-filled glove box where the organic deposition is done in an organic molecular beam deposition (OMBD) system ($\approx 1x10^{-8}$ Torr) interconnected with the measurement chamber. The spectra are collected using a hemispherical electron energy analyzer (Thermo VG) with a pass function FWHM of 0.16 eV.

4.1.3 Results

Figure 4.1 shows representative room temperature $J-V$ characteristics of both OI-HJ diodes. They exhibit pronounced rectification with an exponential increase in

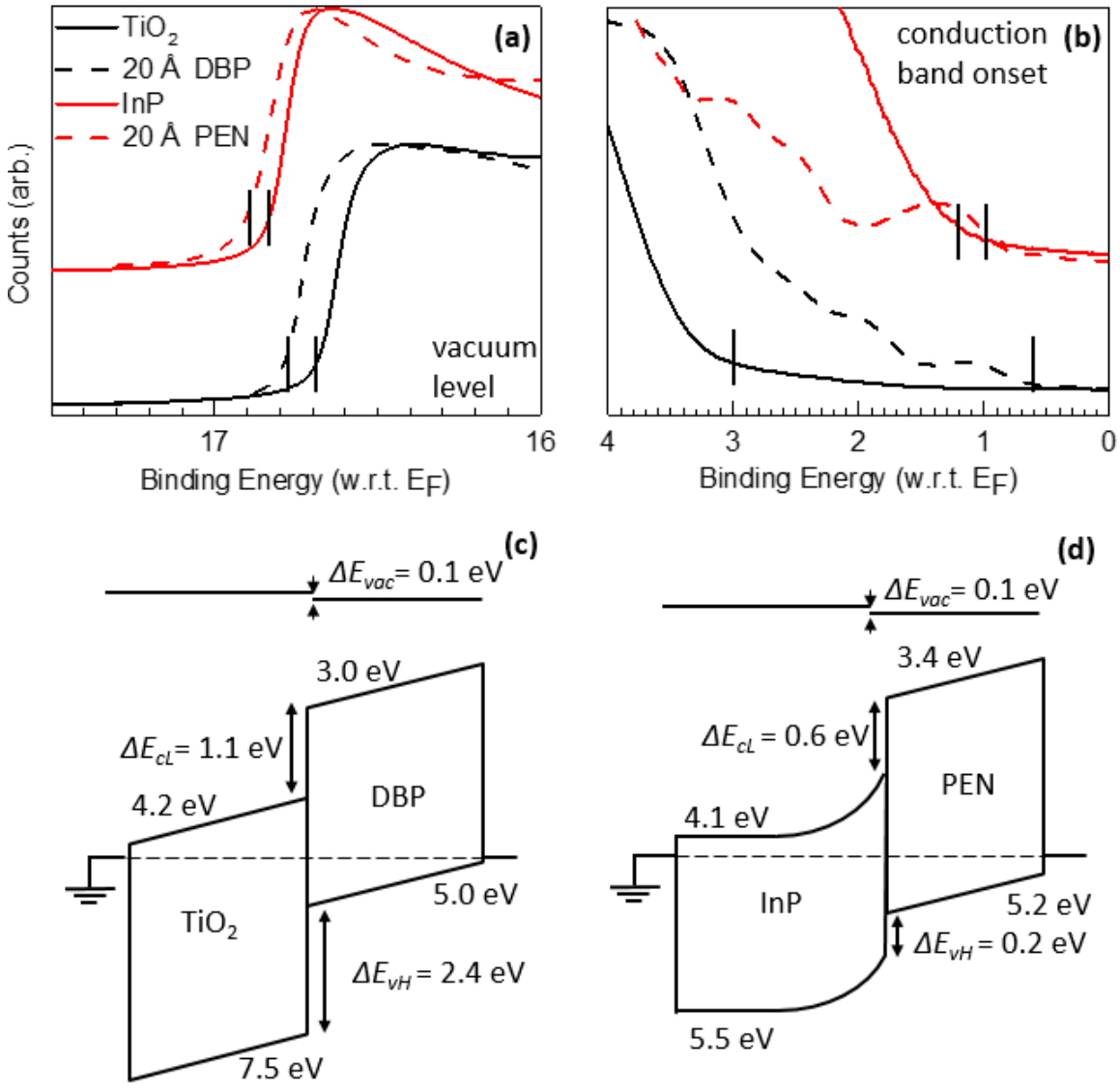

Figure 4.2: UPS spectra of (a) TiO_2 (bottom, solid line), TiO_2 with a 20 Å thick DBP film (bottom, dashed), InP (top, solid) and InP with a 20 Å thick PEN film (top, dashed). The line marks represent the secondary emission cut-off extracted from the spectra (16.7, 16.8, 16.8 and 16.9 ± 0.1 eV, respectively). (b) The low binding energy region providing information about the IPs. The short vertical lines indicate the VB/HOMO level onset energies (3.0, 0.6, 1.2 and 1.0 ± 0.1 eV, respectively). (c) Equilibrium energy level diagrams of the TiO_2/DBP (d) and InP/PEN OI-HJ devices inferred from the UPS data. The CB and LUMO levels are estimated from a combination of the UPS spectra and the optical gaps. The E_F is indicated by the dashed line. The ΔE_{vac} is the interface dipole, and ΔE_{cL} and ΔE_{vH} correspond to the energy level offsets at the conduction and valence levels, respectively. Figure reproduced from Ref. [12].

current under forward bias, and stable reverse bias characteristics with breakdown ranging from −15 V to −20 V.

Figure 4.2 shows the UPS spectra for the two OI-HJs (top) and the equilibrium band diagrams inferred from these data (bottom). Figure 4.2(a) shows the high binding energy region of the inorganic semiconductor and of the inorganic with a 20 Å organic films deposited on top. From the spectra we determine heterointerface dipoles ΔE_{vac} of 0.1 ± 0.1 eV at both the TiO_2/DBP and the InP/PEN interfaces. Figure 4.2(b) shows the low binding energy region of the spectra for the two systems from which we infer the E_v energies and HOMOs and their alignments. We estimate the E_c energies and LUMOs by adding the optical gap to the E_v energies and HOMOs [1, 9, 17, 18] to infer 2.4 ± 0.1 eV (1.1 ± 0.1 eV) offset energies between the $\Delta E_{cL}(\Delta E_{vH})$ of TiO_2 and the HOMO (LUMO) of DBP. For the InP/PEN OI-HJ, the $\Delta E_{cL}(\Delta E_{vH})$ is considerably smaller, at 0.2 ± 0.1 eV (0.6 ± 0.1 eV). Analysis of the UPS data, summarized in the equilibrium band diagrams shown in Fig. 4.2(c) and Fig. 4.2(d) indicates that both systems form type II OI-HJs. In constructing the band diagram for TiO_2/DBP, we have assumed a uniform field throughout the structure since both the organic and inorganic are fully depleted. For the InP/PEN, we assume the organic is fully depleted while the depletion width extends only a few microns into the moderately doped InP.

Wide band gap semiconductor junctions

The *EQE* of the TiO_2/DBP device as a function of temperature is shown in Fig. 4.3. The shape of EQE spectra in the range 450 nm $< \lambda <$ 650 nm matches that of the DBP absorption (also shown), since the wide band gap TiO_2 is transparent at $\lambda > 375$ nm. At room temperature, the *EQE* peaks at 13% at $\lambda = 600$ nm and decreases to 4% at $T = 194$ K. The shape of the *EQE* spectrum does not change with temperature, although its magnitude decreases monotonically. The inset shows an Arrhenius plot of the *EQE* at $\lambda = 604$ nm, which yields an activation energy of $\Delta E_{EQE} = 77 \pm 10$ meV.

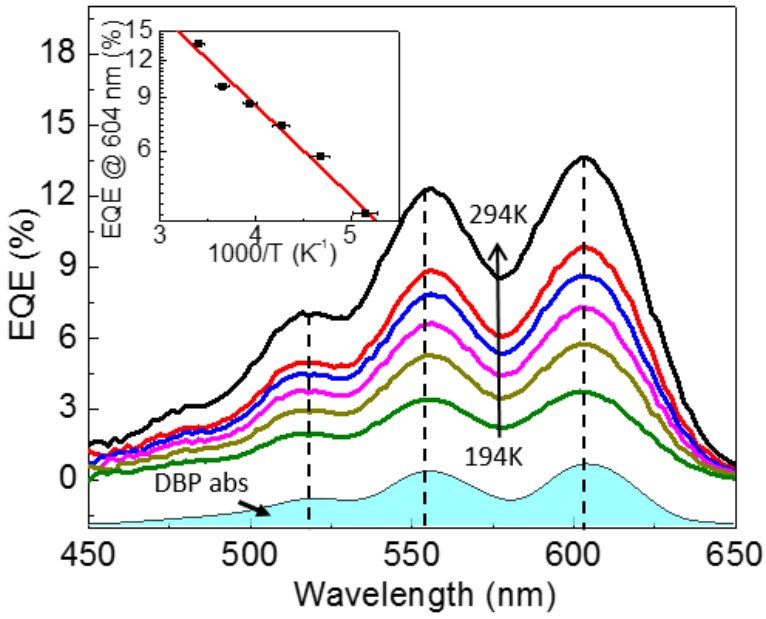

Figure 4.3: EQE vs. λ at several Ts of a TiO_2/DBP OI-HJ device. The vertical dashed lines indicate the peak positions of the several DBP vibronics. Also shown for reference is the DBP absorption spectrum (shaded region). The data are taken at 20 K intervals. Inset: The EQE at $\lambda = 604$ nm is plotted vs. $1000/T$. Fit to the data (solid line) yields an activation energy of $\Delta E_{EQE} = 77 \pm 10$ meV. Figure reproduced from Ref. [12].

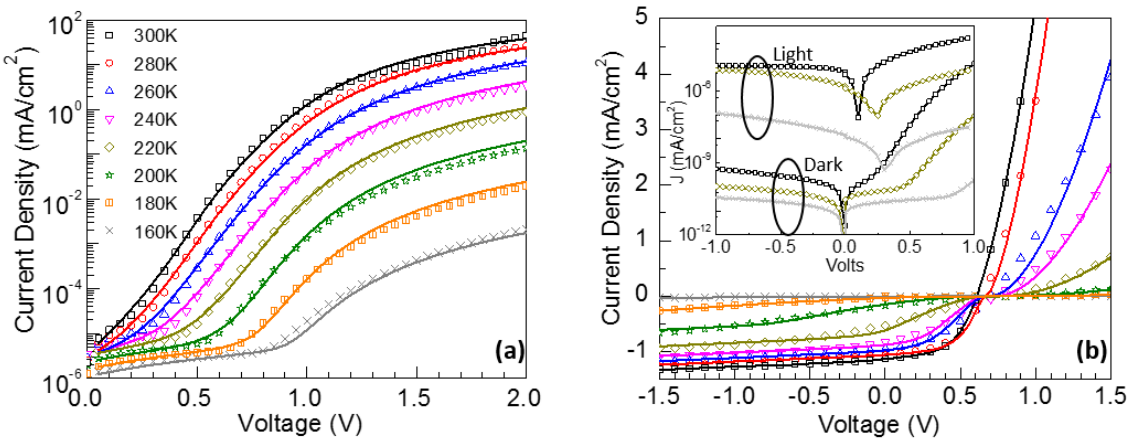

Figure 4.4: $J-V$ characteristics and fits at several Ts for a TiO_2/DBP OI-HJ device (a) in the dark and (b) under illumination. Data are shown by symbols and fits by lines. The fit parameters are summarized in Table 4.1. Inset: Dark and illuminated $J-V$ characteristics replotted on a log scale at temperatures of 160 K, 220 K, and 300 K starting from the bottom. Figure reproduced from Ref. [12].

The $J-V$ characteristics in the dark are shown in Fig. 4.4(a). They exhibit a pronounced roll-off at $V_a > 1$ V due to space-charge, departing from an exponential increase. The onset voltage for roll-off decreases with decreasing T. At low currents, there is an exponentially increasing plateau region that resembles a diode with a very high ideality factor. The $J-V$ behavior of the plateau is symmetric about 0 V. The illuminated $J-V$ characteristics are shown in Fig. 4.4(b). At $V_a > V_{OC}$, the photocurrent decreases with temperature, similar to the dark current. The photocurrent is symmetric around V_{OC} (inset of Fig. 4.4). The FF and PCE also decrease with T due to a reduction in photocurrent in the 4^{th} quadrant. The saturated photocurrent at high reverse bias $V_a > -1$ V also decreases with decreasing temperature. A temperature-independent linear slope in photocurrent is observed at high reverse bias, and has been shown previously to be due to photoconductivity of the organic layer [19].

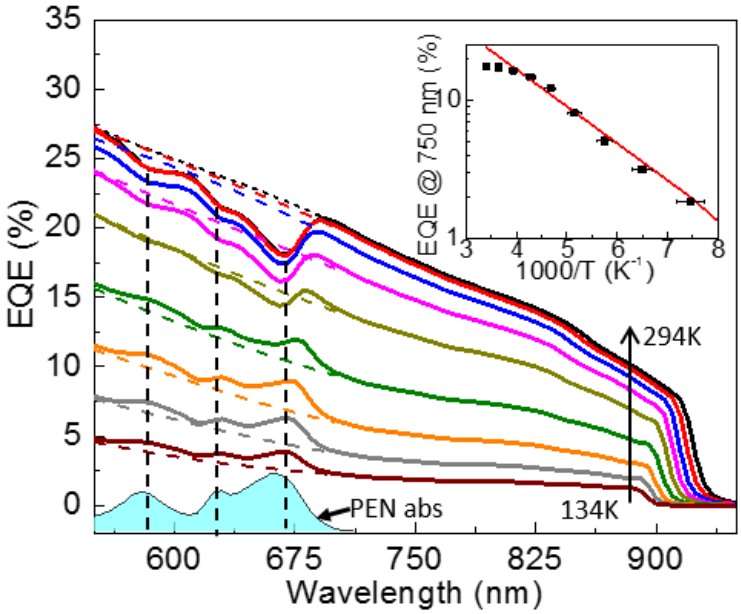

Figure 4.5: EQE of a InP/PEN OI-HJ device vs. T (solid lines) along with the spline fit (dashed lines) used to estimate the InP background. PEN absorption is also shown as reference (shaded region). The vertical dashed lines indicate the peak positions of the several PEN vibronics. Inset: EQE at a wavelength of 750 nm vs. $1000/T$ yields an activation energy of $\Delta E_{EQE} = 55 \pm 10$meV. Figure reproduced from Ref. [12].

Moderate band gap semiconductor junctions

The EQE vs. T data for the InP/PEN OI-HJ is shown in Fig. 4.5. The shape of the PEN absorption, consisting of three vibronics within the interval of $\lambda = 550$ nm to 700 nm, is also shown (shaded region). The EQE at wavelengths outside of the PEN absorption decreases uniformly with temperature, with the long wavelength cut-off decreasing from $\lambda = 925$ nm to 900 nm, consistent with the behavior of direct band gap semiconductors (see Eq. 1.20 and §1.4.3). The inset shows the magnitude of the EQE at $\lambda = 750$ nm vs. $1/T$, yielding an activation energy of $\Delta E_{EQE} = 55 \pm 10$ meV. Within the PEN absorption region, the spectra show three dips at high temperature, and then emerge as peaks as T is reduced.

The forward biased $J - V$ characteristics in the dark are shown in Fig. 4.6(a), and exhibit an exponential increase of current with V_a. Unlike the wide band gap case, the

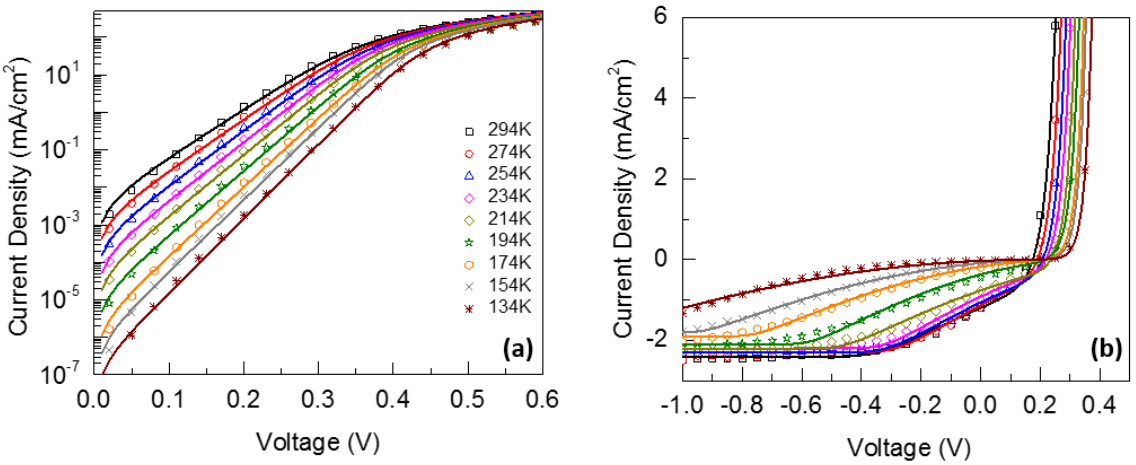

Figure 4.6: $J-V$ characteristics and fits at several different Ts for a InP/PEN OI-HJ device (a) in the dark, and (b) under illumination. The fit parameters are summarized in Table 4.2. Data are shown by symbols and fits by lines. Figure reproduced from Ref. [12].

roll-off follows an Ohmic (i.e. $J \propto V_a$) behavior at high forward bias. The illuminated $J-V$ curves are shown in Fig. 4.6(b). At $V_a > V_{OC}$, the forward current behaves similar to its dark current characteristic, whereas at $V_a < V_{OC}$ it has an S-kink similar to the illuminated TiO_2/DBP characteristics. The FF and PCE also decrease with temperature. The saturated photocurrent at each temperature increases linearly with voltage due to the photoconductivity of the PEN layer.

4.1.4 Discussion

The EQE spectra for both the TiO_2/DBP and InP/PEN diodes show evidence of excitons that diffuse to the OI-HJ forming an HCTE and subsequently dissociating to contribute to the photocurrent. However, the behavior of the HCTE with T is strikingly different in the two cases.

In the wide band gap case, the lack of overlap in the absorption spectra of the organic and inorganic unambiguously shows the contribution of DBP excitons to the photocurrent in the EQE spectra of Fig. 4.3. Since the measured EQE is approximately 100 times higher than an Au (100 nm)/DBP (100 nm)/ITO (72 nm) photoconductor, we

conclude that the high EQE of the OI-HJ is due to exciton diffusion to the interface and subsequent dissociation into free charge. The peak magnitude of the EQE decreases with an activation energy of $\Delta E_{EQE} = 77 \pm 10$ meV (see inset, Fig. 4.3). The temperature activation of the EQE can result from a decrease in the charge collection efficiency, in the exciton flux to the interface, or in the HCTE dissociation efficiency. Although the HCTE becomes increasingly stable at reduced temperatures, it is not expected to change sufficiently over this temperature range to result in a 3-fold decrease in EQE. Furthermore, a low binding energy is expected because of the high dielectric constant of TiO_2 (see Fig. 3.2). From this, we infer that the observed temperature activation results from a trade-off between the exciton flux to the interface and the charge collection efficiency. Fits to the $J-V$ characteristics of the TiO_2/DBP junction yields $\Delta E_{EQE} = 40 \pm 10$ meV for the exciton flux to the interface. This suggests that at $V_a = 0$ V, the V_{bi} and mobility of the DBP are sufficiently high that the EQE decrease with temperature is due to a reduction in exciton flux to the OI-HJ.

In contrast to the wide band gap case, the PEN and InP EQE spectra fully overlap, and the excitonic contribution to the EQE is evident only at lower temperature. That is, at high temperature, the EQE in the spectral region of the PEN absorption results in a net loss, whereas at low temperature the PEN provides an increase to the total photocurrent. To clarify the contributions of PEN, we subtract the InP response between $\lambda = 550$ nm to 700 nm using a spline fit to the background, as shown by the dashed lines in Fig. 4.5. The total EQE minus the extrapolated background, further normalized by the charge collection efficiency, are shown in Fig. 4.7. The collection efficiency is obtained by assuming that it is directly proportional to the EQE in the region where only InP absorbs. It is the same for the organic and inorganic since for both photogenerated charges are lost through recombination at the OI-HJ. Furthermore, the activation energy of the InP EQE is $\Delta E_{EQE} = -55 \pm 10$ meV (see inset, Fig. 4.5), which is similar to the activation energy for the PEN mobility of $E_\mu = 71 \pm 10$ meV, obtained from $J-V$ fits

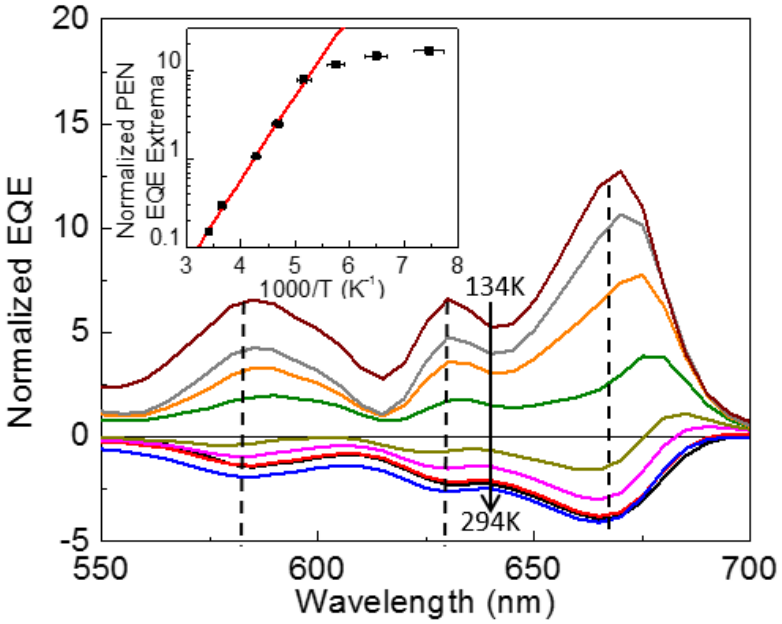

Figure 4.7: *EQE* vs. T of PEN at 20 K intervals in an InP/PEN OI-HJ device. The absolute values of *EQE* are obtained by subtracting the InP spline fit background in Fig. 4.5. The *EQE* contribution from PEN is then referenced to its value at each temperature divided by the background *EQE* from InP at a wavelength of 750 nm. The vertical dashed lines indicate the peak positions of the several PEN vibronics. Inset: Peak *EQE* for the 0—0 (lowest energy) vibronic vs. $1000/T$, gives an activation energy of $\Delta E_{EQE} = 0.21 \pm 0.04$ eV. Figure reproduced from Ref. [12].

(see Table 4.2). This indicates that the change in carrier collection efficiency, resulting from the low hole mobility in PEN, is responsible for the temperature activation of the EQE in the region where only InP absorbs.

It is apparent that at high temperatures, PEN excitons recombine after photogeneration in the bulk of the thin film or are quenched at the interface due to trap states at the InP surface. Hence, at the highest temperatures, there is no change in the absorption signal since nearly all excitons recombine prior to dissociation. However, as temperature is decreased, the loss decreases, eventually resulting in a positive contribution to the photocurrent at $T \leq 214$ K, with the largest increase occurring immediately at the long wavelength PEN absorption edge. The increase in EQE contributed by PEN is approximately 18% from the highest to lowest temperature. The magnitude of that contribution is nearly as high as that of InP at $T = 134$ K, and in all cases is 20 times higher than the photoconductivity obtained for an Al (15 nm)/PEN (30 nm)/ITO (150 nm) sample. Note, too, that the peaks in EQE align to those of the absorption spectra, except near the transition from loss to gain at $T = 214$ K where there is a small bathochromic shift of the long wavelength tail of the $0-0$ vibronic. This peak progressively shifts back towards the $0-0$ vibronic maximum with decreasing temperature as gain dominates over loss. The enhanced contribution in the PEN EQE near the excitionic absorption edge results since the PEN layer at the long wavelength absorption cutoff is nearly transparent. This results in uniform illumination and hence exciton generation nearer to the OI-HJ where dissociation becomes dominant over interface recombination. A similar shift is commonly observed in the photoluminescence maxima of semiconductors where the convolution of the emission and absorption spectra result in a maximum at the transparency edge of the medium.

Interestingly, the activation energy of the difference spectra is $\Delta E_{EQE} = 0.21 \pm 0.04$ eV, and has the opposite dependence with temperature compared to the wide band gap case. This is indicative of the different role that surface states play in the two devices. For

TiO_2/DBP, the surface states are not active under the conditions tested, yet for InP/PEN, surface trap occupancy is found to change, reducing the rate of HCTE and/or exciton quenching as the temperature is reduced. Indeed, the activation energy measured is consistent with the position of InP surface states relative to the Fermi energy, as inferred from Li *et al.* [8] With the deposition of PTCDA on top of *p*-InP, they find that the barrier height changes by 9 meV. Adding this to the barrier height obtained from UPS (1.1 ± 0.1 eV) and the InP band gap (1.35 eV), we find that the surface states should be located at 0.26 ± 0.1 eV above the E_v maximum, consistent with our measurement of ΔE_{EQE}. Alternatively, since the ΔE_{OI} is nearly resonant with the PEN triplet state energy (~ 0.9 eV), reduction in T could increase the efficiency of resonant triplet transfer [20, 21].

There is a possibility that FRET from the organic to inorganic semiconductor can bypass the formation of the HCTE in the charge photogeneration process. The FRET probability is proportional to the overlap between the absorption spectrum of InP and photoluminescence (PL) spectrum of PEN (see §1.6.4). To estimate the probability of Förster transfer from PEN to InP, we measured the PL of a 100 nm thick PEN film on an oxidized Si substrate vs. T. The film was pumped with $\lambda = 337$ nm emission from a N_2 laser at 1.5x10^4 μJ/cm^2. Similar to Park *et. al.* [22], we find the PL exhibits broad features at high energy $\lambda = 500$ nm to 750 nm) that do not change significantly with temperature, and two peaks at longer wavelength ($\lambda = 775$ nm to 925 nm) that increase with decreasing temperature. Between 294 K and 134 K, the PL in the long wavelength region increases five-fold. However, the PL efficiency (η_{PL}) is low at all temperatures, with a maximum of $\eta_{PL} = 0.013\%$ at 134 K. To quantify the effects of FRET, we calculate the Förster radius using Eq. 1.30 of 4 Å. We note that Eq. 1.30 is valid only for point-dipole to point-dipole coupling. Other approximate solutions exist for point-dipole to near band-edge transitions in a semiconductor [23]. Hence, the contribution to the EQE at $\lambda = 663$ due to FRET can arise only from excitons absorbed within R_o of the interface. For $L_D \approx 10$ nm and an absorption coefficient of 10^5 cm^{-1}, we

obtain the contribution from FRET of $< 0.01\%$. We note this is an *upper limit*, since the first few monolayers of PEN stand normal relative to the substrate plane [24, 25]. Thus, their emission dipole moments are oriented such that $\kappa \to 0$ implying that transfer is preferentially in-plane and cannot couple efficiently to the InP substrate.

$J-V$ characteristics: wide band gap semiconductor junctions

As in all fits of $J-V$ data, several parameters emerge whose values provide insight into the detailed dynamics of the devices studied. We find excellent fits to the data for both systems under reverse and forward bias, as well as illumination conditions and temperature. While the fits provide strong support for our analysis, in most cases the characteristics are primarily used to support the picture of the formation of an HCTE in both junctions.

Equation 4.2 is used to fit the $J-V$ characteristics of the TiO_2/DBP junction in the dark and under illumination in Fig. 4.4(a) and (b), respectively. For fits to the dark $J-V$ characteristics, we use J_{s1}, μ and $T_{t,O}$ as parameters. Furthermore, we vary J_{s1} and μ with temperature, since $J_{s1}(T)$ is a function of $k_{rec}(T)$, which in turn is proportional to $\mu(T)$ (see §3.5). For the $J-V$ fits under illumination, we also use the parameters from the fit in Fig. 4.4(a), but recognize that the k_{rec} can also depend on light intensity, and that J_X is a function of the temperature dependent exciton diffusion in disordered organic thin films. For the fits, we take the approximate experimental values of $\epsilon_O = 4$, $V_{bi} = 0.5$ V, and injection barriers $\phi_{c,a} = 0.2$ eV. Finally, we note that since the currents in the low forward current plateau region in Fig. 4.4(a) are small (< 100 pA), they can be influenced by artifacts such as the long time constants of trapped carriers or dielectric leakage in the probes contacting the device. Therefore, the reliability of the fits corresponding to the second term of Eq. 4.2 is reduced by these measurement inaccuracies. The fit results are shown by lines in Fig. 4.4, with the parameters used provided in Table 4.1.

Table 4.1: Fitting parameters for TiO_2/DBP $J-V$ characteristics

Parameter	Value
$T_{t,o}$	710 ± 80 K
μ_∞	6 ± 4 cm^2/(Vs)
ΔE_μ	0.33 ± 0.06 eV
$J_{s1,\infty}$ (dark)	8 ± 4 A/cm^2
E_a (dark)	0.19 ± 0.01 eV
J_{s1} (light)	80 ± 24 mA/cm^2

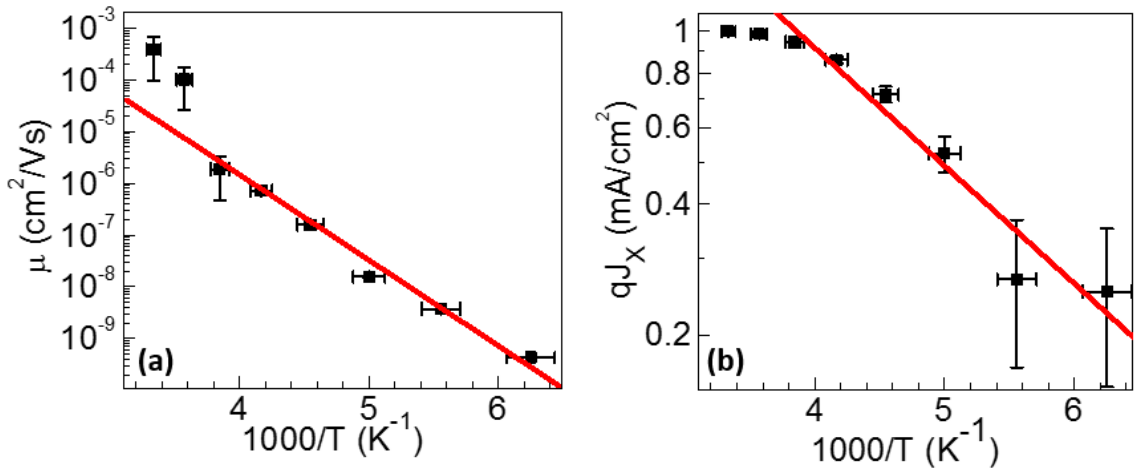

Figure 4.8: (a) Mobility vs. temperature (1000/T) obtained from $J-V$ characteristics of TiO_2/DBP OI-HJ device shown in Fig. 4.4. An activation energy of $\Delta E_\mu = 0.33 \pm 0.06$ eV is obtained from the fit (solid line). (b) Exciton flux to the interface (qJ_X) vs. $1000/T$ obtained from the $J-V$ fits under illumination, yielding an activation energy of $\Delta E_{EQE} = 40 \pm 10$ meV. Figure reproduced from Ref. [12].

From these fits, we find the Arrhenius mobility (see Eq. 1.11), where the thermal activation energy is $\Delta E_\mu = 0.33 \pm 0.04$ eV (see Fig. 4.8(a)) as inferred from the space-charge roll-off region of the forward characteristics in Fig. 4.4. This magnitude of activation energy is consistent with previous measurements of organic films whose charge transport is dominated by polaron hopping between discrete sites with energetic disorder [26, 27]. To confirm that the space-charge roll-off is due to the properties of DBP, we fabricated a device that replaced TiO_2 with a thin C_{60} layer, with the structure: ITO (150 nm)/C_{60} (10 nm)/DBP (30 nm)/MoO_3 (15 nm)/Al (100 nm). Here the C_{60} film has a considerably higher mobility (5.1 x 10^{-2} $cm^2/(Vs)$) [28] than DBP and hence is not current-limiting in the test structure. This organic device exhibits a similar thermal activation for the space-charge roll-off as the TiO_2/DBP device, indicating that the observed effects are indeed due to DBP. The thermally activated mobility fully accounts for the decrease in FF versus temperature in the $J-V$ characteristics under illumination in Fig. 4.4(b). This is apparent in the inset, Fig. 4.4(b), which provides the data and fit on a semi-log scale for selected temperatures. Under illumination, there is surprising symmetry in the current centered about the V_{OC} (identified by the dip in current where it switches from positive to negative). This symmetry is a result of space-charge effects dominating current transport in both the forward and reverse directions. Thus, at $V > V_{OC}$, holes are injected from the contact and transported to the OI-HJ by drift. At $V < V_{OC}$, the direction of the current is reversed as the photogenerated holes are transported by drift away from the OI-HJ to the anode. In this case, the sign of Eq. 2.11 is reversed and the field at the contact, F_c, is replaced by the field at the interface, F_{OI-HJ}.

Reduction in FF with T can result from field-dependent dissociation of the HCTE state. Accurate fits to FF using Eq. 4.2, where the binding energy of the HCTE is assumed to be small, suggest that field-dependent dissociation is not dominant. The low HCTE binding energy is further supported by the small value of $\delta_I = 0.22 \pm 0.04$

obtained from the fit. Using the uniform field approximation, for $\epsilon_O = 4$, we infer that $\epsilon_I \approx 35$. This falls within the range of dielectric constants reported for TiO_2 from 15 to 250, depending on deposition condition [29, 30]. In our case, we measured ϵ_I via the capacitance of a $(1mm)^2$ ITO (150 nm)/TiO_2 (60 nm)/Au (100 nm) sample. The capacitance ranges from 3 nF to 12 nF, corresponding to $\epsilon_I/\epsilon_O \approx 25-100$.

A dependence of J_{s1} on illumination intensity is evident from Fig. 4.4(b), inset. From the $J-V$ fit we find that J_{s1} has an activation energy of $E_a = 0.19 \pm 0.01$ eV in the dark, but lacks a pronounced temperature dependence under illumination. From this we infer that k_{rec} is diffusion limited in the dark when carrier density at the interface is low, and therefore both J_{s1} and μ have the similar activation energy. However, when illuminated, the carrier density at the interface is large, such that k_{rec} is limited by the short charge recombination lifetime at the interface, which is expected to be only weakly temperature dependent.

Finally, J_X has an activation energy of $\Delta E_{EQE} = 40 \pm 10$ meV from Fig. 4.8(b). This results from a reduction in the exciton diffusion length in DBP with temperature, consistent with previous reports for organic materials [31, 32].

$J-V$ characteristics: moderate band gap semiconductor junctions

Equation 4.4 is used to fit the measured $J-V$ characteristics (data points) in the dark and under illumination with results (lines) in Fig. 4.6(a) and (b), respectively. In the dark, thermionic emission (second term on the right hand side of Eq. 4.4) dominates. For the illuminated $J-V$ characteristics, the first term on the left hand side of Equation 4.4 dominates when fitting the inflection below $V < V_{OC}$. The fit parameters are summarized in Table 4.2.

The values of saturation current pre-factor, $J_{therm} = J_{s2} exp\left(-\frac{\Delta E_{vH}}{k_B T}\right)$ in Eq. 4.4, obtained from fits to the dark data are shown in Fig. 4.9(a), with an activation energy of $\Delta E_{vH} = 0.24 \pm 0.04$ eV, which corresponds to the valence energy offset at the OI-HJ.

Table 4.2: Fitting parameters for InP/PEN $J-V$ characteristics

Parameter	Value
μ_∞	$3\text{x}10^{-5} - 2\text{x}10^{-6}$ cm^2/(Vs)
ΔE_μ	71 ± 10 meV
J_{s2} (dark)	5 ± 4 mA/cm^2
J_s (light)	$10^{-10} - 10^{-12}$ mA/cm^2
R_s	0.44 ± 0.02 Ω cm^2

This also agrees with $\Delta E_{vH} = 0.2 \pm 0.1$ eV directly measured by UPS. The fits yield an ideality constant that increases from $n_{therm} = 1.25 \pm 0.01$ at $T = 294$ K to $n_{therm} = 1.96 \pm 0.01$ at $T = 134$ K (see inset, Fig. 4.9(a)). This increase with decreasing temperature is due to the increasing importance of recombination at the HJ, resulting from a decrease in the probability for injected carriers to surmount the interface barrier. This is also consistent with the behavior of conventional Schottky barrier diodes with temperature [33, 34].

The PEN hole mobility vs. T obtained from fits to the illuminated $J-V$ characteristics are plotted in Fig. 4.9(b), showing $\Delta E_\mu = 71 \pm 10$ meV. To independently determine μ, we measured the dark $J-V$ characteristics of an Au/MoO_3 (10 nm)/PEN (200 nm)/MoO_3 (10 nm)/Au. From this, we estimate an upper limit of $\mu \approx 10^{-6}$ cm^2/(Vs), in agreement with the values in Fig. 4.9(b). The low mobility normal to the substrate arises since the PEN molecular plane typically lies perpendicular to the substrate. This leads to a large anisotropy with the lowest mobility normal to the plane, consistent with measurements [35]. Also, 40 nm thick PEN film on InP has a root mean square roughness of 10 nm as determined by atomic force microscopy. The small ΔE_μ suggests, that hole transport is limited by hopping at grain-boundaries [26, 36], in contrast to the polaron trap and release model used to describe the larger ΔE_μ of DBP.

Finally, the illuminated $J-V$ data give a temperature independent saturation current pre-factor, $J_{s1} exp\left(\frac{-E_t}{n_I k_B T}\right)$, in Eq. 4.4. From this, we infer that the inflection in the illuminated $J-V$ is due to electrons trapped in discrete trap states at the inorganic surface with free holes in the organic. For an electron quasi-Fermi level pinned at the

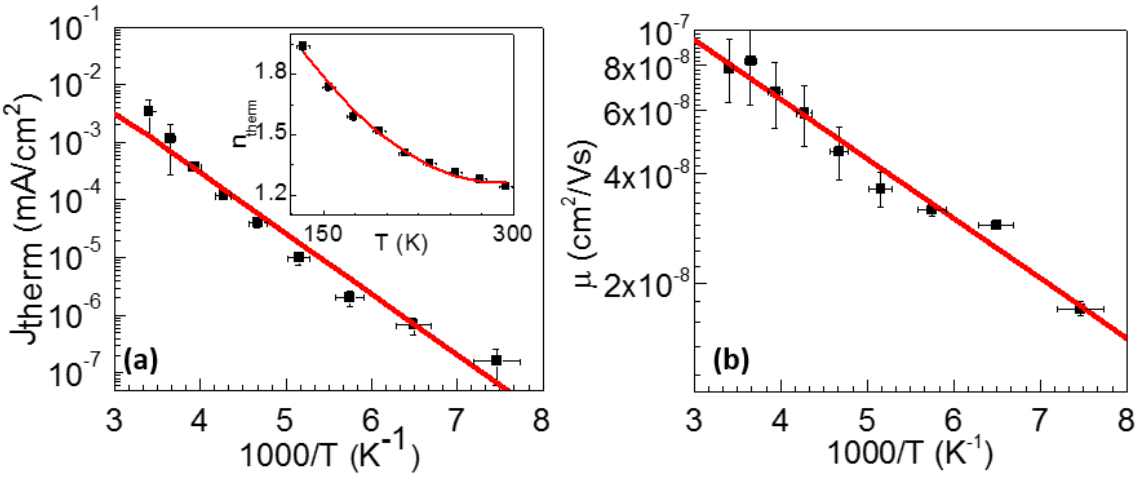

Figure 4.9: (a) Saturation current vs. $1000/T$ obtained from $J-V$ fits in the dark for an InP/PEN OI-HJ device (Fig. 4.6), yielding an activation energy of $\Delta E_{vH} = 0.24 \pm 0.04$ eV. This corresponds to the valence energy offset at the OI-HJ. Inset: Ideality factor, n_{therm} vs. T. (b) Mobility vs. $1000/T$ obtained from illuminated $J-V$ fits. An activation energy of $\Delta E_{\mu} = 71 \pm 10$meV is obtained from the fit (solid line). Figure reproduced from Ref. [12].

OI-HJ by a high density of interface traps [37], the saturation current is expected to be temperature independent, as observed.

4.2 ZnO/CBP OI-HJ

The inorganic semiconductor, ZnO is attractive for studying HCTE states due to its small dielectric constant [38], which results in a large HCTE binding energy. The properties of the HCTE at the ZnO/organic semiconductor HJ have historically been studied in DSSCs [39–41], and recently in OI PV [42–45]. Defect states on ZnO surfaces that result from oxygen vacancies, Zn interstitials [46] or from capping by organics [47, 48] play an important role in governing the HCTE-mediated exciton-to-charge conversion efficiency. For example, single crystal ZnO surfaces capped with thiacyanine and eosine dyes exhibit a low quantum yield ($\phi \approx 10^{-2}$) as compared with polycrystalline ZnO surfaces ($\phi \approx 1$). This is attributed to ZnO surface defects that promote recombination and quenching of the HCTE and its exciton precursor [39, 40]. Strothkämper,

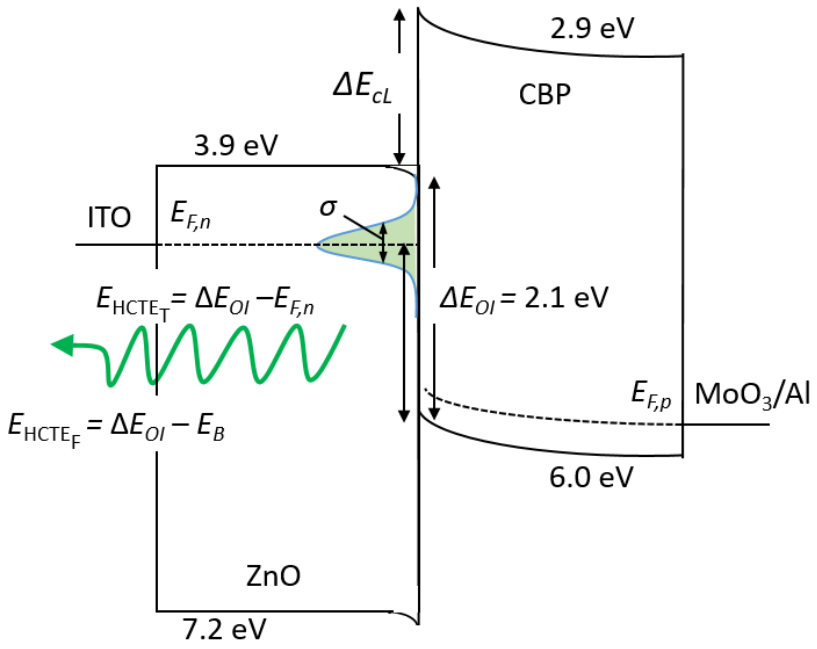

Figure 4.10: Energy level diagram of ZnO/CBP OI-HJ device under forward bias. Due to the asymmetry in charge mobilities of the two materials, under forward bias, ZnO remains in equilibrium while the V_a is primarily dropped across CBP. The energy of the singlet $\mathrm{HCTE_F}$ is the ΔE_{OI} (2.1 ± 0.1 eV) minus E_B of the state (9 meV). The singlet $\mathrm{HCTE_T}$ has an emission energy of ΔE_{OI} minus the $E_{F,n}$ with respect to the ZnO E_c ($E_{F,n} = 0.2-0.8$ eV) minus E_B of the state (60—400 meV). The $\mathrm{HCTE_T}$ emission has a FWHM of $\sigma = 300 \pm 10$ meV as determined from the EL spectral half width. Figure reproduced from Ref. [49].

et al. attached systematically lengthened perylene bridge units to the ZnO surface and observed no change in the HCTE dissociation yield or lifetime, from which they concluded that interfacial states formed between the dye and ZnO are primarily responsible for the high HCTE recombination rate [41]. Bound states at ZnO/polymer [42], $Zn_{1-x}Mg_xO$/polymer [43] and ZnO/small molecule [44] HJ have also been identified by transient and electroluminescence (EL) spectroscopy. DFT studies of P3HT on pristine ZnO single crystal surfaces predict the existence of surface-bound HCTEs with a low dissociation yield compared to C_{60}/P3HT bound polaron-pairs due to poor coupling of the states to the ZnO bulk [41].

To gain further insight into the properties of the HCTE, we characterize a ZnO/CBP

OI-HJ by measuring EQE, PL, and EL spectra as functions of T and V_a. The proposed energy level diagram of the device under high forward bias ($V_a > 3$ V) and energetic levels of relevant states is shown in Fig. 4.10. We use CBP due to its wide energy gap which maximizes $\Delta E_{OI} = 2.1 \pm 0.1$ eV, at the HJ and shifts the the photon emission energy of the HCTE to the visible wavelength range. The peak EQE for the device at a wavelength of $\lambda = 332$ nm is $6.0 \pm 0.2\%$, which corresponds to the CBP absorption maximum. This suggests that Frenkel excitons in the organic efficiently convert into free carriers through an intermediate HCTE. We directly observe the HCTE by EL, and find that the spectrum blue shifts with decreasing temperature from 300 K to 30 K, and increasing voltage from 3 V to 9 V. In addition, the EL spectra FWHM remains unchanged over this temperature and voltage range. Surprisingly, we do not observe HCTE PL emission via exciton generation in CBP even at temperatures as low as 25 K. We conclude that the EL signal results from $HCTE_T$ which are due to electrons injected into ZnO surface defect states. In contrast, the CBP exciton quantum yield at the OI-HJ occurs via $HCTE_F$. Quantum mechanical simulations confirm that the $HCTE_F$ has a lower binding and oscillator strength compared to the $HCTE_T$, which is consistent with the absence of PL from $HCTE_F$.

4.2.1 Theory

We follow the procedure outlined in §3.2 to predict the properties of $HCTE_F$ and $HCTE_T$ at ZnO/CBP OI-HJ. The MD simulations of CBP on the ZnO $(10\bar{1}0)$ plane, which is reported to be the dominant surface in polycrystalline ZnO thin films [50], yields an average distance of 4 Å between a flat-lying CBP molecule and the ZnO surface, as shown in Fig. 4.11(a). The spatial charge distribution of the cationic CBP is found via DFT calculation, with the result shown in Fig. 4.11(b). To solve the Schrödinger equation (Eq. 3.3), we found that it is adequate to let $n = 2$, accounting for two half-charges located at the symmetry points on the two halves of the CBP molecule indicated by the

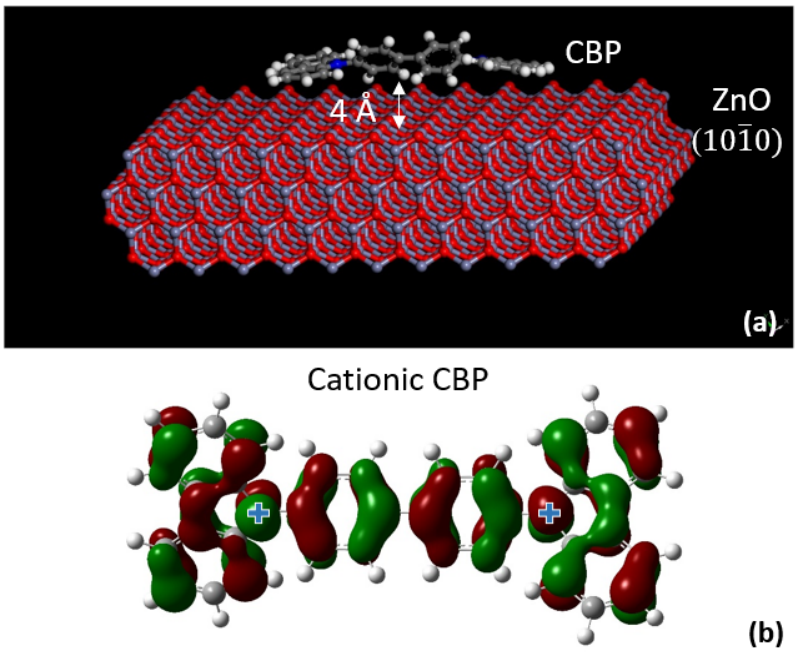

Figure 4.11: (a) MD simulation of CBP on (10$\bar{1}$0) ZnO plane yielding an average distance of 4 Å for CBP molecules from the ZnO surface. (b) DFT calculation of cationic CBP, showing spatial probability distribution of the hole. The plus signs indicate the location of two fractional point charges used in the electron Hamiltonian. Figure reproduced from Ref. [49].

plus signs in Fig. 4.11(b).

The eigenvalues obtained from Eq. 3.3 describe the HCTEs with the lowest energy solution of interest in this work. Due to the spin-allowed radiative relaxation of these quasi-particles, they are labeled singlet ^{1}HCTE states. To show the delocalization of the $^1\text{HCTE}_\text{F}$ and trapped $^1\text{HCTE}_\text{T}$, we plot the spatial probability density in Fig. 4.12(a) and the linear probability density as a function of distance from the OI-HJ in Fig. 4.12(b). The horizontal line at x = 0 indicates the position of the OI-HJ. Parameters $m_{h,O} = 1.0m_0$, $m_{h,I} = 0.22m_0$, $\epsilon_O = 4$, $\epsilon_I = 8$ and $\Delta E_{cL} = 1$ eV, are used for the simulation [38, 51]. Also, for simulating $^1\text{HCTE}_\text{T}$, the screening factor $S = 0.94$ and $S = 3.76$, which results in an electron trap state 0.2 eV and 0.8 eV below the ZnO E_c, respectively, and are comparable to what has been reported for trap states caused by oxygen vacancies [46]. We caution that the description of the trap state is simplistic since it determines

both the trap depth and radius, allowing for only qualitative conclusions.

In Fig. 4.12(b) we show that on the ZnO side, the extent of electron delocalization of the $^1\text{HCTE}_\text{F}$ is three times that of the $^1\text{HCTE}_\text{T}$. Further, on the CBP side, the $^1\text{HCTE}_\text{T}$ wave function extends further into the organic due to confinement of the electron near the interface due to the trap potential. This leads to a higher binding energy and larger oscillator strength than for $^1\text{HCTE}_\text{F}$. The binding energy of $^1\text{HCTE}_\text{T}$ for a trap state 0.2 eV and 0.8 eV below ZnO conduction band are 60 meV and 430, meV respectively, while that of $^1\text{HCTE}_\text{F}$ is 9 meV. The oscillator strength of trapped charge transfer state is four orders of magnitude higher than that of the free state, which yields radiative lifetimes of approximately 400 ns and 10 ms, respectively.

The $^1\text{HCTE}_\text{F}$ PL and EL spectral peaks are expected at energies of $\Delta E_{OI} - E_B$. The $^1\text{HCTE}_\text{T}$ peak is predominantly determined by the electron energy in the ZnO, which is determined by the $E_{F,n}$. To determine the dependence of $^1\text{HCTE}_\text{T}$ on V_a and T, we calculate the $\Delta E_{F,n}(V,T)$. We neglect the change in E_B because each trap level is expected to have a range of binding energies depending on the delocalization of the electron. We also neglect $\Delta E_{f,P}$ at the CBP side of the OI-HJ since the EL spectra peaks in excitonic HJs have been found to negligibly depend on V_a and T [52, 53]. Further, ZnO is also expected to have a uniform trap DOS through the E_g because it is deposited as an amorphous film with defect levels through the film [47, 48]. As a result, we expect trap DOS to be available for occupation at a given $E_{F,n}$. In the uniform field approximation:

$$\Delta E_{F,n}(V) = \Delta V_I = \delta_I \Delta V_a = \frac{\Delta V_a}{1 + \frac{\epsilon_I W_O}{\epsilon_O W_I}}. \tag{4.5}$$

Equation 4.5 is valid when both layers are depleted, which occurs when there is low carrier densities in ZnO and CBP. When there is high carrier density in ZnO (usually the case due to unintentional doping [38]), under forward bias holes accumulate in CBP since the hole mobility ($\sim 10^{-4}$ cm^2/(Vs) [54]) is at least five orders of magnitude

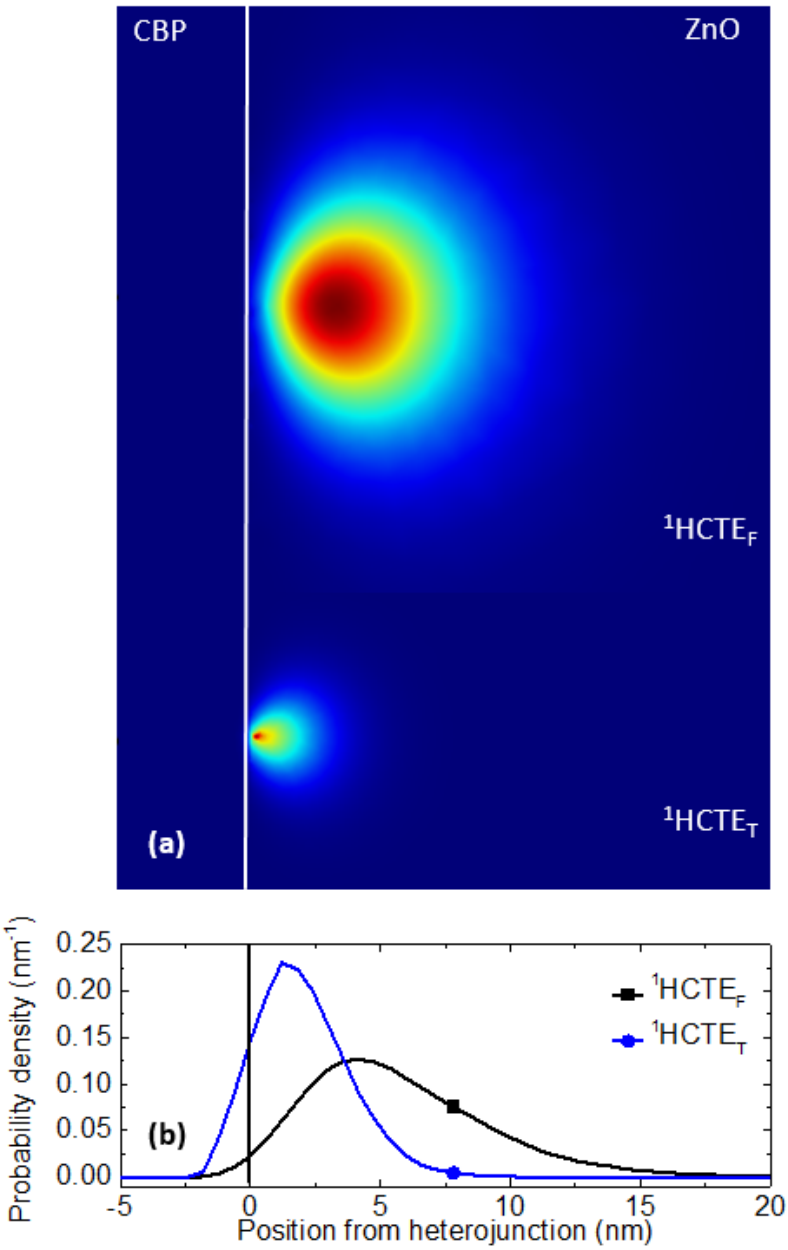

Figure 4.12: (a) Spatial probability density of the lowest eigenvalue solution of the singlet ^{1}HCTE$_F$ and ^{1}HCTE$_T$ at the Zno/CBP OI-HJ. The ^{1}HCTE$_F$ has a 9 meV binding energy, whereas ^{1}HCTE$_T$ has a 31 meV binding energy. (b) The probability density of the free and trapped ^{1}HCTE along the z-axis, perpendicular to the interface. The electron density on the CBP side of the OI-HJ increases for ^{1}HCTE$_T$ vs. ^{1}HCTE$_F$ resulting in a four orders of magnitude higher oscillator strength and radiative lifetime for ^{1}HCTE$_T$. Figure reproduced from Ref. [49].

lower than the electron mobility in sputtered ZnO ($\sim 10\ cm^2/(Vs)$) [38, 55]. As a result, ΔV_a is primarily dropped across CBP, and $\Delta E_{F,n}(V)$ and δ_I are small. Now $\Delta E_{F,n}(T)$ is determined from the free electron density at the ZnO side of the OI-HJ (see §1.4.4):

$$n_{HJ} = \frac{\sqrt{2m_{e,I}^3}}{\pi^2\hbar^3} \int_{E_c}^{\infty} \sqrt{E - E_c(T)} / \left(1 + exp\left(\frac{E - E_{F,n}}{k_B T}\right)\right) dE, \tag{4.6}$$

where E_c is a function of T. Equation 4.6 assumes a quadratic DOS for the ZnO E_c(see Fig. 1.6). For constant current density, n_{HJ} is also approximately constant with temperature due to the nearly temperature independent electron mobility in ZnO [56]. At high temperatures, the Boltzmann distribution is used to approximate Eq. 4.6 as Eq. 2.3, resulting in a linear dependence of $\Delta E_{F,n}(T)$ with ΔT, with a slope of $-k_B ln(n_{HJ}/N_c)$. At low temperatures as $E_{F,n}$ approaches E_c, Eq. 4.6 must be solved numerically to yield $E_{F,n}(T)$.

To gain insight into current conduction and the voltage distribution between the active layers of the device, we fit the dark $J-V$ as a function of T using (see Eq. 2.9):

$$J = J_{s1,T}\left(exp\left(\frac{qV_a - \Delta E_{F,p}}{nk_B T}\right) - 1\right). \tag{4.7}$$

Here we have included the R_S of ITO. For recombination of electrons in a uniform density of electron trap DOS at the ZnO surface [47, 48] and a trapped hole in an exponential DOS in CBP HOMO, we can define the n as n_O in Eq. 2.7. Further, we can define the activation energy of $J_{s1,T}$ as α_O in Eq. 2.7, and add $E_a - \Delta E_t$ term to account for activation energy of the carrier recombination rate and the width of the uniform trap DOS in the ZnO E_g. In writing Eq. 4.7, we have assumed that the diode current is governed by the product of the thermally activated carrier recombination rate and temperature and voltage dependent electron and hole densities at the OI-HJ. Then the temperature dependence of $J_{s1,T}$ and n provide insight into the recombination

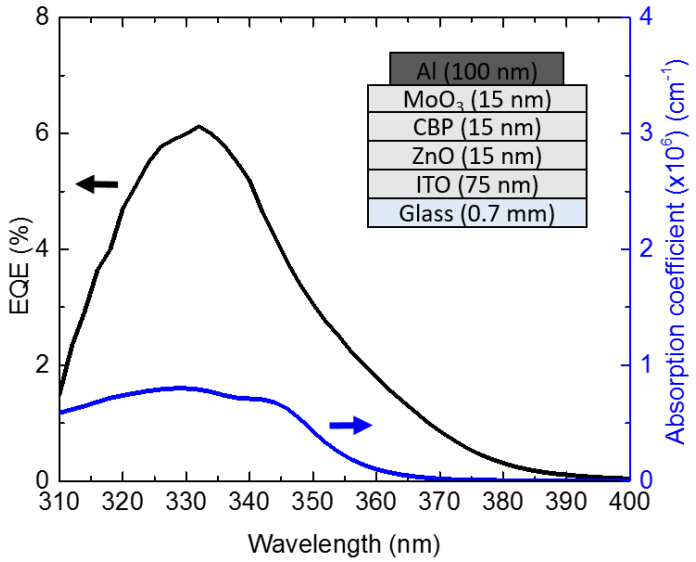

Figure 4.13: *EQE* of a ZnO/CBP OI-HJ device (left axis), and the absorption coefficient of CBP (right axis) grown on glass (0.7 mm). Inset: Device structure used in this study. Figure reproduced from Ref. [49].

mechanisms and voltage distribution across the device.

4.2.2 Experimental methods

The device structure shown in Fig. 4.13 inset, comprises ITO (75 nm)/ZnO (15 nm)/CBP (15 nm)/MoO_3 (15 nm)/Al (100 nm) grown on a 0.7 mm thick glass substrate. Prior to growth, the substrate pre-coated with a 70 nm thick film of ITO and patterned into 2 mm wide stripes (Luminescence Technology Corp.), is cleaned as described in §4.1.2 for the TiO_2 device. The ZnO film is grown by sputtering a ZnO target at 0.25 Å/s with RF power (175 W) and 1 sccm O_2 flow while maintaining the chamber pressure at 2.5 mTorr. The CBP (Luminescence Technology Corp.), MoO_3, and Al layers are deposited as described in §4.1.2 for the TiO_2 device. The Al cathode is deposited perpendicular to the ITO stripes through a shadow mask with 1 mm wide openings to define a 2 mm^2 device area.

The *EQE* measurements employ a monochromated (spectral resolution of 10 nm) Xe lamp with the measurement method described in §4.1.2. For temperature dependent EL

measurements, the device is loaded into a closed-cycle He cryostat. During measurement the cryostat is maintained at $< 1\text{x}10^{-5}$ Torr to prevent degradation by exposure to oxygen or water. The temperature is maintained using a thermally controlled stage heater, allowing 30 min for thermal stabilization between each measurement. The $J-V$ is measured to ensure the device is not degraded and to determine the EL measurement paramters. The EL spectrum is obtained by applying a 20 Hz square pulse of 1 ms pulse width, and the luminance is collected at normal incidence using a fiber-coupled monochromator (Princeton Instruments SP-2300i) equipped with a Si CCD detector array (PIXIS:400). The spectrum is corrected for the wavelength response of the setup using a tungsten halogen lamp. Each EL spectrum is obtained with a 15 s integration time for every 100 nm wavelength increment, yielding a total integration time of 1.5 min per spectra. The EL spectral lifetime is measured using a streak camera (Hamamatsu C4334) with a 40 ps time resolution. For temperature dependent PL measurements, a similar procedure is followed with the exception that the ZnO/CBP bilayer is grown on Si, and the CBP film thickness is only 50 Å to limit bulk emission. The sample is pumped at $\lambda = 325$ nm using a 15 mW/cm^2 He-Cd laser.

4.2.3 Results

The *EQE* at room temperature along with the CBP absorption spectrum are shown in Fig. 4.13. The *EQE* has a maximum at $\lambda = 332$ nm that corresponds to the peak in CBP absorption. The EL spectra obtained while driving the device at 100 mA/cm^2 as a function of T is shown in Fig. 4.14(a). The spectra exhibit a rigidochromic blue shift as the temperature is reduced from 1.65 ± 0.01 eV at 300 K to 2.05 ± 0.01 eV at 30 K, with a temperature independent FWHM of $\sigma = 300 \pm 10$ meV.

The peak energies of the spectra extracted by fitting to a Gaussian function are plotted in Fig. 4.14(b). The hypsochromic shift with decreasing temperature is linear above $T = 100$ K, and then saturates at 2.05 eV as temperature is further reduced. At

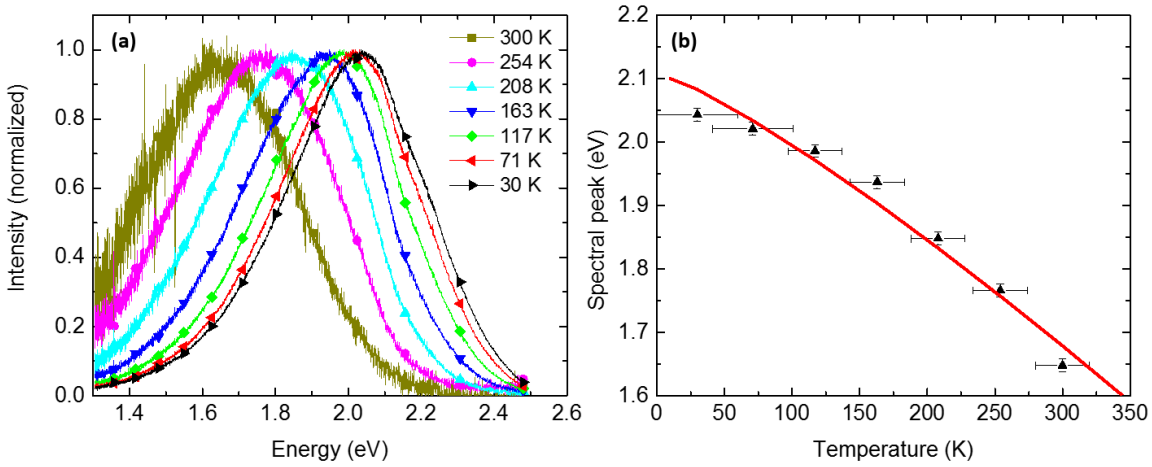

Figure 4.14: (a) EL spectra of the ZnO/CBP OI-HJ device as a function of T. (b) Peak energy of the EL spectrum vs. temperature obtained by fitting the spectrum to a Gaussian with a FWHM of 300 ± 10 meV. Fit to the spectral peak energy (solid line) yields an electron density at the HJ of $n_{HJ} = 10^{14} - 10^{12}$ cm^{-3}. Figure reproduced from Ref. [49].

300 K, the spectral peak energy increases linearly with V_a, as shown in Fig. 4.15. At $T = 30$ K, for $V_a < 3$ V , the peak energies shift more rapidly with temperature than at higher voltages where they exhibit a weak linear relationship similar to the data at $T = 300$ K. No emission is observed from either CBP or ZnO below $V_a = 4$ V. The HCTE$_{\mathrm{T}}$ lifetime is < 100 ns, which is confirmed by EL lifetime measurement, which is limited by the RC time constant of the device. The PL of the OI-HJ bilayer sample at $T > 25$ K shows bulk emission from only ZnO and CBP.

The forward biased $J - V$ characteristics vs. T are shown in Fig. 4.16(a). At all temperatures, three distinct exponential regions are observed. At 300 K and 30 K (i) Region 1 extends up to approximately 10^{-2} mA/cm^2, (ii) Region 2 from 10^{-2} mA/cm^2 to 10^2 mA/cm^2, and (iii) Region 3 at all higher currents shown. In Region 3, the current is limited by series resistance. As the temperature is reduced from 300 K, the current decreases and the three regions occur at higher voltages and over a larger voltage ranges.

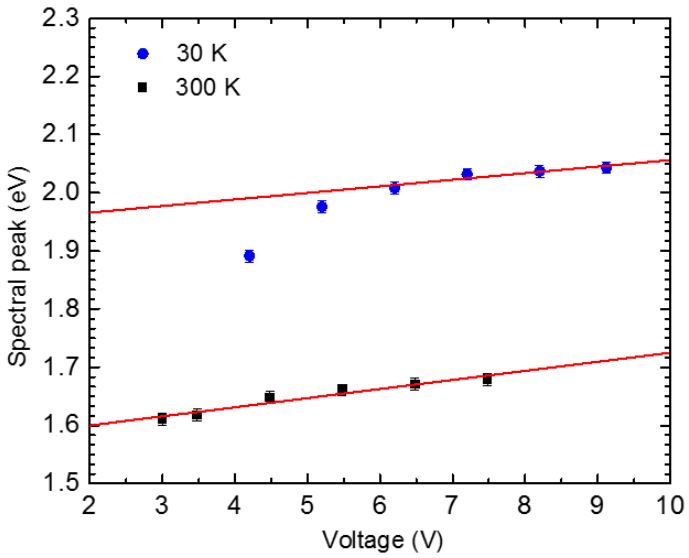

Figure 4.15: Peak energy of the EL spectrum as a function of the V_a at $T = 300$ (squares), 30 K (circles). The FWHM remains constant with V_a. Fits to the data (solid lines) yield the fraction of V_a dropped across ZnO under non-equilibrium conditions, giving $\Delta\delta_I = 0.016 \pm 0.003$ eV/V at 300 K and $\Delta\delta_I = 0.012 \pm 0.005$ eV/V at 30 K. Figure adapted from Ref. [49].

4.2.4 Discussion

The *EQE* of the device is orders of magnitude higher than the photoconductivity of typical organic semiconductor thin films [19], indicating that CBP quantum yield results from excitons diffusing to the OI-HJ and forming HCTEs before dissociating into free carriers. However, no HCTE PL is observed from the OI-HJ bilayer film. Furthermore, no ZnO or CBP EL emission is observed, indicating that radiative recombination of injected charges occurs only at the OI-HJ via HCTEs. The FWHM of the EL spectrum is temperature independent, and its peak energy at 300 K of 1.65 ± 0.01 eV is significantly lower than the predicted energy of $\Delta E_{OI} = 2.1 \pm 0.1$ eV.

To reconcile these disparate observations, we hypothesize the existence of two distinct states: HCTE_F and HCTE_T. The HCTE_F is a precursor to CBP exciton dissociation and comprise of delocalized electrons in ZnO bound to comparatively localized hole polarons in the CBP HOMO. The trapped HCTEs observed by EL are due to localized electrons at the ZnO surface that are populated by electrical injection and that sub-

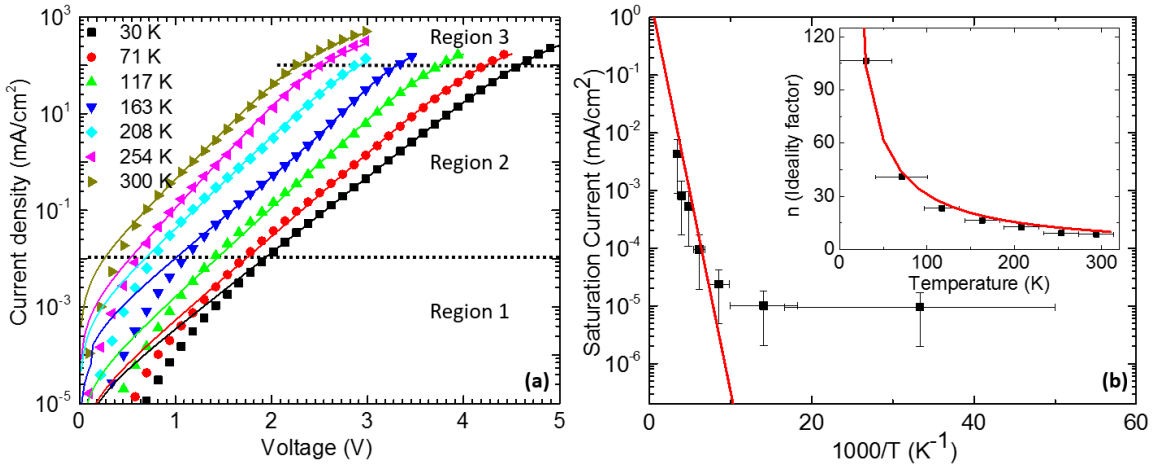

Figure 4.16: (a) $J-V$ characteristics in dark and fits at several different temperatures for a ZnO/CBP OI-HJ device. Data are shown by symbols and fits by lines. The fit parameters are summarized in Table 4.2. The dashed line indicates the current ($\sim$ 100 mA/cm^2) at which the EL data were obtained. Three distinct exponential regions are observed: (i) Region 1 extends to 10^{-2} A/cm^2; (ii) Region 2 from 10^{-2} A/cm^2 10^2 A/cm^2; and (iii) Region 3 is at higher currents. As the temperature is lowered, the three regions occur at higher voltages and over a larger voltage range. (b) Saturation current (J_{S1}) and ideality factor (n) vs. T (inset) obtained via fits to the $J-V$ characteristics. Fit to the saturation current and ideality factor (solid lines) are also shown. The fitting parameters are summarized in Table 4.3. The fits yield $\delta_I \approx 0$, which is expected due to high electron mobility and large carrier density in ZnO compared to the mobility of holes in CBP. Figure reproduced from Ref. [49].

sequently recombine with hole polarons in the CBP HOMO. Electron trapping likely occurs at surface defects due to Zn interstitials and oxygen vacancies whose energies are reported to lie $0.2 - 0.8$ eV below the ZnO conduction band edge [46]. We note that the EL spectra peak position, and its width and intensity, is dependent on ZnO processing conditions. As noted above, that spectral peak dependence on voltage and temperature are not found in organic HJ spectra. These observations support the conclusion that ZnO surface trap states dominate the behavior of the EL spectra peak at this OI-HJ.

The energy of the HCTE_T state is $\Delta E_{OI} - E_{F,n}$ where $E_{F,n}$ is the location of the occupied trap with respect to the ZnO conduction band and is determined by the Fermi level in ZnO. This accounts, therefore, for the shift in EL spectrum with T. Also in Fig. 4.10, we have taken the spectral width of HCTE_T be the trap states near the Fermi level since they are expected to have the highest radiative rate since non-radiative decay rate generally increases with decreasing E_g. This is not strictly correct, as the spectral width is a convolution of both the ground and excited states, but nevertheless is a reasonable approximation of the filled trap distribution.

The HCTE_T state is not observed by PL due to the additional kinetic energy, ΔE_{cL}, available during HCTE formation via CBP excitons. As a result, the electron in most cases does not thermalize into a trap state and remains relatively delocalized in ZnO, forming a HCTE_F that dissociates prior to recombination. Further, the states that do recombine are most likely rapidly thermalize non-radiatively due to the high density of trap states at the interface.

To confirm the existence of HCTE_T, we fit the change in EL peak energy vs. T to changes in the ZnO Fermi level using Eq. 4.6, with the result shown by the solid line in Fig. 4.14(b). Here we have neglected the V_a dependence of the spectra peak shift, which is a minor effect at high current densities (Fig. 4.15). The electon effective mass $m_{e,I} = 0.22m_0$ is used for the fit [38], and the change in E_c with temperature is estimated to be half of the ZnO band gap change as determined by its Varshni parameters [57]

to yield a carrier density of $n_{HJ} = 10^{13}$ $(10^{12} - 10^{14})$ cm$^{-3.}$ The range of n_{HJ} results from errors in the fitting parameter, which is magnified by the exponential relationship between $n_{HJ}$and $E_{F,n}$ in Eq. 4.6. Under high forward bias, the HCTE$_{\mathrm{T}}$ peak energy has a slope of 0.016 ± 0.003 eV/V and 0.012 ± 0.005 eV/V at 300 K and 30 K, respectively, shown by the solid lines in Fig. 4.15. This indicates that only $2-3$% of the incremental applied voltage is dropped across ZnO, which is reasonable considering the high carrier density in ZnO and the asymmetry in carrier mobilities of the two materials. Parameters obtained from the forward biased $J-V$ characteristics confirm the expected low voltage drop across ZnO at high injection. This is consistent with the relatively high electron mobility $\mu > 10$ cm^2/(Vs) at T > 25 K for sputtered ZnO thin films compared to CBP. Then, the voltage drop across the inorganic is $V_I = JW_I/(qn\mu_I)$ where n is the free carrier density. At $J = 100$ mA/cm^2, $W_I = 15$ nm and $n = 10^{14}$ cm^{-3}, this gives $V_I < 10^{-3}$ V.

In Fig. 4.15, we see that at very low voltages (i.e. low injection) at 30 K the EL spectra peak shift is larger than expected from the trends at higher voltages. We explain this using Eq. 4.5, where $\Delta\delta_I = 0.08 \pm 0.01$, which is similar to slope of the peak energy vs. low voltage data at 30 K. This change in voltage across the inorganic is due to carrier freeze out at the lowest temperature measured [38].

In a recent observation of EL from HCTE-mediated recombination at sol-gel ZnO/N,N'-bis(naphthalen-1-yl)-N,N'-bis(phenyl)benzidine (NPD) OI-HJ by Piersimoni, *et al.* [44] attribute the large energy difference of ~ 0.9 eV between the HCTE EL and absorption to vibrational relaxation of the HCTE following generation (see Fig. 1.15). Further, they attribute the broad spectra to inhomogeneous broadening due to tail states. In another reported observation at $Zn_{1-x}Mg_xO$/P3HT OI-HJ Eyer *et al.* [43] observe a broad EL spectrum and a difference of ~ 0.3 eV between the EL emission peak and ΔE_{OI}. They observe no temperature dependence of the spectral peak and only a weak temperature dependence of the spectral FWHM. Further, they attribute the shift in EL peak energy over a relatively small voltage range to an increase in the slope of the HCTE potential

perpendicular to the heterointerface and a resulting increase in electron energy level (i.e. quantum confined Stark effect).

In contrast to these observations, we propose that the EL spectra result from trapped HCTEs whose peak energy depends strongly on temperature and voltage. Further, we quantitatively confirm that the peak energy shift results from changes in Fermi level in the inorganic semiconductor. At 30 K, the trapped HCTE energy is 2.05 ± 0.01 eV, close to that predicted by theory. Our quantum mechanical modeling also suggests that the EL is observed due to the high oscillator strengths and binding energies of $^1\text{HCTE}_\text{T}$ and the absence of emission from $^1\text{HCTE}_\text{F}$ results from its comparatively low oscillator strengths.

$J-V$ characteristics: ZnO/CBP junction

We caution that $J-V$ fits are model dependent. Hence, while they provide information about the nature of the dark current generation processes, more detailed experiments must be carried out to verify our conclusions. For the purposes of this study, the $J-V$ characteristics are nevertheless useful for confirming the Fermi level position vs. V_a and T inferred from the observed spectral shifts. The $J_{s1,T}$ and n obtained from fits to the $J-V$ characteristics in Region 2 using Eq. 4.7 shown as solid lines in Fig. 4.16(a) are plotted in Fig. 4.16(b). The $J-V$ characteristics have ideality factors $n > 2$, suggesting recombination via trapped HCTEs [58]. The $J_{s1,T}$ and n are then fitted using parameters $\phi_I = 0.5$ eV and $\phi_O = 0.2$. Values obtained from the fits are summarized in Table 4.3 and result in the solid lines in Fig. 4.16(b). Further, the fits yield $\delta_I \approx 0$ in Region 2 which confirms the expected low voltage drop across ZnO due to its high electron mobility and carrier density as compared to the hole mobility in CBP. The saturation current, $J_{s1,T}$, does not follow the expected Arrhenius dependence below 70 K because of the assumption of constant, δ_I vs. T. This approximation becomes invalid when carrier freeze out occurs in ZnO, resulting in an increase in voltage dropped across

Table 4.3: Fitting parameters for ZnO/CBP $J-V$ characteristics

Parameter	Value
$T_{t,O}$	3100 ± 700 K
$J_{s1\infty}$	1.0 ± 0.5 A/cm^2
$E_a - \Delta E_t$	0.5 ± 0.1 eV
R_s	1.6 ± 0.2 Ω cm^2

the ZnO layer [38].

4.3 GaN/(In)GaN/DBP or CBP OI-HJs

To gain further insight into the HCTE state, in this work we explore exciton dynamics at an unusual hybrid QW where a relatively narrow energy gap InGaN layer is bounded on one side by GaN and on the other by either of the organic semiconductors, DBP or CBP. The energetics of the HCTE are tuned by the degree of quantum confinement determined by the energy barriers on either side of the InGaN layer and the well thickness. Similar to ZnO, nitride-based semiconductors are suitable for studying HCTEs [59] due to their low dielectric constant [60] relative to other III-V compound semiconductors, ensuring a high E_B for the state. Furthermore, nitride-based semiconductor composition can be modified to absorb in the ultraviolet, ensuring that the photoresponse of a visible-light-absorbing organic semiconductor can be spectrally resolved. Similar to ZnO, the GaN family of semiconductors exhibits rich defect phenomena due to lattice mismatch with the sapphire substrate [61].

We calculate a 10 meV binding energy for the unbound, or HCTE_F at the GaN/DBP heterointerface, which increases to 165 meV when bound in a GaN/$\text{In}_{0.21}\text{Ga}_{0.79}$N/DBP QW HCTE_QW. Voltage and QW In-concentration-dependent *EQE* measurements confirm the existence of a bound HCTE_QW, whose dissociation efficiency is shown to be determined by Poole-Frenkel emission. Combining spectrally resolved PL quenching (SR-PLQ) [62, 63] and *EQE* measurements of GaN/DBP OI-HJs, we find 14 ±3% of the organic excitons that diffuse to the heterointerface form HCTEs that subsequently

dissociate to contribute to the junction photocurrent.

Further, we investigate PL from $HCTE_{QW}$ in GaN/InGaN/CBP QW structures. We observed no PL at temperatures as low as $T = 10$ K, whereas EL from $HCTE_T$ is observed from $T = 294$ K to $T = 10$ K. This suggests that charge recombination at the OI-HJ occurs via electron trap states at the nitride surface on a time scale much shorter than the $HCTE_{QW}$ radiative recombination time. To our knowledge this is the first report of exciton confinement within a hybrid OI QW.

4.3.1 Theory

The proposed energy level diagrams for the QW devices based on vacuum level alignment of the semiconductor energy levels and experimental offsets reported for nitride semiconductor systems [64] are shown in Fig. 4.17. We use DBP as the organic semiconductor since its energy gap is less than that of $In_xGa_{1-x}N$ ($x = 0.11$ or 0.21) and GaN, ensuring that the voltage dependence of its photoresponse can be spectrally resolved from the inorganic photoresponse. In contrast, the wide energy gap of CBP maximizes ΔE_{OI}, as well as ΔE_{cL}. These energy barriers effectively confine the injected charges at the InGaN/CBP HJ, and allow for the possibility of observing the $HCTE_{QW}$ by PL or EL.

The nitride semiconductor surfaces are expected to efficiently dissociate organic excitons due to their large ΔE_{cL} for both CBP and DBP. The resulting $HCTE_{QW}$ PL and EL spectral peaks is expected at $\Delta E_{OI} - \Delta E_C + EE_1 - E_B$. Here, ΔE_C is the E_c offset between InGaN and GaN, and EE_1 is the first quantized electron state energy in the QW relative to the InGaN conduction band minimum energy. The spectral peak of $HCTE_T$ is determined by the $E_{F,n}$ at the inorganic surface as determined by the surface trap density of states as demonstrated for the ZnO/DBP OI-HJ(see §4.2.4).

The lowest energy eigenvalues (for the singlet states: $^1HCTE_F$ and $^1HCTE_{QW}$) obtained from simulations for the DBP based OI-HJs are shown in Fig. 3. The $E_B = 10$

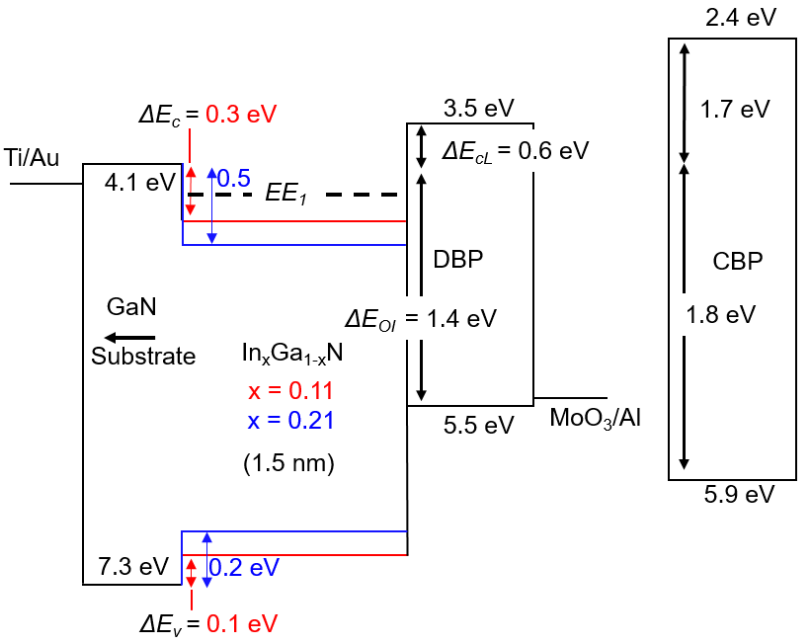

Figure 4.17: Energy level diagram of GaN/1.5 nm $In_xGa_{1-x}N$ ($x = 0.11$ or 0.21)/DBP OI QW devices at flat band determined by vacuum level alignment. Also shown are the energy levels of CBP. The ΔE_{OI} and ΔE_{cL} are the offsets at the OI-HJ. The ΔE_C and ΔE_V are the offset between the E_c and E_v of GaN and InGaN, respectively. The EE_1 is the energy of the first quantized electron state in the QW relative to the InGaN E_v. Figure reproduced from Ref. [65].

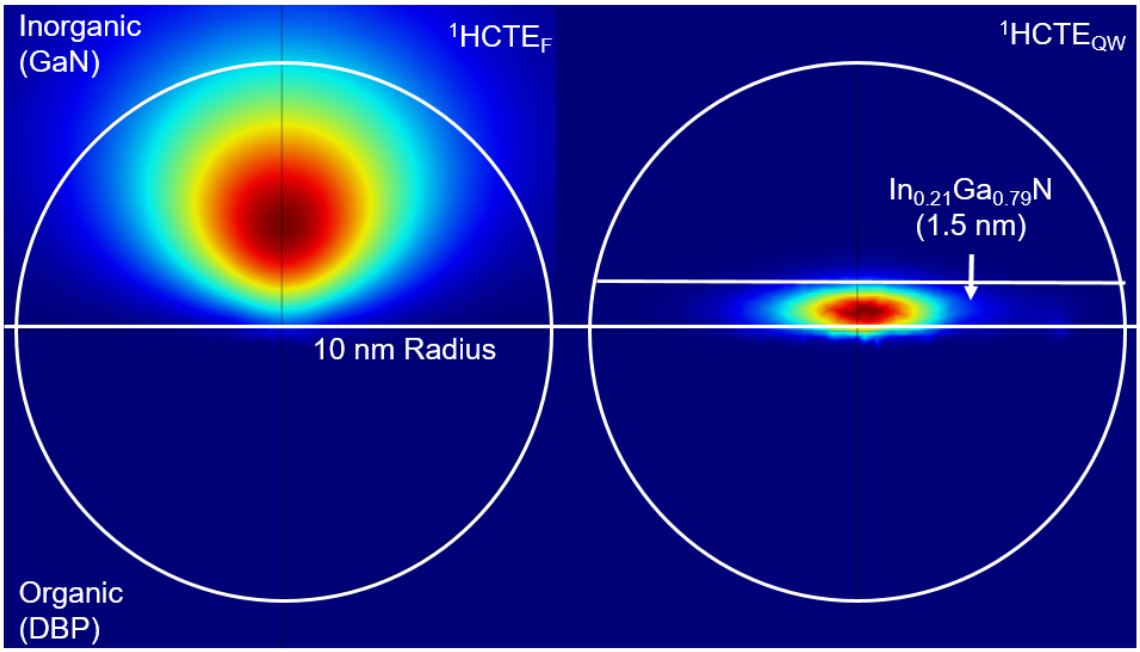

Figure 4.18: Spatial probability density of the lowest eigenvalue solution of the free and confined singlet HCTE (^{1}HCTE$_F$ and ^{1}HCTE$_{QW}$) at the GaN/DBP OI-HJ, and the GaN/1.5 nm In$_{0.21}$Ga$_{0.79}$N/DBP OI QW. The E_B of HCTE$_{QW}$ increases to 165 meV from 10 meV for HCTE$_F$, and the electron wave function penetration into the organic semiconductor increases from 0.1%, to 6.0%. Figure reproduced from Ref. [65].

meV for the $^1HCTE_F$ delocalized in GaN, and 127 meV for the $^1HCTE_{QW}$ confined in the $In_{0.11}Ga_{0.89}N$ well. When the In composition increases to $x = 0.21$, ΔE_c increases from 0.3 eV to 0.5 eV, resulting in an increase of the E_B to 165 meV. The electron wave function penetration into the organic semiconductor increases from 0.1% in $^1HCTE_F$ to 4.5% in $^1HCTE_{QW}$ in $In_{0.11}Ga_{0.89}N$, which gives rise to an increase in oscillator strength of the state. Increasing the In concentration from $x = 0.11$ to $x = 0.21$ increases the electron wave function penetration to 6.0%. When DBP is replaced with CBP, $\Delta\Delta E_{cL}$ increases from 0.6 eV to 1.7 eV. As a result, the $E_B = 97$ meV and 136 meV for $^1HCTE_{QW}$ in the $x = 0.11$ and $x = 0.21$ InGaN samples, respectively. The decrease in E_B for CBP as compared to DBP results from the decrease in electron wave function penetration into the organic semiconductor, which are 1.2% and 2% for $x = 0.11$ and $x = 0.21$ InGaN samples, respectively.

The $^1HCTE_{QW}$ spectral peak is expected to shift with voltage due to the voltage dependence of EE_1 and E_B. At high electric fields, the change in both E_B and EE_1 can be significant. For example, for the GaN/$In_{0.11}Ga_{0.89}N$/CBP CBP at 10^4 V/cm ($V_a = 0.1$ V), 10^5 V/cm ($V_a = 1$ V), 10^6 V/cm ($V_a = 10$ V), we calculate an increase of EE_1 of 3 meV, 24 meV, and 163 meV respectively, and an increase in E_B of 2 meV, 12 meV and 56 meV, respectively. The wave function penetration into the organic semiconductor side of the HJ remains unchanged at 1.5%. Spontaneous and piezoelectric polarizations existing within the nitride semiconductors will have an effect of similar magnitude on the properties of the $^1HCTE_{QW}$. In our measurements, however, they are screened by the externally applied field.

4.3.2 Experimental and theoretical methods

The epitaxial nitride layers are grown on sapphire substrates (University Wafer Inc.) in the (0001) orientation using metalorganic CVD with Si as the n-type dopant. Prior to growth, the substrates are diced into 1 cm^2 squares and cleaned and the organic

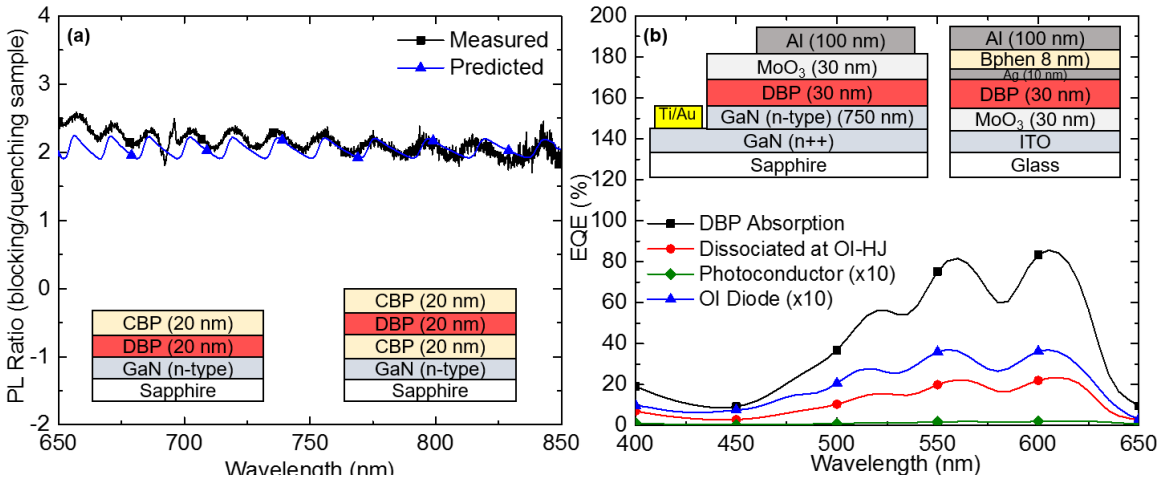

Figure 4.19: (a) Experimental and calculated spectrally resolved DBP PL intensity ratio vs. λ at a quenching and blocking interface (structures shown in inset). The match between the experimental and calculated ratios indicates that 100% of the excitons that reach the OI-HJ either dissociate or recombine. (b) *EQE* of a GaN/DBP OI-HJ and a DBP photoconductor biased at $V_a = +0.66$ V to match the built-in field in the DBP layer in the OI-HJ device at 0 V. Both device structures are shown in inset. The *EQE* spectrum is due to dissociation of DBP excitons. The percentage of light absorbed by the DBP layer and the percentage of photogenerated excitons in the layer that diffuse to the OI-HJ are also shown. Figure reproduced from Ref. [65].

semiconductors are purified as described in §4.1.2 for the TiO_2 device.

The structures used for SR-PLQ measurements shown as insets of Fig. 4.19(a) consist of sapphire/n++ GaN (4-5 μm, 1x10^{18} cm^{-3})/n-GaN (750 nm, 1x10^{16} cm^{-3}) and a combination of organic layers (DBP or CBP) that either block or quench DBP excitons. The OI diodes used for HCTE characterization consist of sapphire/n++ GaN (4-5 μm, 1x10^{18} cm^{-3})/cathode/inorganic layers/30 nm DBP/30 nm MoO_3/100 nm Al, as shown in Fig. 4.19(b), inset. For organic exciton dissociation efficiency characterization, the inorganic layer is n-GaN (750 nm, 1x10^{17} cm^{-3}), whereas for $HCTE_{QW}$ characterization, the inorganic layer is n-GaN (50 nm, 1x10^{16} cm^{-3})/undoped GaN (10 nm)/$In_xGa_{1-x}N$ (1.5 nm, undoped, $x = 0.11$ or 0.21). The DBP, MoO_3 and Al layers are deposited as described in §4.1.2 for the TiO_2 device. The Ti (5 nm)/Au (50 nm) cathode is deposited by e-beam evaporation at 0.5 Å/s as described in §4.1.2 for the InP device, on a region of

Table 4.4: Parameters used to calculate the HCTE properties at GaN/(In)GaN/DBP or CBP OI-HJ and OI QW system

Parameter	**Value**
$\boldsymbol{m_{e,O}/m_0}$	1.0
$\boldsymbol{m_{e,I}/m_0}$ $\boldsymbol{(x = 0, 0.11, 0.21)}$	0.2, 0.19, 0.18
$\boldsymbol{\epsilon_O}$	4
$\boldsymbol{\epsilon_I}$ $\boldsymbol{(x = 0, 0.11, 0.21)}$	8.9, 9.6, 10.2

the substrate where the n++ GaN is photolithographically exposed via plasma etching. Both the anode and cathode are deposited through shadow masks to define a 0.79 mm^2 device area. Similar structures are used for EL spectral measurements except that the DBP layer is replaced by a 20 nm thick CBP layer. For hard-contact patterned devices used for low temperature EL measurements, a 1 μm thick SiO_2 layer is deposited on the nitride surface using plasma-enhanced CVD, followed by photolithographically defining the device active area via etching in buffered HF.

The sample is illuminated for SR-PLQ measurements from the DBP side at $\lambda = 442$ nm using a 100 $\mu W/cm^2$ He-Cd laser at 65° from normal. A similar procedure is followed for the temperature dependent PL and EL characterization as described in §4.2.2, with the exception that the PL pump intensity is 15 mW/cm^2 at $\lambda = 325$ nm. Additionally, the EL spectral measurements use a two-stage, closed-cycle Janis He cryostat. The temperature is maintained with a thermally controlled stage heater, allowing 45 min for stabilization at each temperature. The *EQE* measurements use a current amplifier (Keithley Model 428) and are done using the setup described in §4.1.2. A parameter analyzer and AM 1.5G solar illuminator (100 mW/cm^2 illumination power) are used to obtain dark and light $J - V$ characteristics.

Quantum state calculations combine MD simulations the DBP and CBP deposited on the InGaN (0001) surface, DFT calculations of cationic organic molecular orbitals, and solutions to Schrödinger equation (see §3.2). The parameters used for simulation are listed in Table 4.4, and energies of the QW are reproduced in Fig. 4.17.

4.3.3 Results

The experimental and calculated SR-PLQ signal intensity ratio of DBP on a quenching and blocking GaN surface are shown in Fig. 4.19(a). In the quenching sample, DBP forms a type II HJ where excitons recombine or dissociate. The CBP layer inserted between GaN and DBP forms a type I HJ with DBP, and thus block DBP excitons. The Fabry-Pérot oscillations result from the index of refraction contrast between GaN and the adjacent layers. A DBP diffusion length of $L_D = 10 \pm 1$ nm [66] is found from the data using the method of Bergemann *et al.,* [62] assuming 100% quenching at the GaN interface. The match between the calculated and experimental ratios indicates that all the excitons generated in DBP that reach the GaN surface either dissociate or recombine.

The *EQE* spectrum of the OI-HJ device results solely from generation and dissociation of DBP excitons, since GaN is transparent at $\lambda = 365$ nm. We fabricated a DBP photoconductor to ensure that the *EQE* in the OI-HJ device is not due to DBP exciton dissociation in the bulk, a process which has recently been reported to yield $EQE > 10\%$ [67]. The DBP spectra of the GaN/DBP OI-HJ and DBP photoconductor are shown in Fig. 4.19(b). The photoconductor is forward biased to 0.66 V to match the built-in field in the DBP layer in the OI-HJ at 0 V.

Since the GaN layer thickness is larger than its depletion width, the built-in field across the organic layer is determined by using the procedure outlined in §2.2. The V_{bi} is estimated by the difference in the work function of the electrodes (1.1 V). The calculations indicate that 40% of the V_{bi} is dropped across the DBP. The field in the photoconductor is determined using the uniform field approximation, assuming $V_{bi} = 1$ V.

The peak *EQE*s at $\lambda = 615$ nm of the OI diode and photoconductor are $3.6 \pm 0.5\%$ and $0.22 \pm 0.02\%$, respectively. Optical modeling coupled with solutions to the exciton diffusion equation (see §1.6.4) are used to determine the fraction of excitons that reach the HJ (see Fig. 4.19(b)). The exciton diffusion equation is solved using $L_D = 10 \pm 2$

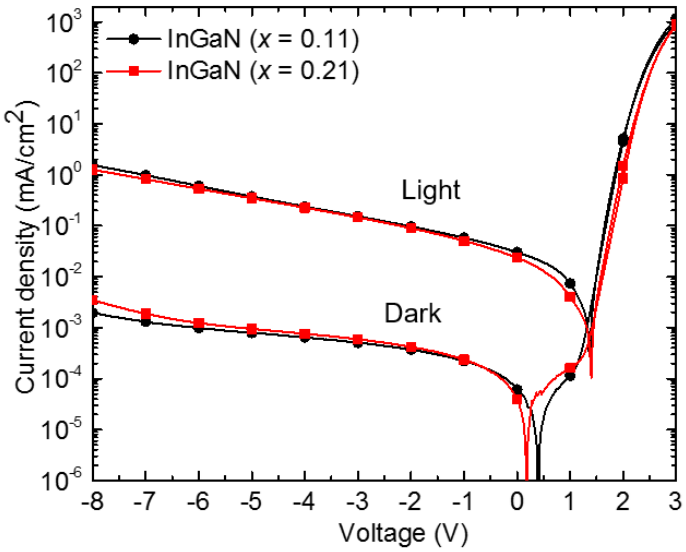

Figure 4.20: Dark and illuminated $J-V$ of GaN/1.5 nm $In_xGa_{1-x}N$ ($x = 0.11$ or 0.21)/DBP OI QW devices. The shift in $J-V$ to the right with decreasing ΔE_{OI} (see Fig. 4.17) matches the shift in $HCTE_T$ emission to higher energy (see Fig. 4.22). This indicates that the energy level alignment at the OI-HJ is determined by trap states at the heterointerface. Figure reproduced from Ref. [65].

nm, assuming that the quenching efficiencies at both the GaN and MoO_3 surfaces are 100%. This analysis shows that, at $\lambda = 615$ nm, the fraction of light absorbed in DBP and the fraction of excitons that diffuse to the OI-HJ are 79.5 ± 2.5% and 22.8 ± 2.5%, respectively.

The $J-V$ characteristics in the dark and under illumination for the GaN/InGaN/DBP OI QWs are shown in Fig. 4.20. The devices have $< 10^{-3}$ mA/cm^2 reverse bias leakage current up to an $V_a = 8$ V. Both devices show charging at low current due to traps and, as a result, do not reach $J = 0$ at $V_a = 0$ in the dark with a measurement integration time of 17 ms at each voltage. The $In_{0.21}Ga_{0.79}N$ QW device has a more abrupt turn-on under forward bias as compared to the $x = 0.11$ QW device. Both have similar ideality factors of $n = 3.2 \pm 0.1$. The $x = 0.21$ device also has a larger slope (between -2 V and +1 V) and lower photocurrent as compared to the x = 0.11 QW. The turn-on of the $x = 0.21$ device is slower than that of the $x = 0.11$ device.

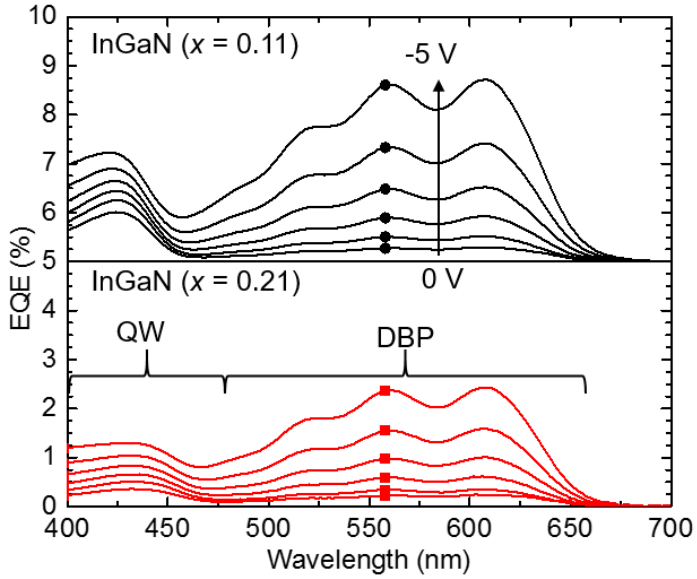

Figure 4.21: *EQE* of GaN/1.5 nm $In_xGa_{1-x}N$ ($x = 0.11$ or 0.21)/DBP QW devices from 0 V to -5 V in 1 V steps. The $x = 0.21$ device has lower *EQE* as compared to the device with $x = 0.11$ due to a larger conduction band offset of the InGaN with GaN, resulting in increased electron confinement in the QW. The InGaN spectral peaks are observed between $\lambda = 400 - 475$ nm, while the photoresponse between $\lambda = 475 - 650$ nm is due to DBP. Figure reproduced from Ref. [65].

Figure 4.21(b) shows the *EQE* vs. wavelength and voltage of the QW devices. The spectral peaks at $\lambda = 475$ nm are due to absorption by InGaN, and between $\lambda = 475$ nm and $\lambda = 675$ nm are solely due to DBP. The $x = 0.21$ device has a lower *EQE* from both the InGaN and DBP as compared to the $x = 0.11$ device, although the proportional increase with voltage is similar for both structures. This suggests that the increased In concentration and correspondingly increased ΔE_c increases electron confinement in the QW. The InGaN photoresponse peaks show minor shifts with voltage due a combination of screening of the built-in polarization fields and the QCSE [64], which confirm that DBP serves as an effective electron barrier at its interface with InGaN. The proportional increase in InGaN *EQE* with voltage is also lower than the increase in DBP photoresponse, suggesting an additional voltage dependent mechanism for DBP exciton dissociation.

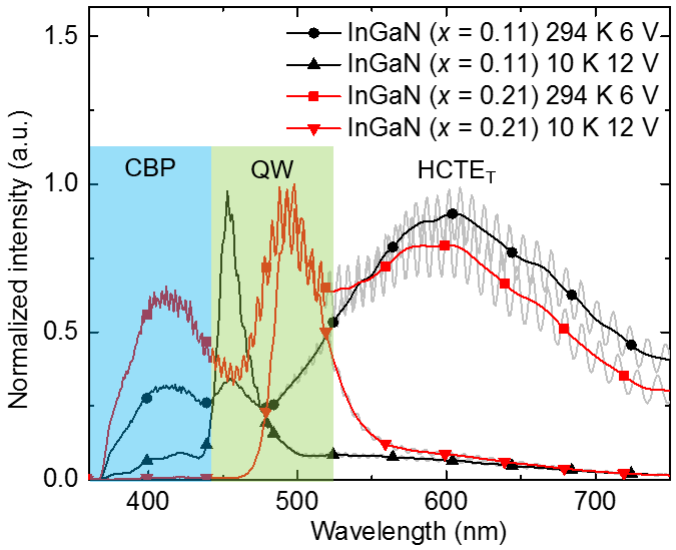

Figure 4.22: EL spectra of GaN/1.5 nm $In_xGa_{1-x}N$ ($x = 0.11$ or 0.21)/CBP OI QW devices at $T = 294$ K and $V_a = 6$ V, and at $T = 10$ K and $V_a = 12$ V. Spectrally resolved emission from bulk CBP and InGaN are observed at 600 nm (~ 2.1 eV) due to the trapped HCTEs, that are bound states between electrons in surface trap states on the nitride surface and hole polarons in the CBP. The HCTE spectra (shown in grey) are averaged to remove the Fabry-Pérot microcavity modes. The HCTE spectral shapes and position are independent of temperature at $T > 10$ K, and voltage. At $T = 10$ K the spectral peak has an abrupt blue shift. Figure reproduced from Ref. [65].

The EL spectra at $T = 294$ K and $V_a = 6$ V, and at $T = 10$ K and $V_a = 12$ V of the GaN/InGaN/CBP QW devices are shown in Fig. 4.22. In addition to the organic and inorganic semiconductor bulk emission peaks, an additional peak is observed at $\lambda = 600$ nm (2.1 eV) that is attributed to the InGaN/CBP HCTE. The emission intensities of the bulk semiconductors increases with increasing V_a and decreasing T. The intensity of the HCTE peak also increases with decreasing T. However, at a given V_a, the HCTE spectral intensity relative to the bulk emission decreases with T. The HCTE spectra remain broad and the spectral peak is independent of both voltage and temperature. At the lowest measurement temperature ($T = 10$ K), the HCTE spectral peaks shift to the blue by approximately 75 nm ($x = 0.11$) and 40 nm ($x = 0.21$). No HCTE PL is observed between $T = 294$ K and $T = 10$ K.

4.3.4 Discussion

The SR-PLQ data confirm that excitons from DBP and CBP that form type II HJs with nitride semiconductors either dissociate or recombine at the OI-HJ. The difference in *EQE* between the device with the OI-HJ and the photoconductor is 3.4 ± 0.5% at 615 nm. The additional *EQE* in the OI-HJ device is attributed to DBP exciton dissociation via $HCTE_F$. Further, since 22.8 ± 2.5% of the photogenerated excitons reach the heterointerface where 3.4 ± 0.5% successfully dissociate, we infer an exciton-to-charge conversion efficiency of 14 ± 3%. This suggests a high recombination rate of either the HCTE or its excitonic precursor at the OI-HJ.

To understand the effects of the $HCTE_{QW}$ binding energy on its dissociation, we normalize the *EQE* due to DBP ($\lambda = 615$ nm) exciton dissociation at a V_a to the relative change in InGaN QW *EQE* at that voltage from its value at 0 V. This factors out the change in charge collection through the DBP layer and emission over ΔE_c due to the applied field. Excitons generated in the InGaN layer dissociate in the QW because their binding energy is lower than the $k_B T$ at RT. We then subtract the contribution due to DBP photoconductivity determined by biasing the photoconductor to match the field in the DBP layer in the QW. The electric field on the QW side of the OI-HJ is determined using the uniform field approximation.

The increase in DBP *EQE* vs. the F in the QW is shown in Fig. 4.23. The observed voltage dependence is a result of the field-dependent dissociation of $HCTE_{QW}$ via Poole-Frenkel emission, which follows Eq. 3.7, where β is the linear slope when dissociation yield is plotted as a function of $F^{1/2}$. It accounts for the screening due to the dielectric constant of the InGaN given in Table 4.4. The data are fit using Eq. 3.7, with slopes $\beta = 8.5 \pm 0.2\text{x}10^{-4}$ $(\text{m/V})^{1/2}$ for $x = 0.11$, and $1.1 \pm 0.2\text{x}10^{-3}$ $(\text{m/V})^{1/2}$ for $x = 0.21$ QW, which are both similar to the predicted $\beta = 9.5\text{x}10^{-4}$ $(\text{m/V})^{1/2}$. The change in intercept at $F = 0$ gives a difference in binding energies of the $HCTE_{QW}$ between the two In composition devices of $\Delta E_B = 42 \pm 12$ meV, that matches the $\Delta E_B = 38$ meV

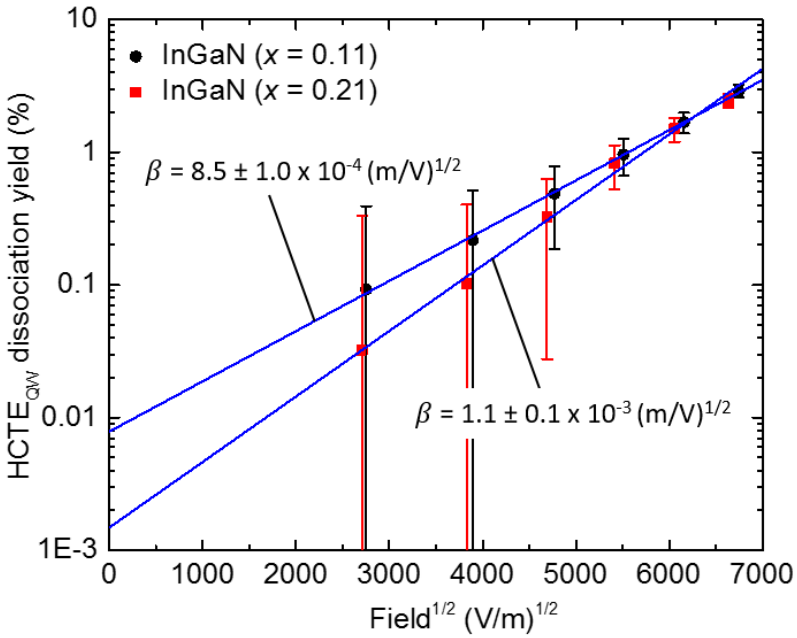

Figure 4.23: Voltage dependence of $HCTE_{QW}$ dissociation yield in GaN/1.5 nm $In_xGa_{1-x}N$ ($x = 0.11$ or 0.21)/DBP OI QW devices vs. F in the QW. The exciton dissociation efficiency is described by Poole-Frenkel emission (lines show fits to the data). The fits give $\beta = 8.5 \pm 0.2\text{x}10^{-4}$ $(\text{m/V})^{1/2}$ ($x = 0.11$) and $1.1 \pm 0.2\text{x}10^{-3}$ $(\text{m/V})^{1/2}$ ($x = 0.21$). The change in $HCTE_{QW}$ E_B for the two In compositions, $\Delta E_B = 42 \pm 12$ meV, determined from the change in the intercept at $F = 0$ matches the calculated $\Delta E_B = 38$ meV. Figure reproduced from Ref. [65].

calculated due to the change in ΔE_c.

The observation of the bound electron in the $HCTE_{QW}$, the high recombination rate of the HCTE at the OI-HJ and the predicted electron wave function penetration into the organic side of the OI-HJ suggests that $HCTE_{QW}$ should be observable by both PL and EL. However, no $HCTE_{QW}$ PL is observed in the GaN/InGaN/CBP QW samples, indicating a high non-radiative recombination rate of the state. In contrast, broad and voltage independent HCTE EL is observed from the GaN/InGaN/CBP CBP. To confirm if the HCTE emission spectrum is due to recombination at the OI-HJ, we replace CBP with NPD and observe that the HCTE spectral peak red shifts to $\lambda = 675$ nm (1.8 eV), in quantitative agreement with the shallower HOMO of NPD (5.5 eV). Further, at higher V_a, the inorganic and organic semiconductor emission intensities increase while that of

the HCTE decreases due to charge emission over the barriers at the OI-HJ.

The HCTE EL spectral peak is likely due to $HCTE_T$ since it does not shift with V_a, and has an abrupt blue shift at $T = 10$ K. The blue shift results from carrier freeze-out that pins the $E_{F,n}$ near to the band edge [68]. The voltage independence of the spectral peak suggests that a large density of trap states are concentrated close to the InGaN conduction band, pinning $E_{F,n}$ at the trap energy. The trap states are likely generated during CVD processing of SiO_2 on the nitride surface, which is consistent with reports of the formation of trap states during oxide deposition [69, 70]. The behavior of the dark $J-V$ further confirms that a high density of trapped charge carriers with discharge time constant $>$ 17 ms (the measurement sample time) exist at the OI-HJ. Further, the shift in $J-V$ turn-on to the right with decreasing ΔE_{OI} (see Fig. 4.17) matches the shift in $HCTE_T$ emission to higher energy (see Fig. 4.22), and is opposite of the trend predicted by the $J-V$ theory (see activation energy of pre-factor in Eq. 2.6). This indicates that the energy level alignment at the OI-HJ has in fact increased and is determined by the high density of trap states at the heterointerface. Further, the HCTE EL spectral peak at 2.1 eV is higher than the 1.7 eV predicted for $HCTE_{QW}$, implicating interface states in determining the OI-HJ alignment. From these observations, we conclude that the EL spectra from the GaN/InGaN/CBP QWs are due to transitions from $HCTE_T$ to the ground state. The high non-radiative recombination rate of the $HCTE_{QW}$ results from non-radiative recombination by rapid phonon-assisted thermalization through the midgap states on time scales faster than the radiative recombination rate. This is further confirmed by the lack of PL from the $HCTE_{QW}$.

Assuming the HCTE or exciton quenching rates at the GaN and (In)GaN surfaces are similar, we can estimate the minimum surface recombination site density. Since 86% of the excitons that reach the OI-HJ recombine, and the $HCTE_F$ radius is $\sim$ 10 nm (see Fig. 4.18), and noting that the state is unlikely to diffuse along the interface before dissociation due to its low binding energy of 10 meV, we estimate a minimum surface

recombination site density of $3x10^{11}$ $cm^{-2.}$ This is lower than the interface trap density of $1x10^{12}$ cm^{-2} reported at GaN/oxide interfaces [69, 70]. Using chemical passivation, a six-fold reduction in surface recombination velocity has been reported [71]. Assuming all surface recombination sites are passivated, we expect a seven-fold increase in the dissociation yield of the $HCTE_{QW}$.

Bibliography

[1] B. O'Regan and M. Gratzel, "A low-cost, high-efficiency solar cell based on dye-sensitized colloidal TiO2 films," *Nature* **353**, 737 (1991).

[2] A. Hagfeldt, G. Boschloo, L. Sun, L. Kloo, and H. Pettersson, "Dye-sensitized solar cells," *Chem. Rev.* **110**, 6595 (2010).

[3] J. Boucle, P. Ravirajan, and J. Nelson, "Hybrid polymer-metal oxide thin films for photovoltaic applications," *J. Mater. Chem.* **17**, 3141 (2007).

[4] S.-S. Li and C.-W. Chen, "Polymer-metal-oxide hybrid solar cells," *J. Mater. Chem. A* **1**, 10574 (2013).

[5] M. Slootsky, X. Liu, V. M. Menon, and S. R. Forrest, "Room temperature Frenkel-Wannier-Mott hybridization of degenerate excitons in a strongly coupled microcavity," *Phys. Rev. Lett.* **112**, 076401 (2014).

[6] S. R. Forrest, M. L. Kaplan, and P. H. Schmidt, "Semiconductor analysis using organic-on-inorganic contact barriers. II. Application to InP-based compound semiconductors," *J. Appl. Phys.* **60**, 2406 (1986).

[7] S. R. Forrest, M. L. Kaplan, P. H. Schmidt, and J. V. Gates, "Evaluation of III-V semiconductor wafers using nondestructive organic-on-inorganic contact barriers," *J. Appl. Phys.* **57**, 2892 (1985).

[8] N. Li, K. Lee, C. K. Renshaw, X. Xiao, and S. R. Forrest, "Improved power conversion efficiency of InP solar cells using organic window layers," *Appl. Phys. Lett.* **98**, 053504 (2011).

[9] S. M. Sze and K. K. Ng, *Physics of semiconductor devices*, 3rd ed. (Wiley-Interscience, Hoboken, USA, 2006), 832 pp.

[10] N. Wang, J. D. Zimmerman, X. Tong, X. Xiao, J. Yu, and S. R. Forrest, "Snow cleaning of substrates increases yield of large-area organic photovoltaics," *Appl. Phys. Lett.* **101**, 133901 (2012).

[11] M. T. Greiner, M. G. Helander, W.-M. Tang, Z.-B. Wang, J. Qiu, and Z.-H. Lu, "Universal energy-level alignment of molecules on metal oxides," *Nat. Mater.* **11**, 76 (2012).

[12] A. Panda, C. K. Renshaw, A. Oskooi, K. Lee, and S. R. Forrest, "Excited state and charge dynamics of hybrid organic/inorganic heterojunctions. II. Experiment," *Phys. Rev. B* **90**, 045303 (2014).

[13] C. J. Tavares, J. Vieira, L. Rebouta, G. Hungerford, et al., "Reactive sputtering deposition of photocatalytic TiO2 thin films on glass substrates," *Materials Science and Engineering: B* Society of Vacuum Coaters 2nd Symposium on Smart Materials **138**, 139 (2007).

[14] B.-x. Zhao, J.-c. Zhou, and L.-y. Rong, "Microstructure and optical properties of TiO2 thin films deposited at different oxygen flow rates," *Trans. Nonferrous Met. Soc. China* **20**, 1429 (2010).

[15] G. J. Bauhuis, P. Mulder, E. J. Haverkamp, J. C. C. M. Huijben, and J. J. Schermer, "26.1% thin-film GaAs solar cell using epitaxial lift-off," *Sol. Energy Mater Sol. Cells* **93**, 1488 (2009).

[16] D. Knipp, R. A. Street, A. Volkel, and J. Ho, "Pentacene thin film transistors on inorganic dielectrics: morphology, structural properties, and electronic transport," *J. Appl. Phys.* **93**, 347 (2003).

[17] X. Xiao, J. D. Zimmerman, B. E. Lassiter, K. J. Bergemann, and S. R. Forrest, "A hybrid planar-mixed tetraphenyldibenzoperiflanthene/C70 photovoltaic cell," *Appl. Phys. Lett.* **102**, 073302 (2013).

[18] D.-J. Yun, J. Chung, C. Jung, H.-S. Han, et al., "Pentacene orientation on source/drain electrodes and its effect on charge carrier transport at pentacene/electrode interface, investigated using in situ ultraviolet photoemission spectroscopy and device characteristics," *J. Electrochem. Soc.* **160**, H436 (2013).

[19] C. K. Renshaw, J. D. Zimmerman, B. E. Lassiter, and S. R. Forrest, "Photoconductivity in donor-acceptor heterojunction organic photovoltaics," *Phys. Rev. B* **86**, 085324 (2012).

[20] A. Rao, B. J. Walker, B. Ehrler, K. P. Musselman, et al., "Resonant energy transfer of triplet excitons from pentacene to PbSe nanocrystals," *Nat. Mater.* **13**, 1033 (2014).

[21] H. Lim, H. Kwon, S. K. Kim, and J. W. Kim, "Delayed triplet-state formation through hybrid charge transfer exciton at copper phthalocyanine/GaAs heterojunction," *J. Phys. Chem. Lett.* **8**, 4763 (2017).

[22] S. P. Park, S. S. Kim, J. H. Kim, C. N. Whang, and S. Im, "Optical and luminescence characteristics of thermally evaporated pentacene films on Si," *Appl. Phys. Lett.* **80**, 2872 (2002).

[23] M. Stavola, D. L. Dexter, and R. S. Knox, "Electron-hole pair excitation in semiconductors via energy transfer from an external sensitizer," *Phys. Rev. B* **31**, 2277 (1985).

[24] H. Yang, T. J. Shin, M.-M. Ling, K. Cho, C. Y. Ryu, and Z. Bao, "Conducting AFM and 2D GIXD studies on pentacene thin films," *J. Am. Chem. Soc.* **127**, 11542 (2005).

[25] N. Koch, I. Salzmann, R. L. Johnson, J. Pflaum, R. Friedlein, and J. P. Rabe, "Molecular orientation dependent energy levels at interfaces with pentacene and pentacenequinone," *Organic Electronics* **7**, 537 (2006).

[26] V. Coropceanu, J. Cornil, D. A. da Silva Filho, Y. Olivier, R. Silbey, and J.-L. Bredas, "Charge transport in organic semiconductors," *Chem. Rev.* **107**, 926 (2007).

[27] A. D. Carlo, F. Piacenza, A. Bolognesi, B. Stadlober, and H. Maresch, "Influence of grain sizes on the mobility of organic thin-film transistors," *Appl. Phys. Lett.* **86**, 263501 (2005).

[28] B. P. Rand, J. Xue, S. Uchida, and S. R. Forrest, "Mixed donor-acceptor molecular heterojunctions for photovoltaic applications. I. Material properties," *J. Appl. Phys.* **98**, 124902 (2005).

[29] E. Hendry, F. Wang, J. Shan, T. F. Heinz, and M. Bonn, "Electron transport in TiO2 probed by THz time-domain spectroscopy," *Phys. Rev. B* **69**, 081101 (2004).

[30] E. Yagi, R. R. Hasiguti, and M. Aono, "Electronic conduction above 4 K of slightly reduced oxygen-deficient rutile TiO2-x," *Phys. Rev. B* **54**, 7945 (1996).

[31] O. V. Mikhnenko, F. Cordella, A. B. Sieval, J. C. Hummelen, P. W. M. Blom, and M. A. Loi, "Temperature dependence of exciton diffusion in conjugated polymers," *J. Phys. Chem. B* **112**, 11601 (2008).

[32] F. B. Dias, K. T. Kamtekar, T. Cazati, G. Williams, M. R. Bryce, and A. P. Monkman, "Exciton diffusion in polyfluorene copolymer thin films: kinetics, energy disorder and thermally assisted hopping," *ChemPhysChem* **10**, 2096 (2009).

[33] H. Cetin and E. Ayyildiz, "Temperature dependence of electrical parameters of the au/n-InP schottky barrier diodes," *Semicond. Sci. Technol.* **20**, 625 (2005).

[34] M. K. Hudait and S. B. Krupanidhi, "Doping dependence of the barrier height and ideality factor of Au/n-GaAs Schottky diodes at low temperatures," *Physica B* **307**, 125 (2001).

[35] J. Cornil, J. P. Calbert, and J. L. Bredas, "Electronic structure of the pentacene single crystal: relation to transport properties," *J. Am. Chem. Soc.* **123**, 1250 (2001).

[36] A. D. Carlo, F. Piacenza, A. Bolognesi, B. Stadlober, and H. Maresch, "Influence of grain sizes on the mobility of organic thin-film transistors," *Appl. Phys. Lett.* **86**, 263501 (2005).

[37] E. Hokelek and G. Y. Robinson, "A study of Schottky contacts on Indium Phosphide," *J. Appl. Phys.* **54**, 5199 (1983).

[38] A. Janotti and C. G. V. d. Walle, "Fundamentals of zinc oxide as a semiconductor," *Rep. Prog. Phys.* **72**, 126501 (2009).

[39] M. Vodenicharova and G. H. Jensen, "Photosensitization of ZnO single crystals by means of dyes," *J. Phys. Chem. Solids* **36**, 1241 (1975).

[40] C. Kavassalis and M. T. Spitler, "Photooxidation of thiacyanine dyes at zinc oxide single-crystal electrodes," *J. Phys. Chem.* **87**, 3166 (1983).

[41] C. Strothkamper, A. Bartelt, P. Sippel, T. Hannappel, R. Schutz, and R. Eichberger, "Delayed electron transfer through interface states in hybrid ZnO/organic-dye nanostructures," *J. Phys. Chem. C* **117**, 17901 (2013).

[42] Y. Vaynzof, A. A. Bakulin, S. Gelinas, and R. H. Friend, "Direct observation of photoinduced bound charge-pair states at an organic-inorganic semiconductor interface," *Phys. Rev. Lett.* **108**, 246605 (2012).

[43] M. Eyer, S. Sadofev, J. Puls, and S. Blumstengel, "Charge transfer excitons at ZnMgO/P3HT heterojunctions: relation to photovoltaic performance," *Appl. Phys. Lett.* **107**, 221602 (2015).

[44] F. Piersimoni, R. Schlesinger, J. Benduhn, D. Spoltore, et al., "Charge transfer absorption and emission at ZnO/organic interfaces," *J. Phys. Chem. Lett.* **6**, 500 (2015).

[45] G. Wu, Z. Li, X. Zhang, and G. Lu, "Charge separation and exciton dynamics at polymer/ZnO interface from first-principles simulations," *J. Phys. Chem. Lett.* **5**, 2649 (2014).

[46] A. A. Sokol, S. A. French, S. T. Bromley, C. R. A. Catlow, H. J. J. v. Dam, and P. Sherwood, "Point defects in ZnO," *Faraday Discuss.* **134**, 267 (2006).

[47] P. Winget, L. K. Schirra, D. Cornil, H. Li, et al., "Defect-driven interfacial electronic structures at an organic/metal-oxide semiconductor heterojunction," *Adv. Mater.* **26**, 4711 (2014).

[48] K. Lee, M. S. Oh, S.-J. Mun, K. H. Lee, et al., "Interfacial trap density-of-states in pentacene- and ZnO-based thin-film transistors measured via novel photo-excited charge-collection spectroscopy," *Adv. Mater.* **22**, 3260 (2010).

[49] A. Panda, K. Ding, X. Liu, and S. R. Forrest, "Free and trapped hybrid charge transfer excitons at a ZnO/small-molecule heterojunction," *Phys. Rev. B* **94**, 125429 (2016).

[50] C. Woll, "The chemistry and physics of zinc oxide surfaces," *Prog. Surf. Sci.* **82**, 55 (2007).

[51] M. Pope and C. E. Swenberg, *Electronic processes in organic crystals and polymers*, 2nd ed. (Oxford University Press, New York, 1999), 1328 pp.

[52] X. Liu, K. Ding, A. Panda, and S. R. Forrest, "Charge transfer states in dilute donor-acceptor blend organic heterojunctions," *ACS Nano* **10**, 7619 (2016).

[53] Y. Zhou, K. Tvingstedt, F. Zhang, C. Du, et al., "Observation of a charge transfer state in low-bandgap polymer/fullerene blend systems by photoluminescence and electroluminescence studies," *Adv. Funct. Mater.* **19**, 3293 (2009).

[54] N. Matsusue, S. Ikame, Y. Suzuki, and H. Naito, "Charge carrier transport in an emissive layer of green electrophosphorescent devices," *Appl. Phys. Lett.* **85**, 4046 (2004).

[55] A. Singh, S. Chaudhary, and D. K. Pandya, "On the temperature dependence of mobility in hydrogenated indium-doped ZnO thin films," *Acta Mater.* **77**, 125 (2014).

[56] A. Singh, S. Chaudhary, and D. K. Pandya, "High conductivity indium doped ZnO films by metal target reactive co-sputtering," *Acta Mater.* **111**, 1 (2016).

[57] V. A. Fonoberov, K. A. Alim, A. A. Balandin, F. Xiu, and J. Liu, "Photoluminescence investigation of the carrier recombination processes in ZnO quantum dots and nanocrystals," *Phys. Rev. B* **73**, 165317 (2006).

[58] R. A. Street, A. Krakaris, and S. R. Cowan, "Recombination through different types of localized states in organic solar cells," *Adv. Funct. Mater.* **22**, 4608 (2012).

[59] M. Slawinski, M. Weingarten, S. Axmann, F. Urbain, et al., "Characterization of charge injection and photovoltaic effects of hybrid inorganic-organic GaN/pentacene heterostructures," *Appl. Phys. Lett.* **103**, 153305 (2013).

[60] M. E. Levinshtein, S. L. Rumyantsev, and M. Shur, *Properties of advanced semiconductor materials: GaN, AlN, InN, BN, SiC, SiGe* (Wiley, New York, 2001).

[61] B. Gil, *Group III nitride semiconductor compounds: physics and applications* (Clarendon Press; Oxford University Press, Oxford; New York, 1998).

[62] K. J. Bergemann and S. R. Forrest, "Measurement of exciton diffusion lengths in optically thin organic films," *Appl. Phys. Lett.* **99**, 243303 (2011).

[63] R. R. Lunt, N. C. Giebink, A. A. Belak, J. B. Benziger, and S. R. Forrest, "Exciton diffusion lengths of organic semiconductor thin films measured by spectrally resolved photoluminescence quenching," *J. Appl. Phys.* **105**, 053711 (2009).

[64] S. L. Chuang, *Physics of optoelectronic devices* (Wiley, New York, 1995).

[65] A. Panda and S. R. Forrest, "Quantum confinement of hybrid charge transfer excitons in GaN/InGaN/organic semiconductor quantum wells," *Nano Lett.* **17**, 7853 (2017).

[66] M. Hirade and C. Adachi, "Small molecular organic photovoltaic cells with exciton blocking layer at anode interface for improved device performance," *Appl. Phys. Lett.* **99**, 153302 (2011).

[67] H. T. Chandran, T.-W. Ng, Y. Foo, H.-W. Li, et al., "Direct free carrier photogeneration in single layer and stacked organic photovoltaic devices," *Adv. Mater.* **29**, 1606909 (2017).

[68] H. Morkoc, *Handbook of nitride semiconductors and devices, materials properties, physics and growth* (John Wiley & Sons, July 30, 2009), 1324 pp.

[69] C. Ostermaier, H.-C. Lee, S.-Y. Hyun, S.-I. Ahn, et al., "Interface characterization of ALD deposited Al2O3 on GaN by CV method," *Phys. Stat. Sol. (c)* **5**, 1992 (2008).

[70] D. Gregusova, R. Stoklas, C. Mizue, Y. Hori, et al., "Trap states in AlGaN/GaN metal-oxide-semiconductor structures with Al2O3 prepared by atomic layer deposition," *J. Appl. Phys.* **107**, 106104 (2010).

[71] G. L. Martinez, M. R. Curiel, B. J. Skromme, and R. J. Molnar, "Surface recombination and sulfide passivation of GaN," *J. Electron. Mater.* **29**, 325 (2000).

CHAPTER V

Conclusion

The theoretical and experimental work contained in this thesis provides a starting point to understand excited state dynamics in organic-inorganic semiconductor heterojunctions (OI-HJs) based optoelectronic devices. By developing a quantitative description of current processes in OI material systems, a quantum mechanical model for the hybrid charge transfer exciton (HCTE), and demonstrating its applicability to multiple OI systems, we have opened the possibility of designing an exciting new class of hybrid materials. Further study of these materials is poised to reveal a new understanding of semiconductor physics that subsequently enables novel applications.

In this chapter, we provide a summary of the experimental and theoretical work described in this thesis. We present the key questions about OI systems that should be addressed to enable their application in next-generation optoelectronic devices. We discuss experimental paths forward to answering these questions and developing novel applications. The outlined experiments offer only a preliminary outlook into the rich set of questions and investigations possible for this nascent field.

5.1 Summary of the work

We presented theoretical models and experimental data elucidating exciton and charge dynamics at hybrid OI-HJs. While we limited our study to type II energy level alignment at the OI-HJ because of their widespread applicability to photovoltaics (PVs), light-emitting diodes (LEDs), and lasers, the conclusions are easily generalized to OI-HJs

with other band alignments. In developing the comprehensive current density vs. voltage ($J-V$) model, we proposed the dark and illuminated electrical characteristics of the OI-HJ based diodes are determined by the junction properties such as the energy level offset between the two materials, the magnitude and densities of states of the interface traps, and the properties of the HCTE. In the dark, recombination of injected electrons and holes occurs primarily at the OI-HJ through the HCTE. When illuminated, the HCTE also forms following the diffusion of a Frenkel-like exciton from the organic semiconductor to the heterointerface. Dissociation of the HCTE results in free carriers that are collected at the electrodes. Conversely, illumination of the inorganic semiconductor directly yields free charge. This results in minority carrier injection over the OI-HJ, where it can either recombine or be extracted by traversing through the organic layer. The low mobility of charge carrier in the organic plays a critical role in limiting current conduction through the diode.

The HCTE is composed of a electron in the inorganic and a hole polaron localized on an organic molecule. As a result, the HCTE has properties intermediate between a Frenkel and Wannier-Mott exciton. This newly identified quasi-particle is of central importance to governing excited state properties at the junction, such as exciton dissociation and charge recombination. Its properties are determined by the dielectric constants, charge carrier effective masses of the contacting materials, and the interface trap densities. We calculate the properties of three HCTE states: the free HCTE ($HCTE_F$), the trapped HCTE ($HCTE_T$), and the the quantum well (QW)-confined HCTE ($HCTE_{QW}$). Conceptually, the latter states result from a reduction in the dimensionality of electron delocalization on the inorganic side of the HJ. The $HCTE_F$ is the intermediate state to exciton dissociation. In this state, the electron is delocalized in 3D over multiple lattice sites. The state is expected to have a low binding energy and long radiative lifetime due to the small electron and hole wave function overlap. The $HCTE_T$ is the intermediate state to charge recombination at the OI-HJ. In this state, the electron is localized on a

trap site on the inorganic surface. The state is expected to have a large binding energy and much shorter radiative lifetime as compared to the $HCTE_F$. The $HCTE_{QW}$ is composed of an electron confined to a thin inorganic QW layer at the OI-HJ. The offsets of the QW conduction and valence bands with the neighboring organic and inorganic semiconductors determine the binding energy and the radiative lifetime of the state. Further, by applying a voltage to the OI-HJ, the absorption and emission energy, and radiative lifetime of the state can be tuned due to the quantum-confined Stark effect (QCSE). While the radiative lifetime of the HCTE is expected to range from ms to ns, in all cases it competes with non-radiative recombination due to rapid phonon assisted thermalization by the interface traps. As a result, observation and manipulation of the HCTE requires interfaces with low non-radiative rates.

The HCTE theory is used to quantitatively describe current density vs. voltage ($J-V$), external quantum efficiency (EQE), electroluminescence (EL), and photoluminescence (PL) characteristics of several OI-HJ based systems. While the experimental work in this thesis focused on studying simple bilayer OI-HJ structures to isolate their fundamental properties, the design of more sophisticated OI semiconductor systems is possible with the presented findings.

Data for wide band gap TiO_2/tetraphenyldibenzoperiflanthene (DBP) and moderate band gap InP/pentacene (PEN) OI-HJs were analyzed. In both cases, we found evidence that excitons generated in the organic thin films contribute to the photocurrent through generation of an HCTE. The effects of interface traps are markedly different in these two systems. There is little evidence that traps impact the temperature dependence of the formation or recombination of HCTEs for the wide band gap case; whereas, in the moderate band gap case, they dominate HCTE dynamics over a wide range of temperatures. Fits to the $J-V$ characteristics in the dark and under illumination over a wide temperature range provide further validation of our models. From the fits, we find the magnitude of the OI-HJ energy offsets and traps at the HJ determine

the recombination kinetics of injected and photogenerated carriers. Specifically, in the wide band gap case, we find the $J-V$ characteristics — both in the dark and under illumination — are determined by interface recombination. In the moderate band gap case, the dark $J-V$ characteristics are determined by thermionic emission into the InP bulk, while HJ recombination dominates under illumination. Furthermore, we find that space-charge effects arising from the low carrier mobility in the organic thin film reduce the fill factor as the temperature is lowered.

At the ZnO/4,4'-bis(N-carbazolyl)-1,1'-biphenyl (CBP) OI-HJ, we observe HCTE_F by EQE and HCTE_T by EL. The EL emission from HCTE_T recombination between localized electrons on the ZnO surface and hole polarons in CBP is found to be dependent on both temperature (T) and applied voltage (V_a), which is quantitatively explained by modeling Fermi level shifts within the ZnO. Exciton-to-charge conversion occurs via HCTE_F. Fits to the $J-V$ provide insight into the voltage distribution and Fermi levels in the layers.

In the GaN/DBP junction, we observed the HCTE_F by EQE, and at the (In)GaN/CBP junction we observe HCTE_T by EL. Further, we design a GaN/(In)GaN/DBP OI system and demonstrate the tunability of the optoelectronic properties of the HCTE by electron confinement within OI QW. The HCTE_QW binding energy increases with QW depth, making it stable at room temperature = 294 K (RT). The existence and properties of HCTE_QW and its confinement are inferred by modeling its electric-field-dependent dissociation using Poole-Frenkel emission. This work opens the possibility of systematic tuning of HCTE properties by confinement within QWs at OI-HJs.

5.2 Future outlook

There still remains an enormous gap in our understanding of the role of surface defects and material dimensionality in the control of excited state processes mediated by the HCTE in OI systems. This thesis has not considered the role of Förster resonance

energy transfer (FRET) in detail, which can also be play an important role in determining properties in OI material systems. For future work, we propose that the following questions be answered:

1. How can the density of interface traps at the OI-HJ be reduced to decrease the non-radiative decay of the HCTE, and to observe the radiative decay (i.e. photoluminescence (PL)) by a tunable state?

2. What are the kinetics of HCTE formation? Can its formation be controlled by changing the resonance between the energy of the electron in the QW and the organic semiconductor? Why is organic exciton dissociation generally observed in wide band gap semiconductors at RT, but not in narrow band gap semiconductors?

3. Can the optoelectronic properties of the HCTE, such as its binding energy and radiative rate, be systematically tuned over a wide range by controlling the dimensionality of the HJ or by placing a wide band gap barrier layer between the contacting heterogeneous materials?

4. Can the HCTE diffuse parallel to the OI-HJ? How efficiently can this diffusion process be controlled by application of an external voltage, magnetic field, or surface acoustic waves (SAWs)?

5. What is the triplet and singlet state splitting for the HCTE, and what is the intersystem crossing rate? How can we control the splitting?

6. What are the non-linear optical properties that result from resonance between the organic and inorganic excitons and the HCTE?

5.2.1 Observing radiative decay of HCTEs

An extensive amount of semiconductor literature is dedicated to the passivation of surface states. Unfortunately, none of the techniques result in perfect passivation

of the surface (except methyl-termination of Si (111) surface [1]). However, recently emerging work in III-V nanowires has demonstrated extremely low surface recombination velocities [2]. There are also reports of PL from the CT states at 2D transition metal dichalcogenide (TMD) HJs [3]. This makes these two semiconductor systems fertile testing grounds for observation of PL of the HCTE. As an added benefit, the 1D confinement of the electron in monolayer TMDs and nanowires increases the probability for observation of the state. Collodial quantum dots could be interesting for this purpose, since they offer 3D confinement. However, they are reported to have a high surface defect density. Nevertheless, $HCTE_T$ emission has been reported from CdSe nanocrystal/polymer OI-HJs [4, 5].

5.2.2 Exciton dissociation kinetics

The process of exciton dissociation is under intense debate in the field of organic photovoltaics (OPVs). Questions remain about whether exciton dissociation occurs through a hot charge transfer (CT) state, and the role of the additional energy from the HJ lowest unoccupied molecular orbital (LUMO) offset in the dissociation process is as yet poorly understood [6, 7]. Further, there are concerns that, since the singlet and triplet CT states are resonant (the large radius of the state results in a small exchange energy), the CT can transfer into a lower energy triplet state in the bulk of one of the contacting materials [8]. The OI QW system offers a tunable system where these questions can be systematically explored and answered.

The formation of an $HCTE_{QW}$ in the GaN/(In)GaN/DBP system suggests that hot exciton dissociation does not occur. However, this question can be explored further by tuning the In composition over a larger range to determine if there is a threshold at which the additional energy from LUMO offset can increase dissociation yield. Resonant triplet transfer has been demonstrated between colloidal quantum dots in a PbSe/PEN [9] and PbS/tetracene HJs [10]. Tuning the HCTE energy level in the QW to the triplet

energy and observing the effect on HCTE formation efficiency can shed further light on the process. Further, if the HCTE formation is found to be affected by the resonance condition, OI systems that efficiently capture triplets can be realized. This could be a potential path to triplet management that has been shown to extend the lifetime of blue organic light-emitting diodes (OLEDs) [11] and organic lasers [12].

5.2.3 Exciton-based transistors

The analogous quasi-particle to the HCTE in III-V semiconductors is the indirect exciton, an exciton where the electron and hole are confined to spatially separated layers. Its long lifetime and tunability with V_a [13] and SAWs [14] is already being explored for exciton-based transistors. In these transistors, the indirect exciton is generated by an incoming optical signal, and its subsequent diffusion along the HJ is controlled to perform logic operations on the signal. Afterward, the exciton can be allowed to recombine, regenerating the optical signal for on-chip communication. As a result, exciton-based transistors can offer significant power savings due to the low energy requirement for transmitting signals. The on-chip communication can also occur at faster speeds, overcoming the already-reached limitations of electronic transistors. However, the already realized exciton-based transistors realized for III-V semiconductor systems are only stable at lower than RT due to the high dielectric constant of the materials. The HCTE can potentially be used for this applications because it is predicted to be stable at RT in some material systems. While the low diffusivity of the HCTE along the interface due to the low diffusivity of polarons in organic semiconductors might limit the speed of operation, this deficiency could potentially be overcome by exploring the high polaron diffusivity in crystalline organic semiconductors.

5.2.4 OI superlattices

There has been significant work on predicting the non-linear optical properties of strongly-coupled OI systems [15]. Recent demonstrations of large Rabi splitting in ZnO/ 1,4,5,8-naphthalenetetracarboxylic dianhydride (NTCDA) [16] and polariton lasing in J-aggeragate/GaAs [17] OI systems indicates this is a promising route for future exploration. Alternating layers of thin ($3 - 5$ nm) organic and inorganic semiconductors (i.e. OI superlattices) with varied combinations of resonant and non-resonant organic and inorganic exciton energies with the HCTE energies can be explored for this purpose. Inorganic superlattices have found application in THz sources and in quantum cascade lasers. The potential of OI superlattices could be similarly vast.

There are three routes to fabricating OI superlattices. The first is by lifting off a epitaxial layer of III-V semiconductor thin film by chemical etching [18] and then alternating stacking the inorganic thin film and deposition of organic thin films. The second is alternating between stacking exfoliated or lifted-off 2D TMD semiconductor layers [19] and depositing organic thin films. The final route is alternating between atomic layer deposition (ALD) of a II-VI semiconductor such as ZnO with organic thin film deposition. The organic thin films can be deposited either by organic molecular beam deposition (OMBD) [20], or by vacuum thermal evaporation (VTE) of materials that form monolayers due their intrinsic properties, such as N,N'-dioctyl-3,4,9,10-perylenedicarboximide (PTCDI) [21]. The ALD method is advantageous since ALD is a low temperature process and can be done directly on the organic semiconductor film [22]. Further, each ALD process step allows for self-terminating monolayer growth, which permits fine control over the inorganic film layer thickness. Both the ALD film and the lifted off III-V film are expected to have high surface recombination velocities, which is not be a concern if the coupling between the semiconductors occurs through FRET. However, if the coupling is occurs through Dexter transfer as is the case for the HCTE, then exfoliated 2D TMD might be the most promising path forward.

Bibliography

[1] R. Hunger, R. Fritsche, B. Jaeckel, W. Jaegermann, L. J. Webb, and N. S. Lewis, "Chemical and electronic characterization of methyl-terminated Si(111) surfaces by high-resolution synchrotron photoelectron spectroscopy," *Phys. Rev. B* **72**, 045317 (2005).

[2] H. J. Joyce, Q. Gao, H. Hoe Tan, C. Jagadish, et al., "III-V semiconductor nanowires for optoelectronic device applications," *Prog. Quant. Electron.* **35**, 23 (2011).

[3] P. Rivera, J. R. Schaibley, A. M. Jones, J. S. Ross, et al., "Observation of long-lived interlayer excitons in monolayer MoSe2-WSe2 heterostructures," *Nat. Commun.* **6**, 6242 (2015).

[4] N. Bansal, L. X. Reynolds, A. MacLachlan, T. Lutz, et al., "Influence of crystallinity and energetics on charge separation in polymer-inorganic nanocomposite films for solar cells," *Sci. Rep.* **3**, 1531 (2013).

[5] U. B. Cappel, S. A. Dowland, L. X. Reynolds, S. Dimitrov, and S. A. Haque, "Charge generation dynamics in CdS:P3HT blends for hybrid solar cells," *J. Phys. Chem. Lett.* **4**, 4253 (2013).

[6] G. Grancini, M. Maiuri, D. Fazzi, A. Petrozza, et al., "Hot exciton dissociation in polymer solar cells," *Nat. Mater.* **12**, 29 (2012).

[7] K. Vandewal, S. Albrecht, E. T. Hoke, K. R. Graham, et al., "Efficient charge generation by relaxed charge-transfer states at organic interfaces," *Nat. Mater.* **13**, 63 (2014).

[8] A. Rao, A. K.-Y. Jen, C.-Z. Li, C. W. Schlenker, et al., "The role of spin in the kinetic control of recombination in organic photovoltaics," *Nature* **500**, 435 (2013).

[9] A. Rao, B. J. Walker, B. Ehrler, K. P. Musselman, et al., "Resonant energy transfer of triplet excitons from pentacene to PbSe nanocrystals," *Nat. Mater.* **13**, 1033 (2014).

[10] N. J. Thompson, M. W. B. Wilson, D. N. Congreve, P. R. Brown, et al., "Energy harvesting of non-emissive triplet excitons in tetracene by emissive PbS nanocrystals," *Nat. Mater.* **13**, 1039 (2014).

[11] J. Lee, C. Jeong, C. Coburn, T. Batagoda, M. E. Thompson, and S. R. Forrest, "Hot excited state management for long-lived blue phosphorescent organic light-emitting diodes," *Nat. Commun.* **8**, 15566 (2017).

[12] Y. Zhang and S. R. Forrest, "Existence of continuous-wave threshold for organic semiconductor lasers," *Phys. Rev. B* **84**, 241301 (2011).

[13] L. V. Butov, "Excitonic devices," *Superlattices Microstruct.* Indirect Excitons: Physics and Applications **108**, 2 (2017).

[14] A. Violante, K. Cohen, S. Lazic, R. Hey, R. Rapaport, and P. V. Santos, "Dynamics of indirect exciton transport by moving acoustic fields," *New J. Phys.* **16**, 033035 (2014).

[15] V. M. Agranovich, Y. N. Gartstein, and M. Litinskaya, "Hybrid resonant organic-inorganic nanostructures for optoelectronic applications," *Chem. Rev.* **111**, 5179 (2011).

[16] M. Slootsky, X. Liu, V. M. Menon, and S. R. Forrest, "Room temperature Frenkel-Wannier-Mott hybridization of degenerate excitons in a strongly coupled microcavity," *Phys. Rev. Lett.* **112**, 076401 (2014).

[17] D. Coles, D. G. Lidzey, G. G. Paschos, J. L. Bricks, et al., "Hybrid organic-inorganic polariton laser," *Sci. Rep.* **7**, 1 (2017).

[18] K. Lee, J. D. Zimmerman, T. W. Hughes, and S. R. Forrest, "Non-destructive wafer recycling for low-cost thin-film flexible optoelectronics," *Adv. Funct. Mater.* **24**, 4284 (2014).

[19] E. V. Calman, C. J. Dorow, M. M. Fogler, L. V. Butov, et al., "Control of excitons in multi-layer van der Waals heterostructures," *Appl. Phys. Lett.* **108**, 101901 (2016).

[20] S. R. Forrest, "Ultrathin organic films grown by organic molecular beam deposition and related techniques," *Chem. Rev.* **97**, 1793 (1997).

[21] A. Zykov, S. Bommel, C. Wolf, L. Pithan, et al., "Diffusion and nucleation in multilayer growth of PTCDI-C8 studied with in situ x-ray growth oscillations and real-time small angle x-ray scattering," *J. Chem. Phys.* **146**, 052803 (2016).

[22] G. N. Parsons, S. E. Atanasov, E. C. Dandley, C. K. Devine, et al., "Mechanisms and reactions during atomic layer deposition on polymers," *Coord. Chem. Rev.* Chemical Vapor Deposition and Atomic Layer Deposition: Precursor Design and Application **257**, 3323 (2013).